1989

The diffusion of muonic deuterium atoms in deuterium gas

James Brian Kraiman
College of William & Mary - Arts & Sciences

INFORMATION TO USERS

The most advanced technology has been used to photograph and reproduce this manuscript from the microfilm master. UMI films the text directly from the original or copy submitted. Thus, some thesis and dissertation copies are in typewriter face, while others may be from any type of computer printer.

The quality of this reproduction is dependent upon the quality of the copy submitted. Broken or indistinct print, colored or poor quality illustrations and photographs, print bleedthrough, substandard margins, and improper alignment can adversely affect reproduction.

In the unlikely event that the author did not send UMI a complete manuscript and there are missing pages, these will be noted. Also, if unauthorized copyright material had to be removed, a note will indicate the deletion.

Oversize materials (e.g., maps, drawings, charts) are reproduced by sectioning the original, beginning at the upper left-hand corner and continuing from left to right in equal sections with small overlaps. Each original is also photographed in one exposure and is included in reduced form at the back of the book. These are also available as one exposure on a standard 35mm slide or as a 17" x 23" black and white photographic print for an additional charge.

Photographs included in the original manuscript have been reproduced xerographically in this copy. Higher quality 6" x 9" black and white photographic prints are available for any photographs or illustrations appearing in this copy for an additional charge. Contact UMI directly to order.

U·M·I

University Microfilms International
A Bell & Howell Information Company
300 North Zeeb Road, Ann Arbor, MI 48106-1346 USA
313/761-4700 800/521-0600

Order Number 8923059

The diffusion of muonic deuterium atoms in deuterium gas

Kraiman, James Brian, Ph.D.

The College of William and Mary, 1989

U·M·I

300 N. Zeeb Rd.
Ann Arbor, MI 48106

THE DIFFUSION OF MUONIC DEUTERIUM ATOMS IN DEUTERIUM GAS

A Dissertation

Presented to

The Faculty of the Department of Physics

The College of William and Mary in Virginia

In Partial Fulfillment

Of the Requirements for the Degree of

Doctor of Philosophy

---

by

James Brian Kraiman

1989

APPROVAL SHEET

This dissertation is submitted in partial fulfillment of the requirements for the degree of

Doctor of Philosophy

James Brian Kraiman

Approved, January 1989

Robert T. Siegel

Robert E. Welsh

Allen H. Boozer

Keith W. Miller
Department of Computer Science

James J. Reidy
Department of Physics and Astronomy
University of Mississippi

DEDICATION

To my parents Robert and Claire

AND

To my sisters Marla and Ella

AND

To my wife Bernadette

TABLE OF CONTENTS

ACKNOWLEDGEMENTS

I would like to thank the many people who have made this work possible:

Dr. Robert Siegel, my advisor, for the countless hours put into the design, construction, and analysis phases of this experiment. I would especially like to thank him for teaching me a great deal of physics in the past three and a half years.

Dr. Robert Welsh, for his help during the experimental runs, helpful comments regarding the experiment, and for reading the manuscript.

Mr. William Vulcan, for all of his help during my years at William and Mary, and for his tireless efforts during the experimental runs.

Dr. James Reidy, for his many contributions to the experiment, his reading of the manuscript, and for being a pleasure to work with.

Dr. Peter Kammel, for his many valuable contributions to this experiment, especially during experimental runs.

Dr. Hannes Zmeskal, for the design, construction, and operation of the gas/vacuum system.

Dr. Joachim Hartmann, for his important contributions to this experiment, particularly his efforts to keep the experiment running smoothly.

Dr. Claude Petitjean, for his valuable comments regarding this experiment and his efforts during experimental runs.

Dr. Alex Zehnder, for his important comments and insights concerning this experiment.

Drs. Paul Guss, Dayle Hancock, and Heather Wolverton for their valuable help during the experimental runs.

Dr. Johannes Marton, for his efforts during experimental runs.

Dr. Michael Cargnelli, for his help during experimental runs.

Dr. Ed Remler, for conveying his insights into the diffusion process.

Mr. GuoFu Chen, for his help during experimental runs and for his contributions to the analysis.

Mr. Peter Baumann, for his hard work during experimental runs.

Dr. Keith Miller, for helpful discussions concerning random numbers and data analysis, and for reading the manuscript.

Dr. Steve Park for several valuable discussions concerning random numbers and data analysis, and for supplying the generator for producing streams of random numbers.

Dr. Roger Carlini, for important suggestions concerning the data analysis.

Dr. Allen Boozer, for reading the manuscript.

Mr. Ulrich, for his excellent design of the target vessel.

Mr. Oschwald and the entire staff of the machine shop at the Paul Scherrer Institute, for their superb craftsmanship in constructing the target vessel and other assorted items used in the experiment.

Mr. Zimmermann, for his excellent workmanship in constructing the scintillation counters used in the experiment.

Drs. Morton Eckhause and John Kane, for their kindness and consideration shown me during my years at William and Mary.

Drs. Donald Joyce and Robert Whyley, for the generous amount of help and advice they provided me over the years.

Fellow graduate students Michael Chapman, John Ginkel, and Chris Kenney, for being fellow graduate students.

Mr. Richard Siegel, for developing the software which was used to produce some of the figures in this work.

Ms. Dianne Fannin, Ms. Paula Spratley, and Ms. Sylvia Stout for the bountiful help they have provided me over the years, and for being so patient when answering my questions.

I would like to take this opportunity to thank the many people at the Paul Scherrer Institute for their gracious hospitality. In particular, I would like to thank:

Dr. David Taqqu, for several stimulating discussions and for being kind enough to share his office with me.

Ms. Monika Keller and Family, for their tremendous hospitality and kindness shown to me during my stay in June 1988.

Very special thanks to Ms. Anne Bolsinger, for being such a wonderful person and valued friend.

Most importantly, I owe an infinite amount of gratitude to my lovely and beautiful wife Bernadette, whose love and devotion have helped me through it all.

This work was supported in part by the National Science Foundation.

LIST OF TABLES

ABSTRACT

Negative muons were brought to rest in a target array consisting of 30-50 parallel plastic foils coated with Au which were separated by a few mm. The interstitial volumes between the foils were filled with deuterium gas at pressures from 0.094 bar to 1.52 bar. Muons which stopped in the deuterium formed μd atoms, which subsequently diffused through the gas until either the muon decayed or the μd atom struck a foil surface. For μd atoms impinging upon the Au layer, the muon would transfer to an Au atom, resulting in the formation of a μAu atom in a highly excited state. De-excitation to the 1S ground state resulted in emission of characteristic muonic Au x rays, and after the muon was absorbed by the Au nucleus, the emission of Pt γ rays. These transfer photons were detected by one of four germanium x-ray detectors adjacent to the target vessel. Analysis of the time distributions formed by collecting delayed transfer events for several sets of experimental conditions yielded information on the diffusion process of μd atoms in deuterium gas.

The initial speed distribution of the μd atoms upon reaching the 1S state is described reasonably well by a Maxwellian speed distribution of mean energy $3KT/2 = 1.8 \pm 0.1$ eV. The theoretical scattering cross sections for the reaction

$$\mu d + d \rightarrow \mu d + d$$

calculated by Bubak and Faifman agree well with this experiment when the effects of molecular scattering are approximated by multiplying the nuclear cross sections by a factor of about two. It was found that a factor of 2.10 for center of mass collision energies greater than 0.30 eV, and 2.30 for collision energies less than 0.30 eV provided a good fit to the experimental data.

THE DIFFUSION OF MUONIC DEUTERIUM ATOMS IN DEUTERIUM GAS

Chapter I

INTRODUCTION

I.1 Purpose of the Experiment

The discovery of parity violation in weak interactions [1,2] led to a generalization of Fermi's theory [3,4] into what is known as the V-A theory of weak interactions. One of the "classical", i.e. strangeness-conserving weak interactions, is the semi-leptonic process of muon absorption by a proton

$$(I\text{-}1) \qquad \mu^- + p \rightarrow n + \nu_\mu$$

The absorption of the muon occurs from the 1S hydrogenic atomic state [5], which has the wave function:

$$(I\text{-}2) \qquad \phi_\mu(r) = \left[\frac{Z^3}{\pi a_\mu^3}\right]^{1/2} e^{-Zr/a_\mu}$$

for an atom with Z protons and where a_μ is the first muonic Bohr radius. It should be noted that for heavy nuclei Z must be replaced by the effective charge felt by a muon as it penetrates the nucleus [6]. The absorption rate is proportional to Z^4 since it is related to the probability of finding the muon in the nucleus ($|\phi_\mu(0)|^2$) as well as the number of protons in the nucleus. The rapid increase of the capture rate with Z would suggest that a muon absorption experiment in a high Z material

would be the simplest to perform. However, the interpretation of experimental results in complex nuclei is complicated because the calculation of the muon absorption rate involves matrix elements which are taken with respect to the initial and all possible final nuclear states. Thus, the matrix element involves a sum over the nucleons in the nucleus [6]. To avoid this complication the obvious choice is to carry out a muon absorption experiment using hydrogen, in which the muon absorption rate is only about 10^{-3} that of the muon decay rate [7].

According to V-A theory the matrix element which describes reaction (I-1) involves contributions from four terms - the vector, axial vector, weak magnetism, and induced pseudoscalar terms (see §I.2). The last two are directly proportional to the momentum transfer q, where q is the difference in the four-momenta of the proton and the neutron. The kinematics for muon absorption on a proton at rest yield a value for the momentum transfer of $q^2 \approx -0.9m_\mu^2$ (which is large compared to β-decay), and therefore the weak magnetism and induced pseudoscalar terms are expected to make large contributions to the reaction rate of process (I-1).

The transition rate for process (I-1) depends strongly upon the relative spin orientations of the proton and the muon at the time of absorption. For the case when the spins are anti-parallel (designated as the singlet hyperfine state F=0) the reaction rate is roughly 50 times the rate for the case when the spins are

parallel (F=1) [7]. In addition, the transition rate for the triplet (F=1) case is particularly sensitive to the value of the (effective) induced pseudoscalar coupling constant (IPCC) [8] (see §I.2). Therefore, in order to determine experimentally the value of the IPCC with good precision, it is of interest to observe muon absorption in hydrogen from the triplet state. Experimentally, the absorption rate from the statistical mixture of hyperfine states would be observed.

Initially μp atoms (see Chapter II) are formed in a statistical mixture of hyperfine spin states ($\propto$ 2F+1), i.e. 75 % are in the triplet state and 25 % are in the singlet state. The ratio of triplet to singlet μp atoms does not remain constant in time but actually decreases due to the following process. The μp atom experiences collisions with surrounding H_2 molecules, with the number of collisions dependent upon the mean free path of the μp atoms in the gas. On average the μp atom will lose kinetic energy (K.E.) until the K.E. (in the center of mass system) falls below the hyperfine splitting of 0.183 eV. It is then unlikely, assuming the H2 gas is at room temperature (3KT/2 = .038 eV), for the μp atom to return to the F=1 state. The time at which this essentially irreversible process occurs will depend upon the initial velocity distribution of the μp atoms as well as the energy-dependent scattering cross sections for the reaction

(I-3) $\quad \mu p + H_2 \rightarrow \mu p + H_2$

After this time all the muon absorption will take place from the singlet hyperfine state.

Experiments which measure the muon absorption rate in liquid hydrogen (where the absorption predominately occurs while the muon is bound in a $p\mu p$ molecule) [9,10] and in gaseous hydrogen [11] have already been performed. However, the experiments in liquid hydrogen yielded no information on the absorption rate from the triplet hyperfine state while the experiment in gaseous H_2 was performed at a pressure (8 atm) at which the observed absorption events would have all occurred from the singlet hyperfine state [11]. Therefore, one is led to perform a muon absorption experiment to measure the absorption rate from the triplet hyperfine state in gaseous hydrogen.

In order to acquire information on the value of the IPCC it is necessary to determine under what experimental conditions (gas pressure and geometry) the statistical mixture of hyperfine states will be preserved long enough to allow muon absorption from the triplet state to be observed. Thus, prior to studying muon absorption in low pressure hydrogen gas, a preliminary experiment must be conducted - hereafter referred to as the diffusion experiment. The purpose of this diffusion experiment is twofold - 1) to determine the initial velocity distribution of the muonic hydrogen atoms (by initial it is meant that the atoms have reached the 1S ground state), and 2) to be able to test current theoretical predictions regarding the scattering cross sections which govern the diffusion process. It should be mentioned that the initial velocity distribution is of interest by itself since it would allow a comparison with

experiment of current theories regarding muonic atom formation.

As discussed in Chapter III, this experiment was performed with deuterium gas, yet a major motivation for conducting the experiment was to be able to gather enough information on the diffusion process to design a muon absorption experiment in hydrogen gas. The reason becomes clear when one looks at the theoretical scattering cross sections for a $\mu d(\mu p)$ atom in deuterium(hydrogen) gas [12]. The scattering probability for a μp atom in hydrogen gas is significantly larger than that for a μd atom in deuterium gas. Scattering will distort the initial velocity distribution (see Chapter III) and hence make it more difficult to extract. Thus, it was logical to perform the initial diffusion experiment in deuterium gas first. At this writing a second experiment using hydrogen gas has also been performed and is being analyzed. Indeed, the comparison of the initial velocity distributions in hydrogen and deuterium may shed some light on the muonic atom formation process.

An additional motivation for using deuterium involves muon catalyzed fusion (μcf). In μcf, a muon is brought to rest in a mixture of hydrogen isotopes (H_2,D_2,T_2) forming μp, μd or μt atoms. These atoms will then experience collisions with the molecules in this mixture, with some collisions resulting in the formation of $d\mu d$,$d\mu t$,$t\mu t$ or $p\mu p$ molecular ions. A fusion reaction may then occur which would cause the emission of a He nucleus and the muon as well as neutrons and γ rays [13], e.g.

(I-4) $\quad d\mu t \rightarrow \alpha + n + \mu^- + 17.6$ MeV

After the fusion reaction the muon is free to catalyze another fusion reaction unless it is captured by the final alpha particle, in which case it remains bound to the ^{4}He nucleus until the muon decays. For a more complete discussion of this process the reader is referred to [13] and references therein. Information obtained on the scattering cross sections associated with μd atoms in deuterium is therefore of interest in the study of the μcf process.

I.2 Muon Absorption

All charged weak processes can be described by an effective Lagrangian density

$$(I\text{-}5) \qquad L = \frac{-G_F}{2\sqrt{2}} \left[J_\lambda J^{\lambda\dagger} + J^{\lambda\dagger} J_\lambda \right]$$

where $G_F \approx 1.435 \times 10^{-49}$ erg-cm^3 is the universal Fermi coupling constant [5]. The current J_λ can be expressed as the sum of a strangeness-conserving hadronic current J^1_λ, a strangeness-changing hadronic current J^2_λ, and a leptonic current j_λ

$$(I\text{-}6) \qquad J_\lambda = J^1_\lambda \cos\theta + J^2_\lambda \sin\theta + j_\lambda$$

The angle θ appearing in (I-6) is the Cabibbo angle, an empirical parameter which has been added to the theory in order to give agreement between theory and experiment. The Cabibbo angle was originally introduced to explain the different rates for weak decays depending on whether strangeness was or was not conserved. It also accounts for the slight deviation from unity of the ratio of vector couplings in β-decay and μ-decay [14]. The leptonic current is itself a composite of an electronic current and a muonic current

$$(I\text{-}7) \qquad j_\lambda = j^e_\lambda + j^\mu_\lambda$$

Muon absorption by a proton is a strangeness-conserving semi-leptonic process which only involves the currents J^1_λ and j^μ_λ. The hadronic current can be further decomposed into a vector current and an axial vector current

$$(I\text{-}8) \qquad J_\lambda^1 = J_\lambda^V + J_\lambda^A$$

The most general form of these currents which is consistent with Lorentz covariance involves the "bilinear" quantities given in Table I, where γ^λ are the 4x4 Dirac matrices with

$$(I\text{-}9) \qquad \gamma^0 = \begin{bmatrix} I & 0 \\ 0 & -I \end{bmatrix} \qquad \gamma = \begin{bmatrix} 0 & \sigma \\ -\sigma & 0 \end{bmatrix} \qquad \gamma^5 \equiv i\gamma^0\gamma^1\gamma^2\gamma^3 = \begin{bmatrix} 0 & I \\ I & 0 \end{bmatrix}$$

Here σ are the Pauli matrices and Ψ are the plane wave solutions to the Dirac equation. The names S,V,T,A,P arise from the behavior of the quantities in Table I under Lorentz transformations (rotations) and space inversion (parity).

Table I
Bilinear Covariants

S	Scalar	$\bar{\Psi}\Psi$
V	Vector	$\bar{\Psi}\gamma^\lambda\Psi$
T	Tensor	$\bar{\Psi}\sigma^{\lambda\nu}\Psi$
A	Axial Vector	$\bar{\Psi}\gamma^5\gamma^\lambda\Psi$
P	Pseudoscalar	$\bar{\Psi}\gamma^5\Psi$

Use of the quantities in Table I and the four-momentum transfer $q \equiv p_n - p_p$ allows the construction of the general form of the V and A hadronic currents [5]

$$(I\text{-}10a) \qquad J_\lambda^V = f_V\gamma_\lambda + if_W\sigma_{\lambda\nu}q^\nu + f_S q_\lambda$$

$$(I\text{-}10b) \qquad J_\lambda^A = f_A\gamma_\lambda\gamma^5 + f_P q_\lambda\gamma^5 + if_T\sigma_{\lambda\nu}q^\nu\gamma^5$$

where the form factors $f = f(q^2)$, and the f_W term is known as the

weak magnetism term since it is analogous to the anomalous magnetic moment term originating from the coupling between nucleons and the electromagnetic field [6]. The f_A and f_V terms are considered to be the primary currents, the other terms are induced from these primary currents by the strong (hadronic) interaction. The muonic current is given in V-A form as

$$(I\text{-}11) \qquad j_\lambda^\mu = \bar{\Psi}_\nu \gamma_\lambda (1 - \gamma_5) \Psi_\mu$$

The expressions in equations (I-10) can be simplified by observing how the bilinear quantities of Table I transform under the G-parity operation

$$(I\text{-}12) \qquad G = Ce^{i\pi I_2}$$

which involves the charge conjugation operator C and an isospin rotation of π about the I_2 axis. Since all six terms in (I-10) transform in the same way under this rotation, only the behavior under C need be investigated [5]. In equation (I-10a) the V and W terms transform in the same way under C (i.e. are positive in sign) while the S term transforms oppositely. Similarly, in equation (I-10b) the T term behaves differently from the A and P terms under charge conjugation. This leads to the designation of the V,A,P, and W terms as "first class" currents and the S and T terms as "second class" currents. The hadronic interaction is invariant under G (only one G class of interactions can exist), i.e. nuclear forces conserve isospin and charge symmetry holds. Since the P,W,S, and T terms are induced by the strong interaction and the existence of the V and A terms are well

established, it might be expected that the second class terms S and T do not contribute in weak interactions. Indeed, $f_S = 0$ is predicted by the conserved vector current hypothesis (CVC) [3] which was developed to explain why the coupling constants in β-decay (e.g. n -> p + e^- + ν_e , which involves hadronic interactions) and muon decay (a purely leptonic process) are the same within a few percent.

The currents in (I-10) and (I-11) can be used to calculate the transition rate of process (I-1), where it will be seen that there is a pronounced hyperfine effect on the rate of muon absorption by a proton in a μp atom. The transition rate for muon absorption can be calculated using Fermi's Golden Rule. The matrix element involved in this calculation, if second class currents are ignored, is given by [5]

$$(I\text{-}13) \qquad M = \frac{G_F \cos\theta}{\sqrt{2}} \int d^3x \; \bar{\psi}_n \hat{O} \; \psi_p$$

and from equations (I-10) and (I-11)

$$(I\text{-}14) \qquad \hat{O} = f_V \gamma^\lambda j_\lambda + i f_W \sigma^{\lambda\nu} q_\nu j_\lambda - f_A \gamma^\lambda \gamma_5 j_\lambda - f_p q^\lambda \gamma_5 j_\lambda$$

Equation (I-13) can be simplified to yield an expression for the matrix element which involves the effective form factors F_V, F_A, and F_P [5] (see Appendix A) :

$$(I\text{-}15a) \qquad F_V = G_F \cos\theta \; f_V \left[1 + \frac{E_\nu}{2m_N} \right]$$

$$(I\text{-}15b) \qquad F_A = G_F \cos\theta \left[-f_A - \frac{E_\nu}{2m_N} \left(f_V + 2m_N f_W \right) \right]$$

$$(I\text{-}15c) \qquad F_P = G_F \cos\theta \, \frac{E_\nu}{2m_N} \left[f_A - m_\mu f_P - (f_V + 2m_N f_W) \right]$$

where m_N is the nucleon mass, E_ν is the energy of the neutrino emitted in muon absorption ($\approx$ 100 MeV), and the form factors are functions of q^2. The ratio of the muon absorption rate in the singlet hyperfine state of the μp atom to the rate in the triplet state can then be determined and is given by [8]

$$(I\text{-}16) \qquad \frac{\Gamma(F=0)}{\Gamma(F=1)} = \frac{(F_V - 3F_A)^2 - 2F_P(F_V - 3F_A) + F_P^2}{(F_V + F_A)^2 - \frac{2}{3} F_P(F_V + F_A) + F_P^2}$$

The values of the form factors in equations (I-15), which must be evaluated at the momentum transfer involved in muon absorption by a proton ($q^2 = -0.9m_\mu^2$), are taken to be [5]:

$$(I\text{-}17a) \qquad f_V(q^2) = 0.97 f_V(0) = 0.97$$

$$(I\text{-}17b) \qquad f_W(q^2) = 0.97 f_W(0) = \frac{0.97(\mu_p - \mu_n - 1)}{2m_N} = \frac{0.97(3.70)}{2m_N}$$

$$(I\text{-}17c) \qquad f_A(q^2) = f_A(0) = 1.25$$

$$(I\text{-}17d) \qquad m_\mu f_P(q^2) \approx \frac{2m_\mu m_N f_A(0)}{q^2 + m_\pi^2} \approx 7 f_A(0)$$

where m_π is the charged pion mass, and μ_p and μ_n are the proton and neutron magnetic moments, respectively. The estimate of f_P in (I-17d) is known as the Goldberger-Treiman (GT) relation [15]. A more accurate determination of the absorption rates (I-16) will constrain the experimental value of the IPCC and therefore serve as a test of the GT relation.

Substitution of the values in (I-17) into equations (I-15) and then evaluating (I-16) demonstrates that there is a pronounced hyperfine effect on the muon absorption rate, with the rate in the singlet state roughly fifty times that in the triplet state. Also, the fact that $F_V \approx -F_A$ indicates that the muon absorption rate in the triplet hyperfine state should be more sensitive to the value of F_P, and therefore to f_P, than the absorption rate in the singlet hyperfine state. From this arises the interest in performing an experiment to measure the muon absorption rate in the triplet hyperfine state of the μp atom. Such an experiment must be carried out under experimental conditions which preserve the initial statistical mixture of hyperfine states long enough for the muon absorption rate in this mixture (R_{St}) to be observed. The absorption rate in the triplet state (R_T) then follows from

$$(I\text{-}18) \qquad R_{St} = \frac{3}{4} R_T + \frac{1}{4} R_S$$

since the absorption rate from the singlet state (R_S) has already been measured with $\approx$ 10 % accuracy [11]. The experimental condition necessary to accomplish the preservation of the initial statistical mixture of the hyperfine states can only be determined if the diffusion process of the μp atom in hydrogen gas is well understood. Therein lies the motivation for studying the diffusion process of muonic hydrogen atoms in hydrogen gas.

Chapter II

THEORY

II.1 Slowing Down of Muons in Hydrogen

In this experiment negative muons are brought to rest inside a target of multiple planar foils which are separated by a small ($\approx$ 2-4 mm) gap of deuterium gas (see Chapter III). Muons which stop in the gas will undergo atomic capture and form μd atoms. In the analysis of the experimental data the μd formation time is taken to be equal to the time at which muons stop in the plastic foils. To justify this assumption it is necessary to compare the times in which a muon is captured in a foil and in a gas gap. Thus, it is necessary to know the moderation time from some initial energy ($\approx$ 5 MeV in our case) down to an energy at which atomic muon capture can occur.

The slowing of the muon in hydrogen can be divided into three stages. The first stage involves the velocity region where the muon velocity (v_μ) is much greater than the velocity of an electron in a hydrogen atom ($v_e = \alpha c$, where α is the fine structure constant). The intermediate velocity region, in which the muon slows to a velocity near v_e, comprises the second stage and the velocity region $v_\mu < v_e$ constitutes the final stage of the moderation process.

In the high velocity region ($v_\mu \gg v_e$) the energy loss, in the non-relativistic approximation, is given by [16]

$$(II\text{-}1) \qquad \frac{dE}{dx} = \frac{4\pi e^4 NZ}{m_e c^2 \beta^2} \ln \frac{2m_e c^2 \beta^2}{I}$$

where E is the kinetic energy of the muon, N is the number density of the stopping medium with Z protons, m_e is the electron mass, I (= 20.4 eV in H_2 [2]) is the adjusted ionization potential (also known as the adjusted mean excitation energy), and $\beta \equiv v_\mu/c$. The non-relativistic form of the Bethe-Bloch equation can be used since $\approx$ 35 MeV/c muons ($\beta \approx 0.3$) were used in this experiment, i.e. the relativistic corrections are small. The lower limit of validity of equation (II-1) is near a muon kinetic energy of 50 keV in light ($Z<5$) elements, although this limit can be pushed somewhat lower in hydrogen [17]. For $E < 50$ keV alternative formulations, in which the energy loss is proportional to $\sqrt{E}$ (and not E^{-1} as in the Bethe-Bloch region), must be employed [17,18]. When $E < 2.8$ keV ($v_\mu < \alpha c$) nuclear stopping, elastic scattering from the screened Coulomb potential of the nucleus, becomes important [18] and energy loss by adiabatic ionization must also be considered [19].

At the present time we are only interested in moderation times needed before atomic capture of the muon can occur. The time required for a 10 MeV muon ($\beta \approx 0.4$) to be moderated to an energy of 0.13 MeV ($\beta \approx 0.05$) has been calculated to be roughly 700 ns in hydrogen gas at STP and about 1 ns in liquid hydrogen [19].

In this experiment nearly all of the stopping power in the target is due to the foils (§III.3) and therefore the time required to moderate a muon to an energy of ≈ 0.1 MeV is of the order of 1 ns. The moderation time from 150 keV to 2 keV is independent of the hydrogen isotope which serves as the moderator, while for energies less than 2 keV the difference in moderation times in H_2 and D_2 is quite small [19]. Therefore, it is acceptable to use the available results for the moderation of muons in H_2.

The experimental condition for which the muons would require the longest moderation times (t_m) in the gas involved 94 mbar D_2 and a 2.3 mm gap. An estimate of the maximum energy at which a muon may enter this gap and come to rest in the gas is provided by range-energy tables [17]. It is evident from the tables that this maximum energy is < 10 keV for this experimental condition. (There is, of course, a distribution of muon kinetic energies entering the gas gap.) In the energy range $2 \leq E \leq 10$ keV the muon energy loss in H_2 is at its maximum value and is nearly constant (to a first approximation) over this energy interval [17,20]. An upper limit to the moderation time (t_1) in this energy interval can be found by considering the (roughly constant) energy loss (dE/dx) of the muon to be the minimum energy loss in this region (dE/dx ≈ 300 keV/cm at STP H_2). The moderation time t_1 is then given by

$$(II\text{-}2) \qquad t_1 < \sqrt{2m_\mu}\,(dx/dE)\,(\sqrt{E_i} - \sqrt{E_f})$$

where m_μ is the muon mass, and $E_i(E_f)$ is 10(2) keV. Then, a

conservative estimate is $t_1 < 1$ ns. The moderation time for a 2 keV muon to be captured in very low pressure hydrogen gas ($p \leq 1$ torr, 300K) has been measured [21]. At 1.0 torr a value of $t_m = 170 \pm 40$ ns was observed and t_m was found to be inversely dependent upon the density of the gas. Scaling this result to a pressure of 94 mbar ($\approx$ 70 torr) indicates that a 2 keV muon requires about 2.5 ns to be captured in deuterium in our lowest pressure experimental arrangement. We can then conclude that the time difference between muon capture in the foils and capture in the gas is roughly 3 ns at the lowest pressure used, with this difference decreasing linearly with increasing pressure. Therefore, within the time resolution (FWHM) of the experimental system ($\approx$ 12-15 ns) the assumption that the stopping time of the muons in the foils is equivalent to the formation time of the μd atoms in the gas seems justified.

A short description of the method used to compute the quoted theoretical moderation times follows. In atomic hydrogen, when $v_\mu < \alpha c$ (i.e. low energy stopping powers are needed), this method [19] employed an adiabatic approach in which the electrons moved in stationary states around the fixed muon and proton. (In the adiabatic approach the period of transition for an electron to pass from a bound state into the continuum is short compared to the collision time of a muon with a hydrogen atom.) For small muon-proton separation R the electron is considered to be moving in an electric dipole potential of dipole moment eR. When $R \approx 0.64a_0$, where a_0 is the Bohr radius, the

binding energy of the electron becomes zero [19,22]. Thus, the slow moving muon is still able to ionize the hydrogen atom, and can continue to lose energy in this process until the muon's kinetic energy falls below 13.6 eV. Once this energy is reached, the muon will be captured when it passes another proton at a distance $< 0.64a_0$.

The adiabatic approximation is not as accurate for molecular hydrogen where the critical muon-proton separation is not so well determined. In addition, the collision with a molecule is not adiabatic since the collision time is shorter than the transition time for the electron to pass from a bound atomic state into the continuum [19]. Instead of the adiabatic approximation, the following model was used to calculate the ionization cross section for a slow ($v_\mu < \alpha c$) muon colliding with a hydrogen molecule. The electron was considered to be bound in a potential well of depth 13.6 eV and range a_0. The depth of the well is reduced to 1 % of its original value at t=0 and then returned to its original depth after a time taken to be the collision time of a muon with a H_2 molecule. Ionization was found to occur in 90 % of the cases, and the most probable value of the cross section for ionizing an H_2 molecule was estimated to be $\approx 0.1\pi a_0^2$ in the velocity interval $5 \times 10^{-4}c < v < \alpha c$. The energy loss due to this mechanism was then adjusted to fit smoothly to the energy loss which was calculated for higher muon velocities using the Born approximation, and for $v_\mu \gg v_e$ equation (II-1) was used [19]. This energy loss function was then used to compute the

moderation times quoted earlier from Wightman [19].

II.2 Atomic Capture

The atomic capture process, and the related process of muons slowing down in matter, has been studied for the past forty years. Of particular interest here are the theoretical predictions for the initial energies at which atomic capture of the muon occurs in hydrogen gas since these energies have a profound effect on the subsequent diffusion process. These predictions have varied greatly from capture energies which are near thermal [23] to energies of several keV [24]. A brief survey of some of these theories is given below.

A simplified view of the atomic capture process in hydrogen can be obtained from the Bohr model. The muon and electron energies vary as

$$E_\mu \sim \frac{m_\mu}{n_\mu^2} \quad , \quad E_e \sim \frac{m_e}{n_e^2}$$

where $m_e(m_\mu)$ is the electron(muon) mass and $n_e(n_\mu)$ is the electron(muon) principal quantum number. In this simple picture capture is expected to occur when the energy of the muon is equal to the energy of a K-shell electron ($n_e = 1$, $E_e = 13.6$ eV), which in turn implies that capture occurs in the orbit $n_\mu \approx (m_\mu/m_e)^{\frac{1}{2}} \approx 14$.

The classical approach to studying the mechanism for slowing down and capture of a muon is known as the Fermi-Teller (F-T) method [22,25-27]. In this model the electrons in the stopping medium are treated as belonging to a degenerate Fermi gas. The muon, which is assumed to be moving at a velocity less than the

velocity of the valence electrons in the stopping medium, loses energy as it scatters from electrons in this gas. The energy loss of the muon is treated as a continuous process and is taken to be an average over all possible collisions [22]. However, the use of average energy losses instead of actual energy losses experienced by the muon as it slows down prevents the development of the distribution of muon energies upon capture [27] (i.e. there is some distribution of possible energy losses for each collision). The Fermi-Teller model has been modified to account for these actual energy losses and yields the result that atomic capture of the muon occurs at higher energies than the F-T model suggests [27]. The moderation and capture process of muons in matter has also been studied by using classical equations of motion in which the energy loss was modeled in terms of frictional forces [25]. However, all of the aforementioned classical models were developed for condensed media and are inapplicable to the problem of muon capture in light elements [28].

Many quantum mechanical calculations of the slowing down and capture of muons in light elements exist. Atomic capture of the muon proceeds via excitation of electrons (Auger transitions) or by direct Coulomb capture which results in the emission of a γ ray (radiative transitions), although the latter mechanism has been shown to be relatively unimportant in the capture process [23,29]. Early results using the Born approximation had atomic capture occurring at near thermal energies in orbits with muon principal quantum numbers < 14 [23]. However, this treatment

only studied the problem of capture and not the related process of the slowing down of the muon. Subsequent quantum mechanical studies have taken the moderation of the muon into account when computing atomic capture rates [28-30] (although one of these [30] studied the Z dependence of capture probability in solids).

The process of slowing down and atomic capture of the muon in hydrogen was investigated by Haff and Tombrello [29] under the simplifying assumptions that capture occurred on isolated atoms where molecular effects were excluded. The calculated capture rate exhibited a rapid increase with decreasing energy until the kinetic energy of the muon fell below the electron binding energy, at which point the capture rate increased more slowly since the number of final muon states available began to decrease [29]. An important result of this model was that half of the muons were captured by hydrogen atoms when their energies were above 75 eV, i.e. well above the ionization potential of hydrogen. However, the initial populations of angular momentum states l and muon principal quantum numbers n after capture were not determined.

A Born approximation calculation similar to that used in [29] was used by Korenman and Rogovaya [28] to calculate the distributions for n and l. It was found that the capture probability for muon states with a principal quantum number n was given by a wide distribution over n, with the maximum value occurring at $n_m \approx 11$ (to be compared with the result of most models that $n_m \approx 13$ or 14). By a wide distribution over n it is

meant that the capture probability for states with $n > n_m$ was greater than 50 %. The l (angular momentum) distribution was determined to be circular (i.e. $l = n-1$, see §II.5) for low n states. When $n \geq n_m$ the maximum population of l-states for a given n occurred at a value $l_m < n - 1$, with the population of states with $l > l_m$ sharply decreasing for increasing l. Also, it was found that the capture probability energy distribution had a maximum at a muon energy of $\approx$ 50 eV [28].

A diabatic (non-adiabatic) state method to describe the moderation and capture of muons has been used by Cohen et al. [31] to calculate the initial kinetic energy distribution of the muons upon capture. The prediction that most muons are captured at energies near or below the ionization potential in hydrogen, with a rapid decrease in the capture probability for energies larger than this, is in disagreement with earlier Born approximation calculations which claim that capture occurs at energies > 50 eV [28-30]. The difference may stem from the calculation of the energy loss of low energy muons in hydrogen [31]. The older theories use the stopping power calculations of Rosenberg [32], whereas the stopping power computed with the diabatic state model yields moderation times of slow muons ($v_\mu \leq \alpha c$) which are a factor of 5-10 shorter than the times predicted using Rosenberg's model [31,33]. The use of an accurate stopping power is a crucial part of calculating the energies at which capture occurs. If a muon loses energy rapidly in the hydrogen gas, then most captures would occur at low energies, but if the

energy loss is slow the muons will spend a longer time at higher energy and therefore will tend to be captured at higher energies [29]. Thus, the shorter moderation times predicted by Cohen et al. [31] may account for the lower capture energies of this model with respect to the older theories. Indeed, the moderation times predicted by the diabatic state method (calculated for atomic hydrogen) are in excellent agreement with the experimental values of moderation times in molecular hydrogen [21], whereas the older Born approximation methods [28,29] predict moderation times which are a factor of three or four too long [21]. Nevertheless, this agreement should be viewed with caution since the relation between muon capture in atomic hydrogen and that in molecular hydrogen has not yet been clarified at the low energies involved in the capture process [33]. In [31], the distribution in the principal quantum number n peaks at $n \approx 14$, in agreement with all but [28], while the angular momentum distributions peak at higher values of l than the previously mentioned theories although they show the same sharp cutoff at high l values for large n. It should also be noted that another method, known as the classical trajectory Monte Carlo method [33], produces results which are in general agreement with those of the diabatic state method.

The slowing and capture of muons in molecular hydrogen has recently been investigated by Balashov et al. [34]. The calculations of the ionization and capture cross sections for a muon interacting with a H_2 molecule indicated that the molecular

cross section is at most 40 % larger than the atomic hydrogen cross section at energies above 1 a.u. (27.2 eV). At low muon energies, below ≈ 10 eV, the molecular cross section is calculated to be less than the atomic cross section. The kinetic energy distribution of the muonic molecules formed after the capture of a muon by a hydrogen molecule (not to be confused with energy values quoted earlier, which are the energy distributions of the muons at the time of capture) is predicted to be uniform from zero energy up to a maximum given by $E_m = Im_\mu/M$, where $m_\mu(M)$ is the muon(molecular) mass and I is the molecular ionization potential (15.4 eV in H_2). For moderation in H_2 and D_2 the values of E_m are 0.87 eV and 0.44 eV, respectively. It should be noted that the moderation times predicted with the molecular hydrogen cross sections of Balashov et al. [34] are in fair agreement with experiment [21].

II.3 Atomic Cascade in Muonic Hydrogen

We will again confine the discussion to μp atoms since the behavior of μd atoms should be similar [35]. Although the muon is captured by a hydrogen molecule, it is expected that enough energy will be given to nuclear motion to dissociate the molecule [22], resulting in the formation of a muonic hydrogen atom in a highly excited state. The predicted probability of muon capture into a level of principal quantum number n depends upon the theory employed but typically is expected to peak at $n_m \approx 13$ or 14 and to decrease as n^{-3} for $n > n_m$ [31].

If the muon is captured in a level $n > 14$, the μp atom can lose energy through Auger ionization of neighboring H atoms or by the chemical process

$$(\text{II-3}) \qquad (\mu p)_E + H_2 \rightarrow \mu H_3^+ \rightarrow (\mu p)_{E'} + H + H$$

where the final μp kinetic energy E' is at least 4.5 eV (the H_2 dissociation energy) less than the initial kinetic energy E. The cross section for this process has been estimated as $\sigma_{ch} \approx \frac{1}{3}\pi a_{n\mu}^2$, where $a_{n\mu}$ is the Bohr radius of a muon with principal quantum number n [36]. The size of a μp atom when the muon is in the level $n_\mu = 14$ is approximately the size of an ordinary hydrogen atom with an electron in the level $n_e = 1$. Therefore, the rate for reaction (II-3) will decrease substantially as the muon de-excites toward the 1S ground state, where the μp atom is roughly 200 times ($\approx m_\mu/m_e$) smaller than an ordinary H atom.

Transitions from high n states can also be induced by Coulomb de-excitation [37,38]. The rate for this process is dependent upon the kinetic energy of the μp atom as well as the density of H_2 molecules, and transitions of $\Delta n = 1$ are favored [37]. Coulomb de-excitation rates have been predicted to be the dominant process at high n, decreasing with n until the rates for Coulomb and Auger processes become comparable at $n \approx 10$ [37]. However, recent calculations have indicated that the Coulomb rates may be two orders of magnitude smaller than previously predicted and hence this mechanism may be relatively unimportant [38]. According to Menshikov [38], once the muon reaches the $n \approx 14$ level, the μp atom will de-excite to the ground state through a combination of Auger, radiative, and Stark mixing processes [39].

The external Auger effect

$$(\mu p)_n + H_2 \rightarrow (\mu p)_{n'} + H_2^+ + e^- \qquad \text{(II-4)}$$

is a collision induced (and hence density dependent) radiationless transition from an initial state n to a final state n'. The Auger process favors transitions between levels which result in as small a change in n as is possible while still providing enough energy to eject an electron [40]. The average rate of Auger de-excitation in liquid hydrogen (for a μp KE of $\approx$ 1 eV) is given by

$$\Gamma^A = (4.3 \times 10^{15}\ s^{-1}) \cdot (R_n^{n'})^2 \cdot M^{-2} (2\Delta E + 1.39)^{-\frac{1}{2}} \qquad \text{(II-5)}$$

where $R_n^{n'}$ are the hydrogen radial matrix elements averaged over the angular momentum quantum number l, M is the reduced mass of the μp atom, and $\Delta E = \Delta E_{\mu p} - I$ with $\Delta E_{\mu p}$ representing the energy loss of the μp atom and I = 15.2 eV is the ionization potential of H_2 [36].

The radiative transition rates are given by

$$\Gamma^R = \frac{4}{3} \cdot (1.6 \times 10^{10}\ s^{-1}) \cdot (\delta E)^3 \cdot (R_n^{n'})^2 M^{-2} \qquad \text{(II-6)}$$

where δE is the energy difference between the μp atom states n and n'. These rates are related to the radiative rates in ordinary hydrogen Γ_n^r by $\Gamma^R = M\Gamma_n^r$ [36]. In contrast to Auger transitions, the radiative rates are higher for transitions which result in a maximum change in n levels and become more important as n decreases. It is expected that $\Gamma^A \gg \Gamma^R$ for large n, with the value of n at which radiative transitions become important being density dependent [39], with $\Gamma^A \sim \Gamma^R$ at $n \approx 5$ in STP hydrogen (1 atm, 273K) [37].

As the small, neutral μp atom passes near or through a hydrogen atom it will experience an electric field of 10^9 - 10^{13} V/cm which induces Stark mixing transitions in the μp atom among the n^2 degenerate states for a given n [41]. Due to the domination of the nP->1S radiative transition rates over all the others, higher P states are depleted rapidly and then refilled by Stark mixing. The result is a larger nP->1S transition rate than would be expected in the absence of Stark mixing [42]. The rate of transitions in liquid hydrogen from a state with quantum numbers n,l to a state n,l-1 due to Stark mixing (for a μp KE of

$\approx$ 1 eV) is [36]

$$(II\text{-}7) \qquad \Gamma^S = (4 \times 10^{16}\ s^{-1}) \cdot n(n^2 - l^2)^{\frac{1}{2}} \cdot M^{-1}$$

The initial population among the n^2 degenerate states of a given n is expected to be statistical since $\Gamma^S \gg \Gamma^A$ and $\Gamma^S \gg \Gamma^R$ (down to densities near STP conditions). For densities below STP, the mixing of the different l sub-levels is not complete since $\Gamma^S \sim \Gamma^R$ [39].

The importance of the Stark mixing and Auger (at high density) processes have been demonstrated by experiment. The ratio R of the $K\alpha/K_{tot}$ x-ray transitions (where $K_\alpha \equiv 2P\text{->}1S$, $K_\beta \equiv 3P\text{->}1S$, $K_\gamma \equiv 4P\text{->}1S$, and $K_{tot} \equiv K_\alpha + K_\beta + K_\gamma + \ldots$) was found to be 0.7 $\pm$ 0.2 in liquid hydrogen [41] and 0.42 $\pm$ 0.10 in gaseous hydrogen at 4 atm, 293 K [42]. Since the rate of Stark collisions is higher at liquid densities than it is at 4 atm, one might expect an enhancement of higher nP->1S transitions and thus a smaller value of R in the liquid as opposed to the gas. The near equality of the above results indicates the importance of Auger transitions at liquid densities, these being expected to dominate radiative transitions down to a level of n=4 [36]. This tends to decrease the number of higher nP->1S x rays, resulting in a larger value of R [41]. Also, the analysis of the gaseous hydrogen data indicated the need for a large amount of Stark mixing in order to explain the observed ratio of K_α/Ktot muonic x-ray transitions [39,42]. In addition, a high rate of Stark mixing is needed to explain the short π^- cascade time in liquid

hydrogen, otherwise the estimated transition times would be an order of magnitude longer than the observed cascade time [40].

Recent experiments in very low pressure H_2 gas indicate that the cascade time (t_c) for a μp atom to reach the 1S ground state has an upper limit of $t_c < 200$ ns at a pressure of 0.25 torr, and $t_c < 70$ ns at 1.0 torr [43], which can be compared to the theoretical estimate of Burbidge and De Borde [44] of $t_c \approx 200$ ns for a pure radiative cascade. These results, in combination with the extrapolation of the theoretical cascade times of pionic hydrogen to pressures below 1 atm [45], indicate that the cascade time for muonic hydrogen at a pressure of 94 mbar ($\approx$ 70 torr) is less than a few ns, and will be shorter for higher pressures. Thus, after formation the $\mu p(\mu d)$ atoms can be considered to cascade promptly into the 1S ground state.

II.4 Scattering of μd atoms in D_2

After reaching the 1S ground state muonic hydrogen atoms begin to diffuse through the gas in which they were formed. The subsequent behavior of the μd atoms (neglecting, for now, processes which prevent a μd atom from attaining a foil surface) is determined by two factors - the initial energy of the μd atom upon reaching the ground state and the strength of the cross sections for the scattering process

$$(\mu d)_F + d \rightarrow (\mu d)_{F'} + d \qquad \text{(II-8)}$$

where F and F' represent the hyperfine state of the μd atom before and after the collision, respectively. (The problem of scattering from D_2 molecules is discussed below.) Initially, the μd atoms are formed in a statistical mixture ($\propto$ 2F+1) of hyperfine spin states, i.e. two-thirds are in the quartet state (F=3/2) and one-third are in the doublet state (F=1/2). The magnitude of the cross sections which govern process (II-8) depends upon the energy of the μd atom as well as the hyperfine state that the μd atom is in at the time of collision. These collisions can be divided into two classes - elastic collisions in which the hyperfine state (before the collision) is preserved (F=F') and spin-flip collisions which result in a transition between hyperfine states (F≠F').

The theoretical description of the three body process μ,d, and d (II-8) has often been performed in the adiabatic representation. This consists of expanding the wave function of a

system of three particles, which interact according to Coulomb's law, in terms of the wave functions of the two-center problem [46]. The method of solution involves the perturbed stationary state (PSS) (also known as the molecular wave function) method, which uses the idea that for slow ($v_{\mu d}$ « orbital velocity of the electron) collisions the motion of the heavy particles are adiabatic. The solution using the PSS method involves solving a system of coupled Schrödinger equations, which can be reduced using the two-state (or two-level) approximation [47] to a set of two coupled equations [46]

$$\text{(II-9a)} \quad \left[\frac{d^2}{dR^2} + k_1^2 - \frac{l(l+1)}{R^2}\right] \chi_1 = K_{11}\chi_1 + K_{12}\chi_2 + 2Q_{12}\frac{d\chi_2}{dR}$$

$$\text{(II-9b)} \quad \left[\frac{d^2}{dR^2} + k_2^2 - \frac{l(l+1)}{R^2}\right] \chi_2 = K_{21}\chi_1 + K_{22}\chi_2 + 2Q_{21}\frac{d\chi_1}{dR}$$

or in matrix form

$$L\chi = K\chi + 2Q\frac{d\chi}{dR}$$

where R is the distance between deuterium nuclei, l is the total orbital angular momentum of the three-body system, and K and Q are the effective potentials.

The magnitude and energy dependence of the scattering cross sections used in this work come from the effective two-state approximation, which allows calculations of the cross sections to an accuracy of 10-20 % [12]. This method solved the set of coupled equations (II-9) in the diabatic representation, which is related to the adiabatic basis by a transformation W such that

$\Psi=W\chi$ and allows equations (II-9) to be written without the first derivative terms [48]. In matrix form the equations of (II-9) then become

$$\text{(II-10)} \qquad L\Psi = V\Psi$$

where L is defined as in equation (II-9) and

$$k_1^2 = \frac{2M\epsilon}{\epsilon_a} \quad , \quad k_2^2 = \frac{2M(\epsilon - \Delta E)}{\epsilon_a} \quad , \quad \epsilon_a = \frac{m_a e^4}{\hbar^2}$$

$$\text{(II-11)} \qquad M = \frac{M_1}{m_a} \quad , \; M_1^{-1} = (m_\mu + M_a)^{-1} + M_b^{-1} \; , \; m_a^{-1} = m_\mu^{-1} + M_a^{-1}$$

$$\Delta E = E_b - E_a = \frac{m_\mu}{2}\left[\left(1 + \frac{m_\mu}{M_a}\right)^{-1} - \left(1 + \frac{m_\mu}{M_b}\right)^{-1}\right]$$

where M_a, M_b, are the masses of the hydrogen nuclei a and b, m_μ is the muon mass, and ϵ is the collision energy in the center of mass frame [12]. In the case of μd scattering from deuterium nuclei ($M_a = M_b$) $\Delta E = 0.0485$ eV, the energy difference between the two hyperfine state levels in the μd atom.

Solutions to (II-10) were sought in the form

$$\text{(II-12)} \qquad \Psi(R) = [u + vT(R)]A(R)$$

where u and v are diagonal matrices composed of the two linearly independent solutions of the differential equation $L\Psi = 0$ [49], A is a matrix which relates the effective potential V to the potentials of the two-center problem U, i.e. $V = AUA^{-1}$, and the reaction matrix T is related to the scattering matrix S by [12]

$$\text{(II-13)} \qquad S = (1 + iT)(1 - iT)^{-1}$$

The values of the cross section for a given value of the total spin of the three-body (μd,d) system ($S = F + S_d$, with the deuteron spin $S_d = 1$) then follows from [50]

$$\text{(II-14)} \qquad \sigma^S_{ij} = \left(\frac{\pi}{k_i^2}\right) |\delta_{ij} - S_{ij}|^2$$

where i corresponds to the hyperfine state before collision, j to the hyperfine state after collision, and where i or j equal to one(two) corresponds to the lower(upper) hyperfine state.

If transitions between hyperfine states are possible then it is said that both reaction channels are open, i.e. the μd atom can either remain in the same hyperfine state after collision or it can make a hyperfine transition to the other state. There are also situations in which only one reaction channel is open. If the μd atom is in the lower hyperfine state before the collision and the available kinetic energy in the center of mass frame is less than the hyperfine splitting, then the spin-flip reaction channel σ_{12} is closed since the energy available is insufficient for this reaction. Also, since the cross sections for spin-spin and spin-orbit transitions which change S are several orders of magnitude smaller than the spin-flip cross sections, the total spin S is conserved in process (II-8) [50]. Thus, in collisions in which the μd atom is in the upper hyperfine state and S = 5/2, spin-flip transitions are forbidden and therefore only one reaction channel is open.

When both reaction channels are open the cross section is given by

$$\sigma_{ij}^{S} = \frac{4\pi a_m^2}{k_i^2} \sum_{l} (2l + 1) \frac{\delta_{ij} D_l^2 + (t_{ij}^l)^2}{(D_l - 1)^2 + (t_{11}^l + t_{22}^l)^2} \quad \text{cm}^2$$

(II-15)

$$D_l = t_{11}^l t_{22}^l - (t_{12}^l)^2 \qquad , \quad a_m = \frac{\hbar^2}{m_a e^2}$$

for total orbital angular momentum l (l=0 s-wave, l=1 p-wave, etc.), $a_m = 2.70344 \times 10^{-11}$ cm for the process (II-8), and t_{ij} are the elements of the reaction matrix T provided by Bubak and Faifman [12]. If one reaction channel is closed then

$$\sigma_{ii}^{S} = \frac{4\pi a_m^2}{k^2} \sum_{l} \frac{(2l + 1) (t_{ii}^l)^2}{1 + (t_{ii}^l)^2} \quad \text{cm}^2 \qquad \text{(II-16)}$$

It should be noted that the energies at which the matrix elements t_{ij} are provided in reference [12] are defined in such a way that for $\epsilon < \Delta E$, the tabulated energy is related to the lower hyperfine energy level, and for $\epsilon > \Delta E$ the tabulated energy is related to the upper energy level. When computing σ, for all cases $k^2 = 2ME_t/\epsilon_a$ where E_t is the tabulated energy provided in [12], except when computing σ_{11} for cases when the kinetic energy of the μd is larger than the hyperfine splitting. In this case $E_t' = E_t + \Delta E$ should be used in calculating k^2. In summary, equation (II-15) is used to calculate σ_{11} ($\epsilon > \Delta E$), σ_{21}, and σ_{22} when S = 1/2,3/2; equation (II-16) is used for σ_{11} ($\epsilon < \Delta E$) and also for σ_{22} when S = 5/2. The total cross section then follows from

$$(II\text{-}17) \qquad \sigma_{FF'} = \sum_{S} W_{FS} \cdot \sigma^{S}_{FF'}$$

where the statistical weights W_{FS} are

$$(II\text{-}18) \qquad W_{FS} = \frac{2S + 1}{(2F + 1)(2S_d + 1)}$$

This method does not take into account the effects of molecular structure (the μd scatters from D_2 molecules in the gas) and electron screening (scattering from atoms instead of nuclei). Calculations of the influence of molecular structure on the scattering cross sections have been performed, but only up to a collision energy of 0.25 eV [51,52]. Electron screening has also been taken into account for collision energies up to 0.25 eV [53] and to 1.0 eV [54]. These calculations show that including electron screening has < 10 % effect on the nuclear cross section values for $\epsilon > 0.10$ eV, below which this effect becomes more important. Thus, the treatment of Bubak and Faifman [12] does not encompass all of the complicated mechanisms involved in the scattering process. Nevertheless, it offers an advantage over other theoretical work in that it presents tables of numbers (matrix elements from which cross sections can be computed) over a wide collision energy range ($0.001 \leq \epsilon \leq 50$ eV).

As mentioned earlier, there are certain processes to which the μd atom is subjected as it diffuses which result in the destruction of the μd atom. Some of these inelastic processes are shown in Table II [55]. The rates for processes (b) and (c) are the rates at which these processes would occur at the liquid

Table II
Experimental Rates of Inelastic Processes in μd Diffusion

Process		Rate (x 10^5 s^{-1})
(a)	$\mu^- \rightarrow e^- + \bar{\nu}_e + \nu_\mu$	4.55135 ± 0.00014
(b)	$\mu d + d \rightarrow d\mu d$	23.4 ± 0.17
(c)	$\mu d + {}_zY \rightarrow \mu_zY + d$	$\sim$2.5 x 10^6
(d)	$\mu^- + d \rightarrow n + n + \nu_\mu$	(4.45 ± 0.60) x 10^{-3}

hydrogen density of N = 2.11 x 10^{22} molecules·cm^{-3}. Thus, the rate given for process (c) is that when the density of the impurity ${}_zY$ is N and the μd is thermalized. Therefore, at the pressures used in this experiment (p ≤ 1.5 bar), dμd molecular ion formation (process (b)) occurs at a negligible rate. The high rate of process (c) emphasizes the importance of keeping the deuterium gas free of impurities. The rate of muon absorption by a deuteron (process (d)) is given for the μd atom residing in the doublet state (F=1/2). Capture rates from the quartet state are expected to be about forty times smaller than this [55]. Thus, it can be seen that the only inelastic process of any consequence during the μd diffusion process in this experiment is that of muon decay (process (a)). The effect of the decay of the muon is to cause the number of μd atoms reaching the foil per stopped muon in the gas to be less than unity. Since the muon

decay rate is known with high precision its effect can be readily accounted for (§IV.5).

II.5 Muon Transfer

After diffusing through the deuterium gas in which it was formed the μd atom will eventually strike a foil surface composed of atoms ${}_{Z}Y$ with atomic number Z (if it is not lost to an inelastic process (§II.4)). The μd atom will dissociate when it experiences the electric field of the nucleus as it penetrates the electron cloud of the atom ${}_{Z}Y$ [56]. Although the dimensions of the μd atom are quite small (the muonic Bohr radius $a_{\mu} = 2.56 \times 10^{-11}$ cm) there exists a large cross section for the transfer process

$$(II\text{-}19) \qquad \mu d + {}_{Z}Y \rightarrow (\mu_{Z}Y)^{*} + d \rightarrow (\mu_{Z}Y)_{1S} + d + x \text{ rays}$$

This process results in the creation of a muonic atom in an excited state $(\mu_{Z}Y)^{*}$, which de-excites to the 1S ground state via Auger and radiative transitions [57]. Thus, during the cascade a characteristic set of muonic x rays is released which serves, upon detection by germanium detectors, as a signal that the μd atom has arrived at the foil surface and therefore as a signal that the diffusion process is complete.

The transfer of the muon to a nucleus ${}_{Z}Y$ occurs at an intranuclear distance R given by

$$(II\text{-}20) \qquad R \approx 4n^{2}\sqrt{Z}a_{\mu}$$

where n is the level of the μd system at the time the transfer takes place [58], which can be taken as n=1 (§IV.3). Therefore,

the transfer probability is not expected to depend on the molecular structure of the medium containing $_{Z}Y$ since the distance R is so close to one of the nuclei that the variation of the electron charge distribution due to any molecular structure can be neglected [58]. The transfer rate from the 1S ground state of the μp atom has been estimated to be

$$\text{(II-21)} \qquad \lambda \approx (6.5 \times 10^{10}) \cdot Z^{2/3} \cdot w(Z) \qquad s^{-1}$$

where the transfer factor w(Z) increases with Z and lies in the range $0.3 < w(Z) \leq 1.0$ [59]. The rate (II-21) has been normalized to a density n of 4.22×10^{22} atoms/cm^3 - the density of liquid hydrogen. Fiorentini and Torelli [59] predict that the transfer cross section σ will vary inversely as the square root of the μd KE in the energy range .038 eV $\leq$ KE $\leq$ 1 eV. Therefore, the predicted transfer rate $\lambda = n\sigma v$ is independent of the μd velocity in this KE range. Experimentally, the transfer rate exhibits a mass dependence and for a μd-$_{Z}Y$ system is half that of a μp-$_{Z}Y$ system [60].

The atomic shell N to which the muon is transferred from an initial μd level n is given (for high Z) by [59]

$$\text{(II-22)} \qquad N \approx \sqrt{2} n Z^{3/4}$$

The newly formed $\mu_{Z}Y$ atom de-excites from this high N state through internal Auger and radiative processes, with Auger processes dominating for high N and radiative processes becoming more important as N decreases. The region in N for which the cascade goes from pure Auger to pure radiative is usually quite

narrow [61]. For levels with principal quantum number N and angular momentum L the radiative transitions with $\Delta L = -1$ are generally two to three orders of magnitude larger than radiative transitions with $\Delta L = 1$, while the Auger transitions also favor $\Delta L = -1$ and $\Delta N = -1$ when ΔN is large enough to make electron ejection energetically possible [61]. Thus, the radiative and Auger processes tend to push the muons into "circular" orbits in which L = N-1 . Also, the intensities of transitions between circular orbits (N,L=N-1 -> N-1,L=N-2) have been found to increase with increasing Z [57].

Experimentally, an enhancement of higher (N>2) K-series (NP->1S) x rays compared to K_α (N=2) x rays has been observed in cases when the $\mu_Z Y$ atom is formed through a transfer process (e.g II-19) as compared to direct formation of a $\mu_Z Y$ atom from muons stopping directly in the target medium [62]. Such an enhancement has been observed for target atoms with $Z \leq 18$, whereas for high Z (Z=54) this enhancement has disappeared [63]. By adjusting atomic cascade models so that the initial L-distribution of the $\mu_Z Y$ atoms formed by transfer is weighted towards lower L-states than when the $\mu_Z Y$ atom is formed from direct stops, the observed K-series enhancement in low Z targets can be reproduced [62]. In addition, it has been observed that this enhancement is roughly twice as great when the muon is transferred from a μp atom as it is when the muon is transferred from a μd atom. This may indicate that the initial L-distribution of the $\mu_Z Y$ atom is weighted to higher L-states after transfer

occurs from a μd atom as compared to a μp atom [64].

Once the muon has cascaded to the 1S ground state, it will either decay or be absorbed by the nucleus, with the probability for absorption increasing with increasing Z. In this experiment Au (Z=79, where the μ lifetime is $\approx$ 70 ns (see §IV.3)) was used as the transfer medium so that virtually all ($\approx$ 97 %) of the muons are absorbed by the Au nucleus. The absorption of the muon will usually leave the nucleus in a highly excited state, with de-excitation occurring through the emission of one or more neutrons followed by γ-ray emission from Pt (Z=78) [65]. Thus, since the muon cascade to the 1S state in the excited $(\mu_Z Y)^*$ atom formed after transfer (or direct stops) occurs promptly ($\leq$ 1 ps [44]) and the absorption time of the muon in Au can be taken into account (§IV.3), these γ rays can also serve as a signal that the μd atom has arrived at the foil surface.

II.6 Time Scale of the Experiment

In order to get an estimate of the time scale involved in this experiment, we determined the time distribution of μd atoms striking the foils under certain simplifying assumptions. The μd atoms are assumed to form uniformly in the gas gap between the foils and begin their diffusion process in a random, isotropic direction. Furthermore, the gas pressure is assumed to be so low that the mean free path of the μd atoms in the gas is much greater than the spacing between the foils, i.e. all of the μd atoms reach the foils without experiencing any scattering along the way. In this case, the arrival time of the μd atoms at a foil surface (many of these times are collected to form a time distribution) will depend solely upon the initial velocity distribution of the μd atoms (initial means in the 1S state) and the foil spacing. For simplicity it is convenient to assume that all the μd atoms are formed with the same kinetic energy so that the initial velocity distribution is represented by a delta function, i.e. $f(v) = \delta(v - v_0)$. With these assumptions and for a geometry consisting of semi-infinite planes separated by a distance L, the probability distribution P(t) for μd atoms hitting the foil at a time t is given by [66]

$$P(t) = \begin{cases} \dfrac{v_0}{2L} & t < \dfrac{L}{v_0} \\ \dfrac{L}{2v_0 t^2} & t > \dfrac{L}{v_0} \end{cases} \qquad \text{(II-23)}$$

as shown by the solid curve in Figure 1 (see Appendix B). The appropriate time scale under these assumptions is then L/v_0, which for a μd atom with an initial kinetic energy of 1.0 eV and a foil spacing of about 2 mm is $\approx$ 200 ns.

If the above assumptions hold, deviations from the shape of P(t) in Figure 1 would be due to either an initial μd velocity distribution which was not a delta function (see the dashed curve of Figure 1) or the presence of scattering (neglecting detector resolution). For example, increasing the pressure (and hence the scattering probability) would leave P(0) unaffected (since μd atoms which strike the foil at t=0 must originate from adjacent to the foil surface regardless of the pressure and foil spacing used) but would change the shape of P(t) near the "cusp" region of Figure 1 (i.e. near $t=L/v_0$). An increase in pressure would increase, on average, the time it takes for a μd atom to hit a foil surface and thus have the effect of redistributing the events (for t>0) in Figure 1 to longer times. The result would be an apparent "peaking" of the time distribution toward t=0 as the pressure increased.

Chapter III

EXPERIMENTAL METHOD

III.1 Introduction

The experiment was performed in the μE4 area of the Paul Scherrer Institute (PSI - formerly the Swiss Institute for Nuclear Research (SIN)) in Villigen, Switzerland. The data were gathered in three sets - a two week run in May 1987, a four week run in August 1987, and some additional D_2 data were gathered in June 1988. The May 1987 run served mainly as a test of the apparatus and yielded some preliminary data. The bulk of the data were recorded during the production runs in August 1987 and June 1988.

The experiment can briefly be described as follows. A beam of negative muons was brought to rest inside an aluminum target vessel containing a number of planar, Au-coated plastic foils. The foils were separated by a few mm, with the interstitial volumes containing deuterium gas. A small percentage of the incident μ^- stopped in the gas region and formed μd atoms. After diffusing through the D_2, a fraction of the μd atoms (which fraction depended upon the gas pressure and foil spacing used) impinged upon a foil, whereupon the muons were transferred to the Au on the foil surface. This process resulted in the formation of

muonic Au atoms, initially in excited states. De-excitation to the 1S ground state would occur within a picosecond [44] through the release of one or more muonic Au x rays. After absorption of the muon in the Au nucleus, nuclear γ rays from Pt would also be emitted. The detection of these emitted photons by one of a set of intrinsic Ge γ-ray detectors surrounding the target vessel served as the signal that the μd atom had arrived at the foil surface. This arrival time (resulting from a true diffusion event), together with the energy of the detected photon were processed by the data acquisition system and stored on magnetic tape. The vast majority of the muons would stop directly in the foils themselves, and the energy and time of detection of the photons related to these events were also recorded.

As discussed in Chapter I, the purpose of the experiment was to gather sufficient information on the diffusion process to be able to design a muon absorption experiment in gaseous hydrogen. Specifically, it is necessary to determine the initial velocity distribution of the μd atoms after they have reached the 1S state, and also to estimate the scattering of the μd atom in a given experimental condition.

The initial velocity distribution of the μd atoms will be modified by scattering. It is thus desirable to work at a gas pressure low enough to assure that the μd atom formed in the gas gap will have a high probability of reaching the foil surface without scattering (of course some muons will decay en route to the foil). Just how low the pressure must be depends upon the

magnitude of the scattering cross sections for the process

$$\mu d + D_2 \rightarrow \mu d + D_2$$

Extensive theoretical calculations exist [12 and references therein] for μd scattering from deuterium nuclei (§II.4) and are important for the data analysis (§IV.5). However, a different approach is required to determine this low scattering limit during the experimental runs. This relies on constructing distributions of the arrival times of the μd atoms at the foil surface. As the pressure is decreased, the shape of this time distribution will change as the amount of scattering also decreases. Eventually an asymptotic shape of the time distribution will be reached at sufficiently low pressure. In this asymptotic limit, the shape depends solely upon the initial velocity distribution of the μd atoms and the target geometry (neglecting the time resolution of the germanium detectors). Data taken at higher pressures provide information on the scattering cross sections.

III.2 Experimental Conditions

The May 1987 run tested the apparatus with deuterium gas at pressures of 7.85,2.56, and 1.28 bar using a 50 foil single gap foil stack with a total length of 11.5 cm. Single(double) gap refers to a spacing of 2.3(4.6) mm between the foils. Initially, a high pressure of 7.85 bar was chosen in order to insure a high stop rate of muons in the gaseous regions between the foils. In addition to runs made with deuterium gas, checks of background were made with a He target filling. The He pressures were adjusted to give the same stopping power as the D_2 runs mentioned above. Muons stopping in He would form μHe atoms which, due to their positive charge, would not transfer their muons to the Au surface layer on the foils. A comparison of energy spectra for D_2 and He runs could then be made. Photopeaks which appeared in the energy spectra taken with He gas could not be diffusion related, and were therefore considered to be background.

After preliminary analysis of the May 1987 data, it was clear that pressures below 1 bar would be needed to attain conditions in which the shape of the time distribution (for arrival of the μd atom at the foil surface) would not be visibly affected by a reduction in pressure. Therefore, in August 1987 runs with D_2 pressures of 1.52,0.750,0.375, and 0.188 bar with a 50 foil single gap stack and 0.750,0.375, and 0.188 bar with a 30 foil double gap stack were made. Use of a double gap stack provided additional information for analysis, and constrained the

interpretation of the data. In addition to a D_2 filling, runs with the target vessel evacuated were performed using both the single and double gap foil stacks. Also, runs in which a solid Au target was placed in the beam line (replacing the target vessel containing the foil stack) were performed. The necessity of these runs will be discussed in §IV.2.

III.3 Target

The target consisted of a set of Au-coated plastic foils which were bolted together to form a foil stack. The foil stack was placed inside an aluminum pressure vessel which was connected to a gas/vacuum system. The whole assembly, including the gas system, was mounted on wheels to facilitate the movement of the target up to the beam pipe vacuum window.

The foils were constructed of 9 μm thick Kynar ($C_2H_2F_2$) foil with 100 $\pm$ 10 Å thick layers of Au deposited on each surface. Analysis with a transmission electron microscope confirmed that the Au had been deposited uniformly on the Kynar surface. There also was no evidence of any penetration of the Au into the Kynar [67]. The 10 cm diameter foils were ultrasonically welded to a 2.3 mm thick kynar ring of inner diameter 10 cm and outer diameter 13.3 cm. These foils could then be connected using three bolts to form a foil "stack" of variable length, with 2.3 mm gaps in between the foils through which the gas would flow. Aluminum clamp rings were mounted on each end of the foil stack in order to achieve uniform compression of the stack when the nuts were tightened. A kynar ring was mounted on top of these clamp rings to prevent beam muons from striking these metal surfaces. A double gap foil stack with 4.6 mm gaps between the foils could be formed by inserting a kynar ring, to which no foil had been attached, between each foil.

There were several advantages to using Au-coated Kynar to

comprise the foil stack. The plastic Kynar was chosen as the major component of the foil stack for its stability in vacuum and low vapor pressure. Thus, contamination of the D_2 gas resulting from the outgassing of impurity atoms from the foils was minimized. The benefits of coating the foils with a thin, high Z layer are related to the distribution of arrival times of the μd atoms at the foil surface. With the foil composition mentioned above, a 2.3 mm gap of D_2 at 1 bar will have $\approx$ 1 % of the stopping power of the foils themselves. Therefore, most of the beam muons will stop in the foil (principally in C or F atoms), thereby producing a large number of background events near zero time, where zero time is defined as the time the muons enter the target vessel. This "prompt" time signal can overwhelm the signals produced by the diffusion process at early times. The loss of information at early times can be minimized by coating the foils. Then the element to which muon transfer takes place has relatively little stopping power (at a pressure of 1 bar the stopping powers of 2.3 mm of D_2 and 100 Å of Au are roughly equal), allowing the distribution of μd arrival times at the foil to be measured close to time zero. Furthermore, if a high Z coating is used, many of the photons emitted after transfer to the high Z material will have energies well above the energies of K-series μC and μF x rays. This helps to reduce the level of background under the diffusion related photopeaks, which in turn enables a time distribution to be extracted with improved precision.

The thickness of the Au layer on the foils was chosen so

that the predicted transfer probability of a muon from a μd atom to Au would be fairly large. This thickness was determined in the following manner. The muon transfer cross section (for μd atoms in Au) was estimated by using the experimental transfer rate of muons from μp atoms to Xe (Z=54) [68] and scaling by the predicted Z dependence of the transfer rate [59], then halving this rate due to the experimental mass dependence of the transfer rate [60] (§II.5). The result was an estimated transfer cross section for μd atoms in Au of $\approx 8 \times 10^{-17}$ cm^2. Then, using the predicted energy dependence of the transfer cross section [59], this would yield a mean free path of a μd atom in Au (before transfer occurred) of $\approx$ 20 Å at .038 eV and $\approx$ 100 Å at 1.0 eV. Thus, a 100 Å thickness was chosen as a good compromise between minimizing the prompt stops in the Au layer and maximizing the transfer probability of the muons to the Au layer.

The spacing, or gap, between the foils will clearly influence the diffusion process. If the gap size is increased then the stopping power of the gas relative to that of the foils is increased resulting in an improved muon stop rate in the gas. However, the wider the gap the further a μd atom must travel (on average) before striking the foil. The resulting increase in scattering probability will cause the time that the μd remains in the gap to increase. This will lead to an increase in the number of muons which decay before the μd atom reaches a foil surface. Also, increasing the spacing will make it much more difficult (i.e. require lower pressures) to observe the asymptotic limit

of no scattering between the foils. For a fixed pressure, the chance of a μd atom reaching the foil surface without scattering would increase as the foil spacing is decreased, yet this would reduce the observed transfer signal because of the corresponding decrease in the number of μd atoms formed. Too small a gap would require large amounts of beam time to accumulate reasonable statistics. Also, the tolerance on the uniformity of the foil spacing becomes more stringent as the gap is narrowed. (The uniformity of the spacing between foils was tested by measuring the gap between four foils at five different places on each foil. All measurements of the foil gap were within 2.29 ± 0.07 mm.) A compromise between a gap size that is too large or too small can be reached by estimating the mean free path in D_2 of a μd atom with the expected energy of ≈ 1 eV. If the theoretical scattering cross sections for μd scattering on d [12] are assumed and then scaled by a factor of two to approximate scattering from D_2 molecules, the μd mean free path at 1 bar is ≈ 1 mm.

In May 1987, the foil stack was placed inside a cylindrical aluminum target vessel, with a formed hemispherical nose upstream. This design allowed for quick transitions to gas pressures above and below one bar. Thus, the need to change target entrance windows was eliminated. The design thus saved time during the short (two week) test run. After the May 1987 run an improved design of the target vessel was implemented at PSI for subsequent runs.

For the August 1987 run, the foil stack was placed inside a

cylindrical aluminum pressure vessel of length 28.0 cm and inner diameter 13.5 cm. This allowed the foil stack to fit tightly inside the target vessel while allowing adequate room for longer foil stacks. The side walls of this pressure vessel were thin (1.5 mm) to minimize the attenuation of x rays emanating from the foil stack but were able to withstand pressures of 10 bar. (Assuming normally incident x rays, approximately 25 % of 350 keV x rays would be absorbed in the material (≈ 1.3 cm Kynar foil holders, 1.5 mm Al side walls, and ≈ 2 mm of plastic scintillator) between the active volume of the target (where μd atoms are formed) and the germanium detectors [69] .) An 0.1 mm thick aluminum entrance window of 8.0 cm diameter was used in this target vessel.

The gas/vacuum system is schematically represented in Figures 2a,2b. The vacuum system, including a fore pump and a turbo molecular pump, and the gas input were connected to the stainless steel back flange of the target vessel. The gas output was connected to the stainless steel front flange, thus requiring the gas to flow through the foil stack and preventing any "short circuit" between incoming and outgoing gas flow from occurring. In order to prevent the build up of impurities in the gas resulting from outgassing of the foil stack and the aluminum pressure vessel itself, the D_2 gas was continually circulated through a palladium purifier. The presence of impurities in the gas was monitored on-line by a quadrupole mass spectrometer. At no time during the August 1987 run were impurities detected in

the gas system. In the May 1987 run, without the benefit of a closed recirculation system including a Pd filter, impurities (N and O) were detected in the gas. However, this was of some use in the analysis (§IV.2.4).

III.4 Data Acquisition

The μE4 experimental area of PSI is shown in Figure 3. The main ring cyclotron produced a 590 MeV proton beam which was extracted and directed towards target station E, where a 12 cm long, 6 mm thick Be target is used for pion production [70]. Pions produced at a 90° production angle (relative to the proton beam direction) are accepted by the quadrupole triplet QTB 61/62/63. Muons generated from pion decay are collected by a 5 m long superconducting 5 tesla solenoid and transported to area μE4. The pions which do not decay in this channel, as well as electrons, are effectively removed from the muon beam by the muon extraction system of Figure 3.

The experimental setup is shown in Figure 4. The target vessel was placed as close as possible to the beam pipe vacuum window, while allowing room for the scintillation counters 2,3, and 3A, in order to minimize the effects of the beam divergence. The target height was adjusted so that the center of the foil stack was at the beam height of 149. cm above the floor.

The detectors A,B, and C, which were housed in one vacuum envelope, were high purity n-type coaxial Ge detectors and were well suited for the detection of photons in the 100-700 keV energy region. The Ge crystals in detectors A,B, and C were 47 mm in diameter and 26 mm in length. Detector GMX was a 17% efficient (with respect to 3"x3" NaI(Tl) at 1.333 MeV) high purity Ge detector. The Ge detectors were placed as close as possible to

the cylindrical target vessel while allowing enough room for the placement of the charged particle veto counters V1 and V2 between the target and the detectors. Together, the active volume of the four Ge detectors subtended ≈ 5% of the available solid angle.

The main functions of the electronics were to record the energies and detection times of photons emitted from the target vessel, as well as to provide appropriate trigger signals. The detection time was taken to be relative to the time a muon entered the target. The energy deposited and time of each detected photon were recorded on magnetic tape for later analysis (Chapter IV).

A simplified block diagram of the electronics is shown in Figure 5. Muons exiting the beam pipe would pass through the scintillator telescope comprised of counters 2,3, and 3A. The dimensions of the scintillator counters are provided in Table III. The entrance of a muon into the target vessel was indicated by the μSTOP coincidence $2 \cdot 3 \cdot \overline{3A}$. Since the Au-coated foils were 10 cm in diameter, it was desirable to accept only those muons which were close to the center axis of the foil stack. Therefore, counter 3A had a 5 cm diameter aperture (which was centered about the center axis of the foil stack) through which the muons were required to pass in order to signal a μSTOP. This allowed for the effects of multiple scattering in the target and the beam divergence during the slowing down process of the muon. A valid μSTOP was placed in anti-coincidence with various deadtimes in the system ($\overline{DT}$).

Table III
Dimensions of Scintillation Counters

Counter	Dimensions (cm)
2	20 x 20 x 0.06
3	5.5 diameter x 0.05
3A	18 x 14 x 0.5 with 5 cm aperture
V1	14 diameter x 0.2
V2	8 x 8 x 0.3

A $\mu\overline{DT}$ anti-coincidence (AC) initiated a 6.1 μs deadtime in which further $\mu\overline{DT}$ AC's were forbidden. A pileup protection prevented subsequent processing if a second muon (identified by a hit in counter 2) was detected within 4 μs of a μSTOP. The $\mu\overline{DT}$ AC also served as the start signal for the time-to-digital converter (TDC) in addition to opening a 5 μs wide gate μGATE. This gate was opened from -1 to 4 μs since the timing signals from the Ge detectors were delayed by 1 μs. It was placed in coincidence with a signal from any of the Ge detectors. If the charged particle veto counter covering the Ge detector did not fire, this indicated that the detected signal was a photon and not a charged particle. The detection of the photon served as the stop signal for the TDC and also initiated analog-to-digital conversion in the ADC. A latch was then set which remained on until reset by a $\mu\overline{DT}$ AC of another incident muon.

The signal EM, which was generated at the end of a μGATE, was delayed by 100 ns to allow for time jitter among the Ge

detectors to form Q1. This began the read-out stage of the system. If a second muon was not detected within 4 μs of a μSTOP, and the system was live, i.e. there was a $\mu\overline{PD}$ (a muon with no pileup - a second muon detected within ±4 us of a μSTOP - and no deadtime), then a MASTER coincidence was formed with the detected photon in one of the Ge detectors and $\mu\overline{PD}$. This coincidence defined an "event" - a detected photon after a μSTOP when there was no rejection due to system deadtimes or pileup protection - and generated an I/O to the μVAXII computer used in the data acquisition system. The absence of a MASTER coincidence generated a fast clear of the ADC's and TDC's.

The stopping distribution of the muon beam was centered in the foil stack by maximizing the number of detected μF(2-1) x rays per μREAL event, where a μREAL event was defined to be a detected muon without any deadtimes or pileup rejections (a coincidence between a $\mu\overline{DT}$ (delayed by 5 μs) and a $\mu\overline{PD}$). An additional check on beam momentum came from observing the strength of a nuclear γ ray from ^{55}Mn. This signal is produced after muon absorption in an iron nucleus in the stainless steel back flange of the target vessel. If the beam momentum was set too high then this photopeak in the energy spectra of the Ge detectors would become prominent, indicating that too much of the beam was stopping in the back flange of the target vessel. The optimal muon momenta were 35 MeV/c for a 50 foil single gap stack and 34 MeV/c for a 30 foil double gap stack. Some typical signal rates are shown in Table IV. The appropriate magnet settings in

the μE4 beam line for the muon momenta 34 MeV/c and 35 MeV/c are provided in Table V.

Table IV
Signal Rates

	Rate (x 10^3 s^{-1})	
Scaler	p_μ = 34 MeV/c	p_μ = 35 MeV/c
2	21.9	23.0
2·3	16.0	17.2
μstop	15.9	16.9
$\mu\overline{DT}$	13.6	13.3
$\mu\overline{PD}$	12.0	12.2
μreal	9.0	9.2
master	0.72	0.76
beam current (μA)	225	225

Table V
Beam Line Magnet Settings

Magnet	p_μ = 34 MeV/c	p_μ = 35 MeV/c
QTB61	+ 2192	+ 2214
QTB62	- 1840	- 1858
QTB63	+ 1080	+ 1090
ASK61	- 1140	- 1151
QSB61	+ 636	+ 654
QSB62	- 350	- 360
QSB63	- 302	- 311
QSB64	+ 514	+ 529
ASK62	- 507	- 521
QTA61	- 1680	- 1700
QSK61	+ 558	+ 574
QSK62	- 598	- 615
QSK63	+ 472	+ 485
Slit Settings (Volts)		
Top	1.75	1.70
Bottom	1.45	1.30
Left	1.30	1.30
Right	1.70	1.70

Chapter IV

DATA REDUCTION AND ANALYSIS

IV.1 Introduction

In the analysis of the data, we were primarily concerned with extracting the time distributions of delayed events. To obtain such distributions we calculated two-dimensional energy versus time spectra for each Ge detector from the original data stored on magnetic tape. The analyzed time region included times from -40 ns to 2.0 μs. This insured the inclusion of the prompt time region as well as the region of interest in the delayed spectrum. The energy and time axes in the two-dimensional spectra were compressed with respect to the original scales by a factor of two due to memory restrictions on the VAX-11/750 used in the analysis. After routine checks of the integrity of the data were performed, data from tapes with identical conditions (foil spacing and gas pressure) were summed. The intensities of the peaks of interest were then determined as a function of time.

IV.2 Data Reduction

IV.2.1 Identification of Photopeaks

The first step in analyzing the data was the identification of photopeaks observed with the Ge detectors. For this purpose, information was needed on the energies of the photopeaks as well as the time evolution of each photopeak.

The energy calibration for each detector was performed using the radioactive sources of ^{57}Co, ^{133}Ba, and ^{137}Cs. The energy of any line in the spectrum could then be determined from the calibration and compared to tabulated values in tables of muonic x rays [71,72] or the Table of Isotopes [73]. Since the identification of signals which were directly related to the diffusion process was of major interest, a solid Au target of 520 mg/cm^2 and $\approx$ 4 cm diameter was used to obtain high statistics signals of photopeaks which would emanate from the Au foil coatings in the target vessel.

IV.2.2 Transfer Signals

The temporal behavior of the photopeaks can be divided into two classes - prompt and delayed. Prompt muonic x rays are emitted during the cascade process after muon capture. A typical prompt spectrum is shown in Figure 6. Examples of the muonic x rays which are prominent in Figure 6 include the K and L-series in fluorine and the K-series in carbon.

The delayed signals arise from true diffusion related events as well as nuclear γ rays produced in the material of the target vessel. These nuclear γ rays are emitted after muon absorption in the target vessel, and thus are delayed with respect to the prompt stops with a lifetime characteristic of the element in which muon absorption occurred. Examples of these are nuclear γ rays from F at 110 and 197 keV. A typical delayed spectrum is shown in Figure 7.

Originally it was planned to use the "circular" transition x rays (§II.5) emitted during the cascade process in the muonic Au atom. The circular x rays range in energy from below 100 keV to above 5 MeV [72] and are produced with a high yield [57] (Table VI). The tabulated transitions were readily detected when the solid Au target was placed in the muon beam (Figure 8). However, as can be seen in Figure 7, there are few delayed muonic Au x rays emitted in the region 50-500 keV during the cascade process <u>after transfer</u>. The μAu(2->1) ($\approx$ 5.6 MeV) and μAu(3->2) ($\approx$ 2.4 MeV) transitions are prominent in the delayed spectra of the GMX detector, and when taking into account the low detector efficiency at these energies, the yields appear to be relatively high ($\approx$50%). All other x ray transitions are much weaker after transfer than they are after direct stops in Au.

In the delayed spectrum of Figure 7, there are delayed signals other than muonic Au x rays which are directly related to the diffusion process - nuclear γ rays from Pt. These are emitted after completion of the cascade process, when the

Table VI
Circular X-Ray Transitions in μAu

Transition	Energy (keV)	Yield
$2P_{3/2} \rightarrow 1S_{1/2}$	5764.89[1]	0.90
$2P_{1/2} \rightarrow 1S_{1/2}$	5594.97[1]	
$3D_{3/2} \rightarrow 2P_{1/2}$	2474.032	0.80
$3D_{5/2} \rightarrow 2P_{3/2}$	2341.246	
$4F_{5/2} \rightarrow 3D_{3/2}$	898.792	0.76
$4F_{7/2} \rightarrow 3D_{5/2}$	869.979	
$5G_{7/2} \rightarrow 4F_{5/2}$	405.591	0.68
$5G_{9/2} \rightarrow 4F_{7/2}$	400.093	
$6H_{9/2} \rightarrow 5G_{7/2}$	217.701	0.68
$6H_{11/2} \rightarrow 5G_{9/2}$	216.226	
$7I_{11/2} \rightarrow 6H_{9/2}$	130.961	0.49
$7I_{13/2} \rightarrow 6H_{11/2}$	130.452	
$8J_{13/2} \rightarrow 7I_{11/2}$	84.081	0.29
$8J_{15/2} \rightarrow 7I_{13/2}$	83.880	
$9K_{15/2} \rightarrow 8J_{13/2}$	57.606	0.29
$9K_{17/2} \rightarrow 8J_{15/2}$	57.513	

[1] Energies taken from reference [71]
All other energies from reference [72]
Yields from reference [57]

muon has reached the 1S state of the μAu atom. The muon is then absorbed by the Au nucleus (Z=79) (since only a few percent decay in Au), which often leaves the nucleus in an excited state. De-excitation occurs with the emission of one or more neutrons followed by γ-ray emission from Pt (Z=78) [65]. Such nuclear γ rays were used as a transfer signal, which has both positive and negative aspects. On the negative side, these γ rays are not emitted promptly (as are muonic x rays) after the μd atom transfers its muon to a Au atom. Instead, they are emitted with a time delay which has a mean life of $\approx$ 70 ns (§IV.3) which corresponds to the muon lifetime in gold. This implies that features in the time distribution of delayed events which occur on a time scale of $\leq$ 70 ns cannot readily be resolved. A positive aspect is that one is assured that the emission of the transfer signal is largely independent of the cascade process, and therefore independent of the energy of the μd atom at the time it encounters the foil surface. The emission of Pt γ rays is not completely independent of the cascade process, since it is possible for the muon to excite low-lying nuclear levels during the cascade. Such radiationless transitions are possible when a forbidden muonic transition (e.g. 2S->1S) is close in energy to a nuclear excitation [74]. Experimental data on this process in Au is not in the literature, but the probability for radiationless transitions in ^{209}Bi (Z=83) which result in neutron emission has been found to be 7 $\pm$ 2 % [75]. Thus, while it remains unclear whether this process is dependent upon the energy of the muon at

the time of transfer, it appears that radiationless transitions play a relatively small role in the cascade process.

Also prominent in the delayed spectrum of Figure 7 are two electronic x rays from Pt at energies of 65.1 and 66.8 keV. These x rays are emitted both promptly and with the characteristic 70 ns absorption time of muons in Au. Due to a lack of complete understanding of this "hybrid" time structure, these x rays were not included in the analysis.

IV.2.3 Time Distributions

The analysis of the data involved creating two-dimensional energy versus time histograms for each Ge detector. Two energy regions were analyzed - spanning 60 to 107 keV and 320 to 362 keV. The lower energy region contained Pt electronic x rays at 65.1 and 66.8 keV, the K-series in μC and the μN(2-1) transition. The μC lines were analyzed for monitoring purposes (and see also §IV.2.4). The μN line served as a check for impurities in the gas. The high energy region contained two nuclear γ rays from ^{196}Pt (a 326.2 keV transition was also present but it was too weak to be used as a transfer signal) and one from ^{194}Pt (see Table VII). All other Au or Pt transfer signals were considered to be too weak to be useful - i.e. their inclusion would not significantly improve the obtained precision in the time distribution. The yield of the 328 keV γ ray was determined by scaling the yield of the 333 keV γ ray [65] by the

Table VII
Nuclear Gamma Rays from Pt Used as Transfer Signals

Isotope	Energy (keV) [1]	Yield [2]
^{196}Pt	355.7	0.36 ± 0.05
^{196}Pt	332.9	0.11 ± 0.02
^{194}Pt	328.45	≈ 0.10

[1] taken from reference [73]
[2] taken from reference [65], except yield of 328 keV γ ray

intensity ratio of the 328 and 333 keV γ rays from the present experimental data.

The time region studied was t=-40 ns to t=2.0 μs. The upper limit was set by the fact that most of the μd atoms had either decayed or reached the foil by then at the pressures and foil spacings used. The lower limit insured that the entire prompt time peak would be included. Time zero was determined by fitting the μF(2-1) and μAl(2-1) prompt time distributions with a non-linear least squares fitting program (FITA [76]), and then defining the centroid position to be t=0. These centroids differed for each of the Ge detectors, but were quite stable (to within 1 ns) over the entire range of tapes.

Once time zero was established for all four Ge detectors, the size of the time bins best suited for the data analysis was determined. Ideally, one would use as small a bin width as possible in order to obtain maximum resolution in time. However, the statistics become worse for smaller bin sizes. The optimal

bin size that could be used was determined using the ^{356}Pt photopeak from vacuum runs with the Au foil stack. If the bin sizes chosen were too narrow, the statistics were too sparse to allow the extraction of the ≈ 70 ns lifetime of this line, making background subtraction unreliable. The smallest bin width which satisfied this criterion was 40 ns. At late times the strength of the transfer signal diminishes because the number of surviving μd atoms is small. Since the effects of scattering are clearly visible at late times, it is of interest to follow the transfer signal out to later times by increasing the bin width to 80 ns after a time t_c. The initial time t_c for using the increased (80 ns) bin widths was determined by studying that data from August 1987 which had the least amount of scattering present - the 188 mbar, single gap data. It was seen that the time of 400 ns was well past the "cusp" region in the data (cf. §II.6), yet early enough to still have reasonable statistics in the bin centered at 380 ns.

IV.2.4 Checks of Data Integrity

In order to extract the time distribution of the transfer peaks, histograms created from tapes collected under identical experimental conditions were summed together. This allows one to take maximum advantage of the statistics available. However, before this was done a check of the integrity of the data had to be performed. If there was a significant electronic drift in the ADCs between tapes, then a degradation of the FWHMs of the energy peaks could occur when the histograms were added together. This would have decreased the precision with which the signal (the background subtracted area under the photopeaks) could have been determined. To insure that the magnitudes of these drifts were small enough to have a negligible effect on the area determination of the transfer peaks, the centroids of the μC(2-1) and μAl(2-1) peaks were checked for stability before any tapes were combined. As an additional check, the intensities of the μC K_α, K_β, and K_γ lines were determined for each tape. The ratios of $\mu C(K_\alpha)/\mu C(K_\beta)$ and of $\mu C(K_\alpha)/\mu$REAL were then monitored for consistency and were found to be the same (within error) for each tape at a given condition.

In addition to checks on the electronic stability, further inspections of the data were made. There were three potential problems : penetration of the Au layer to the underlying Kynar by μd atoms before transfer, transfer to impurities in the gas, and transfer of the muon to a thin surface layer of carbon [77-79].

Recall from §III.3 that the thickness of the Au layer was chosen to insure that most of the μd atoms would transfer their muons to this surface layer. In order to verify that this was indeed the case, a search for delayed μF(2-1) x rays was performed. The presence of these signals in the delayed spectra could arise (neglecting the few percent of the μd atoms diffusing to the sides of the foil stack) from μd atoms penetrating the Au surface layer of the Kynar foils. Since the transfer probability decreases as the μd energy increases [59] (§II.5), the high energy component of the initial speed distribution would have a greater probability of penetrating the Au layer. Therefore, if delayed μF(2-1) signals were observed, the time distribution extracted from the Pt γ rays would be insensitive to the high energy component of the initial speed distribution, considerably complicating the interpretation of the experiment. To test for the possible presence of such an effect, a comparison of the μF(2-1) time distribution from vacuum runs and the 188 mbar single gap condition was made. The latter condition was chosen since it possessed the least amount of scattering and therefore the least degradation of the high energy component of the initial speed distribution. After normalizing the two conditions using the prompt ($\pm$ 20 ns from t=0) μC(4-1) x rays, the two distributions were subtracted. The result was statistically consistent with zero. This check was performed with all four Ge detectors.

The presence of impurities in the gas was monitored using a

mass spectrometer. An additional check of gas purity involved searching the data for the μN(2-1) transition at 102.1 keV in the energy spectra. An approximate value of the sensitivity to nitrogen contamination was determined from the sensitivity to the nearby μC(4-1) transition (94.1 keV). It was found that a photopeak in this energy range must contain $\approx$ 100 events per 10^9 μREAL events (the typical number of μREAL events for each experimental condition) in order to be detected in this experiment. Then taking into account the solid angle subtended by all four Ge detectors ($\approx$ 5 %) gave a sensitivity of 10^{-6} μN(2-1) x rays/μREAL. Since the volume of the target was $\approx$ 1 liter, the sensitivity to nitrogen contamination was about 1 part in 10^6 at a pressure of 1 bar. In the limit of this sensitivity, there was no evidence of any nitrogen contamination under any of the conditions run in this experiment.

A final cause for concern manifested itself in the high pressure data (2.56,7.85 bar) of the May 1987 test runs. At these pressures μC K-series x rays were observed in the delayed spectra. The μC(3-1) and μC(4-1) transitions were used for analysis since interpretation of the μC(2-1) peak was made difficult by a Pt K_β electronic x ray at nearly the same energy. The lack of delayed μF x rays eliminated the possibility that these μC x rays were due to penetration of the Au layer. The distinctly different behavior of the carbon time distribution with respect to the μN(2-1) time distribution (Figure 9) argued against the carbon being in gaseous form between the foils (the

μN data are from the May 1987 run in which there was no palladium filter or mass spectrometer in the system). The apparent "steepening" of the μC time distribution as the pressure decreased (Figure 10) seemed to indicate that the carbon resided on the surface of the Au, since as the pressure was decreased, the resultant reduction in the degradation of the μd initial energy allowed more of these atoms to penetrate the carbon layer [77]. This suspicion was confirmed using x-ray photoemission spectroscopy of several foil samples [78]. It was found that there was a 5 Å layer of carbon residing on the surface of the Au with a ratio of Au:C atoms of 2:1 [78]. The presence of such a surface carbon layer on Au is well known [79]. Again, a problem arises with interpretation since the carbon surface layer will preferentially sample the low energy portion of the initial speed distribution - an effect opposite to that of penetration of the Au. Thus, it was clearly desirable to work at pressures where the μC x rays did not have a measurable effect on the time distribution. Using a method analogous to the one employed in the search for μF x rays, no evidence was found for transfer to the surface carbon layer at any of the conditions used in the August 1987 run.

IV.2.5 Production of Transfer Related Time Distributions

The extraction of the time distribution of transfer events proceeded next. The area under each relevant peak was determined using the program FITA, which employs the method of non-linear least squares. Several comments should be made on the options that were implemented in the fitting procedure. First, the FWHMs of the peaks were obtained from a fit to either prompt peaks (e.g. carbon lines) or to peaks containing both prompt and delayed times (e.g. Pt γ rays). The values of the FWHM were then treated as a fixed parameter in the fit of the area of the peaks as a function of time, a procedure which reduced the fractional error of the area determination for peaks containing few events. This occurred at late times where the signal began to fade into the noise. Background was represented by a linear function

$$B_1 = ax+b \qquad \text{(IV-1)}$$

for delayed times (for an ADC channel x) and by a "pseudo" step function of the form

$$B_2 = B_1 + \frac{(2-e^{\lambda X})}{2} \qquad X<0$$

$$B_2 = B_1 + \frac{e^{-\lambda X}}{2} \qquad X\geq 0 \qquad \text{(IV-2)}$$

for prompt signals (with X=0 defined as the centroid of the peak), where incomplete charge collection can degrade resolution and add a tail to the low energy side of the photopeak [80]. A

transfer peak was followed out to 2.0 μsec or until the signal could not be extracted reliably from the noise. This "cutoff" was defined to be the time bin in which the relative error in the area was greater than 1/3, which corresponds to a 99.73 % confidence level (3σ) that the signal represents a true spectral line and not a fluctuation in background [81]. It is worth noting that the background was not entirely random in time, i.e. there was also a transfer-related component in the background. This background was probably due to Compton events in the Ge detectors produced by higher energy (> 356 keV) transfer photons [82].

After the histograms were added together, time projections of the energy spectra were made into the following time bins : 40 ns wide bins from 0 to 400 ns, and 80 ns wide bins from 400 to 2000 ns. Then the background subtracted intensity of each aforementioned Pt γ ray was determined as a function of time using FITA for each time bin. This constituted the raw data used in the analysis.

IV.2.6 Subtraction of the Background from the Au layer

The raw data for Pt γ rays must be corrected for events which were due to prompt stops in the Au layer on the foils. These stops produce delayed Pt γ rays with a $\approx$ 70 ns lifetime and thus contaminate the early time data. The vacuum runs with single or double spaced foil stacks provided only a weak time

distribution for this background, typically fading into the noise after only 140-180 ns. Instead, the solid Au target was used to provide an accurate determination of the shape of the Pt 356 photopeak as a function of time from 0 to 480 ns. (It was not necessary to determine this for the other two γ rays since they arise from the same process of muon absorption by a gold nucleus.) Identical time bins were used for the background and the raw data. Vacuum runs with the Au foil stacks thus provided information on the strengths of the Pt 328,333 and 356 keV signals coming from the prompt stops in the Au layers on the foils. The total area under each Pt signal from the vacuum runs was then calculated as well as the area under the Pt 356 line from the solid Au runs (for identical time bands). By scaling the solid Au time distribution by the area ratio of the vacuum time distributions to the solid Au time distribution a simulated background signal was produced for each Pt γ ray. The resultant distributions, which ran from 0 to 480 ns, are those which the vacuum runs would have produced over a long period in the beam line. There are actually two such distributions for each Pt γ ray since both a single gap and double gap foil stack were used.

A monitor was needed to scale the resultant vacuum distributions to the proper strength for each experimental condition. The intensity of the μC($K\gamma$) line was suitable for this task. This line was free of any "contaminant" lines, unlike the μC(K_α) (a Pt K_β electronic x ray was at nearly the same energy) and μC(K_β) (contaminated by the μAl(4-2) transition).

The resultant vacuum distributions were then scaled by the prompt $\mu C(K_\gamma)$ intensity ratio between pressure runs and vacuum runs to produce the background time distribution for each Pt γ ray at any condition, which was then subtracted from the raw data.

The results in the time bin centered around 20 ns were statistically consistent with zero for all experimental conditions and therefore this time bin was omitted from the entire analysis.

IV.2.7 Combining Photopeaks into One Time Distribution

Once the three Pt γ-ray time distributions were corrected for contamination by the "prompt" background they were combined into a single distribution. The procedure was to fold the two weaker Pt γ rays into the stronger Pt 356 signal. Since the efficiency of the Ge detectors is a function of energy, before each signal was combined with the Pt 356 line they were normalized to have the same area for the same Δt, where Δt ran from 60 ns to the time where the signal faded into the noise. The distributions were then combined using the weighted mean

$$N_i = \sum_j \frac{w_{ij} n_{ij}}{w_{ij}} \qquad \text{(IV-3)}$$

where N_i is the number of events in bin i for the combined distribution, n_{ij} is the number of events in bin i for photopeak j, and w_{ij} is the weight given by

$$w_{ij} = \sigma_{ij}^{-2} \qquad \text{(IV-4)}$$

where σ_{ij} is the error in the number of events in bin i of photopeak j. The result of combining lines was a single time distribution for each Ge detector in which the fractional error had been reduced with respect to a single line.

Before the time distributions from the four Ge detectors were combined into a single time distribution a consistency test of the data was performed, according to the procedure described in reference [83]. It was found that no single detector showed any signs of being inconsistent with the rest of the detectors, and therefore the time distributions from the individual detectors were combined using the weighted mean to produce a final time distribution at a given condition.

IV.3 Monte Carlo Simulation

It was pointed out in §II.6 that under appropriate low pressure conditions the time distribution of the μd atoms striking the foil could be determined analytically, subject to the assumption that there was no scattering en route to the foils. However, at higher pressures the presence of scattering eliminates the possibility of deriving a functional form for f(t). In addition, with the mean free path of the diffusing atoms on the order of the foil spacing, diffusion theory was not applicable. Instead, the arrival time of the μd atoms must be calculated by a Monte Carlo simulation of the diffusion process.

It is useful to begin by stating what is sometimes called the "fundamental principle" of Monte Carlo. If p(x)dx is the probability of x lying between x and x + dx with $a \leq x \leq b$ and

$$\int_a^b p(x')dx' = 1 \qquad \text{(IV-5)}$$

then

$$r = P(x) = \int_a^x p(x')dx' \qquad \text{(IV-6)}$$

determines x uniquely as a function of the random number r. Furthermore, if r is uniformly distributed on the interval (0,1), then x occurs with frequency p(x)dx in the interval (x,x+dx) [84].

The random number generator used for analyzing the diffusion data was the "mimimal standard" suggested by Park and Miller

[85]. The generating function was of the multiplicative linear congruential type :

$$(IV\text{-}7) \qquad f(z) = az \bmod m \qquad 1 \leq z \leq m-1$$

(where a and m are constants) which will generate a (pseudo) random sequence of integers

$$(IV\text{-}8) \qquad z_{n+1} = f(z_n) \qquad n=1,2,3...$$

Equation (IV-8) was then normalized to produce a sequence of random numbers uniformly distributed on the interval $0 < r < 1$:

$$(IV\text{-}9) \qquad r_n = z_n/m$$

The sequence (IV-8) must be initiated with an initial seed z_1, the choice of which is immaterial since <u>all</u> seeds between 1 and m-1 are equally valid. The values recommended (and used) for the modulus m and the multiplier a were :

$$m = 2^{31} - 1$$
$$a = 16807$$

The Monte Carlo simulation commenced with the formation of the μd atoms in the gaseous region between the foils. The μd atom was then followed as it diffused through the gas, its history dependent upon the experimental condition that was being simulated. Eventually, the μd history would be terminated when the muon either struck a foil surface or side boundary of the foil stack. The muon is also subjected to the "inelastic" channels described in §II.4 (such as muon decay), which may occur before transfer is realized. The Monte Carlo was run until a desired number of μd atoms would strike the foil surface. A

general description of the calculation is delineated below.

(1) Initial position:

It was assumed that the μd atoms formed, uniformly distributed between two foils of radius R_f separated by a distance 2b. The probability density function (p.d.f.) for this case is then

$$p(z) = \frac{1}{2b} \qquad \text{(IV-10)}$$

and

$$r_1 = \int_{-b}^{z} p(z)dz \qquad \text{(IV-11)}$$

or

$$z = b(2r_1 - 1) \qquad \text{(IV-12)}$$

The determination of the transverse position requires choosing two additional random numbers r_2 and r_3. The p.d.f. for the radial position R is given by

$$p(R) = \frac{2\pi R}{\pi R_f^2} \qquad 0 < R < R_f \qquad \text{(IV-13)}$$

and that for the azimuthal angle φ by

$$p(\varphi) = \frac{1}{2\pi} \qquad -\pi \leq \varphi \leq \pi \qquad \text{(IV-14)}$$

Substituting (IV-13) and (IV-14) into (IV-6) yields the following equations for R and φ :

$$R = R_f\sqrt{r_2} \qquad \text{(IV-15a)}$$

$$\varphi = \pi(2r_3 - 1) \qquad \text{(IV-15b)}$$

The transverse positions are then given by

(IV-16) $$x = R\cos\varphi$$
$$y = R\sin\varphi$$

(2) Initial direction:

The initial direction of the μd atoms after formation was assumed to be isotropic. The direction cosines u,v,w are defined in the usual way (Figure 11) such that $u = \cos\alpha$, $v = \cos\beta$, and $w = \cos\gamma$ subject to the constraint that $u^2 + v^2 + w^2 = 1$. One wants to assign initial directions such that u,v,w are uniformly distributed on the unit sphere (Figure 12). Then for the direction cosine w

(IV-17) $$p(w)dw = \frac{-2\pi\sin\gamma d\gamma}{4\pi} = \frac{dw}{2}$$ and

(IV-18) $$w = 2r_4 - 1$$

Since $\rho = (u^2 + v^2)^{\frac{1}{2}} = (1 - w^2)^{\frac{1}{2}}$ and using (IV-15b) to compute ξ (with a different random number) it can be seen that

(IV-19) $$u = \rho\cos\xi$$
$$v = \rho\sin\xi$$

(3) Time to follow the μd atom:

During the time between formation and arrival at the foil, the μd atom is subjected to several inelastic processes, described in §II.4, any one of which results in the loss of the muon. Of these, only muon decay and dμd molecular ion formation were considered since the other processes are negligible at the pressures used here. In fact, dμd formation could also have been

neglected. These processes were ignored for the fitting procedure described in §IV.5. However, it was of importance to take into account the fraction of μd atoms lost to decay for each experimental condition. The p.d.f. for an exponential process such as decay is

$$p(t) = \lambda e^{-\lambda t} \qquad \text{(IV-20)}$$

Then

$$r_6 = \int_0^t p(t')dt' = 1 - e^{-\lambda t}$$

$$t = \frac{-\ln (1-r_6)}{\lambda} = \frac{-\ln r_6}{\lambda} \qquad \text{(IV-21)}$$

The last step is valid since r_6 is uniformly distributed on the interval (0,1). In fact, if more than one "inelastic" process of the form (IV-20) exists, a time t_i can be computed with (IV-21) for each of the i processes. The shortest sampled time t_s then represents how long the muon will survive before it is lost to process s.

(4) The initial speed is determined:

The initial speed distribution of the μd atoms after formation must be assumed <u>a priori</u>. For simplicity, three distributions were initially considered. A delta function

$$f_1 = \delta(v - v_0) \qquad \text{(IV-22)}$$

is a one parameter distribution that is conceptually simple to understand. A Maxwell speed distribution

$$(IV\text{-}23) \qquad f_2 = 4\pi(m/2\pi KT)^{3/2}\, v^2 e^{-mv^2/2KT}$$

is a one parameter distribution with a spread in initial speeds. The speeds were chosen using a Monte Carlo rejection method since the expression

$$(IV\text{-}24) \qquad r = \int_0^v f_2(v')dv'$$

cannot be inverted in analytic form to provide $v = f(r)$. A Gaussian speed distribution with mean $\bar{v}$ and standard deviation σ

$$(IV\text{-}25) \qquad f_3(v) = (1/\sigma\sqrt{2\pi})\, \exp[\, -\tfrac{1}{2}\{(v-\bar{v})/\sigma\}^2]$$

is a simple example of a two parameter distribution. The Gaussian speed may be determined directly from

$$(IV\text{-}26) \qquad v = \bar{v} + r_n\sigma$$

where r_n is randomly chosen from a gaussian distribution of zero mean and unit variance. The distributions (IV-22) and (IV-23) have the added benefit that, in the limit of zero scattering <u>en route</u> to the foils, the time distribution of the μd atoms reaching the foil can be determined analytically (§II.6). The μd monte carlo can then be tested, <u>in the absence of scattering</u>, by generating a time distribution with a given initial speed distribution. These "data" can then be fit to the analytic form of f(t) (see Appendix B) allowing the extraction of the correct parameter value in the process, namely the mean energy (3KT/2) of the Maxwell distribution or the speed v_0 of the delta function.

(5) Determine the initial hyperfine state:

Elastic scattering cross-sections depend on the hyperfine state F of the incident μd atom. The possible hyperfine states for the μd atom are F=1/2,3/2. Initially, the μd atoms are formed in a statistical mixture ($\propto$ 2F+1), i.e. 2/3 will reside in the quartet (F=3/2) and 1/3 in the doublet (F=1/2).

(6) Generate a scattering event:

The scattering is assumed to be isotropic in the center of mass (CM), i.e. only S-wave scattering is considered. The justification for this assumption is in the theoretical scattering cross sections used in the analysis [12]. In deuterium, the elastic scattering cross sections (no change in the hyperfine state of the μd atom after collision) for P-wave and higher l-states are at least one order of magnitude smaller than the corresponding S-wave cross sections for the CM energies (ϵ) of interest here ($\epsilon \leq$ few eV). The P-wave contribution does start to seriously affect the transition cross section (a change in F due to the collision) for CM energies above $\approx$ 0.5 eV. However, this cross section is still an order of magnitude smaller than the elastic cross section. Also, the theoretical elastic cross sections for scattering in the upper (F=3/2) and lower (F=1/2) hyperfine state are very similar in magnitude.

The total energy in the CM during the collision must be determined in order to calculate the total cross section $\sigma(\epsilon)$. A collision is "forced" to take place between a μd atom with a

projectile speed v_p chosen as described in step (4) and a target D_2 molecule moving with a speed v_t chosen from a Maxwell distribution at room temperature. As a convention, lowercase(uppercase) variables will correspond to LAB(CM) quantities, with prime quantities referring to values after the collision. Assume that the collision takes place in the yz-plane with the incident projectile velocity along the z-axis (Figure 13). Here v_c is the velocity of the CM as measured in the LAB frame, and v_r is the relative velocity

$$v_r \equiv v_p - v_t \qquad \text{(IV-27)}$$

The angle α must be chosen such that

$$-1 \leq \cos\alpha \leq 1 \qquad \text{(IV-28)}$$

The projectile velocity in the LAB frame after collision is given by

$$v_p' = V_p' + v_c \qquad \text{(IV-29)}$$

The projectile velocity in the CM can be calculated from the definition of the velocity of the CM

$$v_c = \frac{m_p v_p + m_t v_t}{m_p + m_t} \qquad \text{(IV-30)}$$

where $m_p(m_t)$ is the projectile(target) mass. Defining $m \equiv m_p+m_t$ and substituting (IV-27) and (IV-30) into (IV-29) yields

$$V_p = (m_t/m)\, v_r \qquad \text{or} \qquad \text{(IV-31)}$$

$$V_p = (m_t/m)\,[v_p^2 + v_t^2 - 2v_p v_t \cos\alpha]^{\frac{1}{2}} \qquad \text{(IV-32)}$$

The total energy ϵ available in the CM can be calculated

using (IV-32) since

$$(IV\text{-}33) \qquad \epsilon = \tfrac{1}{2}[m_p v_p^2 + m_t v_t^2] = \left[\frac{m_p m_t + m_p^2}{2m_t}\right] v_p^2$$

(7) Calculate the total cross section:

Once the collision energy in the CM is determined the total cross section $\sigma(\epsilon)$ can be calculated. For μd atoms initially in the lower hyperfine state, a transition between hyperfine states can only occur if $\epsilon \geq \Delta E_{hfs}$ since the phase space for the transition tends to zero as ϵ approaches the hyperfine splitting (.0485 eV for μd). The total cross section as a function of the initial hyperfine state (hfs) is summarized in Table VIII, where the 1(2) represents the lower(upper) hfs.

Table VIII
Total Scattering Cross Section

Initial hfs	CM Energy	Total Cross Section
1	$\epsilon < \Delta E_{hfs}$	σ_{11}
1	$\epsilon \geq \Delta E_{hfs}$	$\sigma_{11} + \sigma_{12}$
2	all ϵ	$\sigma_{22} + \sigma_{21}$

The values for the energy dependent cross sections σ_{11},σ_{22}, and σ_{21} are those of Bubak and Faifman [12]. The transition cross section σ_{12} was calculated using the principle of detailed balancing [86] :

$$\text{(IV-34)} \qquad \sigma_{12}(\epsilon) = \left[\frac{2S_2+1}{2S_1+1}\right]\left[\frac{p_2}{p_1}\right]^2 \cdot \sigma_{21}(\epsilon)$$

where $S_1(S_2)$ is the spin and $p_1(p_2)$ is the momentum in the lower(upper) hfs state. The cross sections used from reference [12] are nuclear cross sections. In order to simulate scattering from D_2 molecules, the nuclear cross sections were multiplied by an energy independent constant. Although this is not expected to be entirely accurate, we are not aware of any calculation for this scaling factor as a function of energy for μd scattering from D_2 (except for [51,53] which only consider collision energies up to 0.25 eV).

(8) Calculate path length to collision:

The p.d.f. for a collision to occur between the distance l and l+dl in a medium of number density N and total scattering cross section σ is given by

$$\text{(IV-35)} \qquad p(l)dl = N\sigma e^{-N\sigma l}dl$$

In an analogous manner with step (3), it can be shown that the path length to the collision with a target D_2 molecule is

$$\text{(IV-36)} \qquad l = -\lambda \ln r$$

where the mean free path $\lambda(\epsilon) = 1/N\sigma(\epsilon)$.

(9) Determine the point of collision:

After a path length is chosen from (IV-36), the geometry of the target dictates the following three possibilities:

(a) The μd strikes a foil surface within a path length l:

The time required to traverse the distance to the foil along the direction u,v,w is calculated and added to the time the μd has already been in existence. (If inelastic processes are being considered, then a check is made to see if the μd atom is lost before it strikes the foil .) This foil hit time t_f would be the observed time if it was assumed that the Ge detectors had perfect resolution and a promptly emitted signal (such as a muonic x ray) was used for the transfer signal. Of course, neither assumption is valid. However, the effects of the capture process in Au and the detector resolution can be calculated and then added to t_f.

The detector "response" function is then comprised of two parts, the p.d.f. representing the capture process in Au

$$f(t,\lambda) = \lambda e^{-\lambda t} \qquad 0 \le t \le \infty \tag{IV-37}$$

and the detector resolution function

$$r(t',t) = (1/\sigma\sqrt{2\pi}\,)\exp[-\tfrac{1}{2}((t'-t)/\sigma)^2] \tag{IV-38}$$

The p.d.f. for the actual measured time t' is then [83]

$$f'(t') = \int f(t,\lambda)r(t',t)dt \tag{IV-39}$$

Evaluating (IV-39) yields the "response" time of detecting a transfer signal

$$(IV\text{-}40) \qquad f'(t') = e^{(\lambda\sigma)^2/2} \cdot e^{-\lambda t'} \cdot G[(t'/\sigma) - \lambda\sigma]$$

where G is a tabulated function known as the cumulative normal standard distribution. Therefore, once the rate λ for μ-absorption in Au and the standard deviation of the detector resolution σ (near 350 keV) have been determined, the "response" time can be sampled from the p.d.f. (IV-40) to obtain the measured time $t_{obs} = t_f + t'$. The life history of the μd atom is then terminated and a new event is generated.

The experimental time distribution of the Pt 356 photopeak from the solid Au target was used to determine λ and σ. These distributions (one for each detector) were fit (using MINUIT [87]) to the form (IV-40) with λ and σ treated as free parameters. The results can be seen in Table IX (reduced chisquare $\chi^2_\nu \equiv \chi^2/\nu$ where ν is the number of degrees of freedom in the fit and ν = number of data points - number of free parameters in the fit). The data from Detector C were somewhat anomalous; therefore Detector C was omitted from the calculation of the weighted mean, although its inclusion had only a 1 % effect on the values which were used in the analysis :

$$\lambda^{-1} = 70.40 \pm 0.22 \quad \text{ns}$$

$$\sigma = 4.84 \pm 0.09 \quad \text{ns}$$

The λ^{-1} value quoted above is in disagreement with the value quoted in the literature (the weighted mean is 72.77 ± 0.47 ns [88]), but is close to the values obtained by another method in this experiment [89].

Table IX
Values of λ, σ used in Determining Detector Resolution

Detector	λ (ns^{-1})	σ (ns)	χ^2_ν
A	0.01410 ± 0.00007	4.86 ± 0.16	0.99
B	0.01441 ± 0.00008	5.18 ± 0.16	1.13
C	0.01376 ± 0.00009	4.24 ± 0.22	6.03
GMX	0.01414 ± 0.00007	4.56 ± 0.14	0.88

(b) The μd strikes a Kynar boundary:

If the radial position of the μd atom became larger than a foil radius within a path length l it was assumed to be captured in the cylindrical "side" wall of the target. The muon is then transferred to the Kynar and is considered lost for our purposes. Approximately 3-6 % of the μd atoms were lost to this channel depending upon the foil spacing and pressure used.

(c) The μd remains in the gap between foils:

After checking to see if the μd atom has not been lost to an inelastic channel, a collision occurs with the D_2 molecule from step (6). Assured that the μd atom will still "survive" after travelling a distance l, both the speed of the μd atom and its direction after collision must be calculated.

In order to begin the calculation of the μd speed after its collision with the D_2 molecule, we must choose the CM scattering angles θ, Φ such that

$$\begin{aligned} -1 \leq \cos\theta \leq 1 \\ -\pi \leq \Phi \leq \pi \end{aligned} \qquad \text{(IV-41)}$$

as well as use the angle between the projectile and target velocities α chosen in (IV-28). The speed of the μd atom after collision follows directly from equation (IV-29) :

$$(IV\text{-}42) \qquad v_p' = [\, V_p^2 + v_c^2 + 2V_p' \cdot v_c \,]^{\frac{1}{2}}$$

since v_c is unchanged by the collision and $V_p'=V_p$ in an elastic collision. The speed V_p can be calculated from equation (IV-32). The velocity of the center of mass can be calculated from

$$(IV\text{-}43) \qquad v_c = v_c \sin\beta \hat{y} + v_c \cos\beta \hat{z}$$

with

$$(IV\text{-}44a) \qquad v_c \cos\beta = \frac{v_p \cdot v_c}{v_p} = (m_p/m) v_p + (m_t/m) v_t \cos\alpha$$

$$(IV\text{-}44b) \qquad v_c \sin\beta = v_c (1 - \cos^2\beta)^{\frac{1}{2}} = (m_t/m) v_t \sin\alpha = V_p \sin\delta$$

The last step follows from (IV-45) which is one of two useful expressions which can be extracted from Figure 13 :

$$(IV\text{-}45) \qquad v_r \sin\delta = v_t \sin\alpha$$

$$(IV\text{-}46) \qquad \tan\delta = \frac{v_t \sin\alpha}{v_p - v_t \cos\alpha} \qquad 0 \le \delta \le \pi$$

The final term in equation (IV-42) involves the CM velocity of the projectile after scattering through angles θ, Φ in the CM :

$$(IV\text{-}47) \qquad V_p' = V_p [\, \sin\theta\cos\Phi \hat{X} + \sin\theta\sin\Phi \hat{Y} + \cos\theta \hat{Z} \,]$$

Since the scattering takes place in the YZ plane, a passive rotation about the x-axis is required to express V_p' in terms of the LAB basis :

$$V_p' = V_p \begin{bmatrix} 1 & 0 & 0 \\ 0 & \cos\delta & -\sin\delta \\ 0 & \sin\delta & \cos\delta \end{bmatrix} \begin{bmatrix} \sin\theta\cos\Phi \\ \sin\theta\sin\Phi \\ \cos\theta \end{bmatrix}$$

$$(IV\text{-}48)\qquad \vec{V}_p' = V_p[\ \sin\theta\cos\Phi\hat{x} + (\sin\theta\sin\Phi\cos\delta - \cos\theta\sin\delta)\hat{y} + (\sin\theta\sin\Phi\sin\delta + \cos\theta\cos\delta)\hat{z}\ ]$$

Now using (IV-32),(IV-44),(IV-46), and (IV-48), equation (IV-42) can be solved for the projectile (μd) speed in the LAB after collision.

The direction of the μd atom after collision must be expressed in terms of a <u>fixed</u> basis, i.e. the U,V,W system of Figure 12, where W = ±1 is taken to be perpendicular to the foils. It is desirable to form a rotation which takes the space U,V,W into itself, i.e. take the point $(u_s,v_s,w_s) = (0,0,1)$ into the initial direction (u,v,w) [84]. The rotation matrix is formed by taking an active rotation about the V-axis through an angle γ

$$(IV\text{-}49)\qquad \begin{bmatrix} u' \\ v' \\ w' \end{bmatrix} = \begin{bmatrix} \cos\gamma & 0 & \sin\gamma \\ 0 & 1 & 0 \\ -\sin\gamma & 0 & \cos\gamma \end{bmatrix} \begin{bmatrix} u_s \\ v_s \\ w_s \end{bmatrix}$$

followed by an active rotation about the W-axis through an angle ξ

$$(IV\text{-}50)\qquad \begin{bmatrix} u'' \\ v'' \\ w'' \end{bmatrix} = \begin{bmatrix} \cos\xi & -\sin\xi & 0 \\ \sin\xi & \cos\xi & 0 \\ 0 & 0 & 1 \end{bmatrix} \begin{bmatrix} u' \\ v' \\ w' \end{bmatrix}$$

which yields

$$(IV\text{-}51)\qquad \begin{bmatrix} u'' \\ v'' \\ w'' \end{bmatrix} = \begin{bmatrix} \cos\gamma\cos\xi & -\sin\xi & \sin\gamma\cos\xi \\ \cos\gamma\sin\xi & \cos\xi & \sin\gamma\sin\xi \\ -\sin\gamma & 0 & \cos\gamma \end{bmatrix} \begin{bmatrix} u_s \\ v_s \\ w_s \end{bmatrix}$$

Using the relations from Figure 12

$$(IV\text{-}52)\qquad \begin{aligned} \rho &= \sin\gamma = (1-w^2)^{\frac{1}{2}} \\ \cos\xi &= u/\rho \\ \sin\xi &= v/\rho \end{aligned}$$

in (IV-51) produces

$$(IV\text{-}53) \qquad \begin{bmatrix} u'' \\ v'' \\ w'' \end{bmatrix} = \begin{bmatrix} uw/\rho & -v/\rho & u \\ vw/\rho & u/\rho & v \\ -\rho & 0 & w \end{bmatrix} \begin{bmatrix} u_s \\ v_s \\ w_s \end{bmatrix}$$

The μd atom is scattered through the LAB angles ϑ,φ with respect to the incident line of flight u,v,w

$$(IV\text{-}54) \qquad (u_s,v_s,w_s) = (\sin\vartheta\cos\varphi,\sin\vartheta\sin\varphi,\cos\vartheta)$$

Note that if the μd atom is not scattered (ϑ=0,φ=0) then rotation (IV-53) insures that the final direction (u",v",w") is equal to the initial direction (u,v,w). Therefore, the final direction cosines (u',v',w') expressed in terms of the initial direction cosines (u,v,w) and the LAB scattering angles ϑ,φ are

$$(IV\text{-}55) \qquad \begin{aligned} u' &= [\sin\vartheta\cos\varphi uw - \sin\vartheta\sin\varphi v]/\sqrt{1-w^2} + u\cos\vartheta \\ v' &= [\sin\vartheta\cos\varphi vw + \sin\vartheta\sin\varphi u]/\sqrt{1-w^2} + v\cos\vartheta \\ w' &= -\sin\vartheta\cos\varphi\sqrt{1-w^2} + w\cos\vartheta \end{aligned}$$

The last step is the calculation of the polar angle ϑ and the azimuthal angle φ (defined in the positive sense from the x-axis). The final projectile velocity in the LAB can be expressed as

$$(IV\text{-}56) \qquad \mathbf{v}_p' = v_p'[\sin\vartheta\cos\varphi\hat{x} + \sin\vartheta\sin\varphi\hat{y} + \cos\vartheta\hat{z}]$$

Substituting (IV-44),(IV-48), and (IV-56) into (IV-29) yields

$$(IV\text{-}57) \qquad \begin{aligned} v_p'\sin\vartheta\cos\varphi &= V_p\sin\theta\cos\Phi \\ v_p'\sin\vartheta\sin\varphi &= V_p[\cos\delta\sin\theta\sin\Phi - \sin\delta\cos\theta] + V_p\sin\delta \\ v_p'\cos\vartheta &= V_p[\sin\delta\sin\theta\sin\Phi + \cos\delta\cos\theta] + v_c\cos\beta \end{aligned}$$

The LAB angles are then given by

$$\text{(IV-58)} \qquad \tan|\varphi| = \frac{\cos\delta\sin\theta\sin|\Phi| + \sin\delta(1-\cos\theta)}{\sin\theta\cos\Phi}$$

with $0 \le |\varphi|, |\Phi| \le \pi$ and $\Phi < 0 \Rightarrow \varphi < 0$ and $\Phi > 0 \Rightarrow \varphi > 0$, and

$$\text{(IV-59)} \qquad \tan\vartheta\cos\varphi = \frac{V_p\sin\theta\cos\Phi}{V_p[\sin\delta\sin\theta\sin\Phi + \cos\delta\cos\theta] + V_c\cos\beta}$$

with $0 \le \vartheta \le \pi$.

(10) Calculate the hyperfine state after collision:

If the μd atom is in the lower hyperfine state and the collision energy $\epsilon \le \Delta E_{hfs}$, then no transition is possible and the μd atom remains in the lower hyperfine state. All other cases require computing the probability of residing in, say, the upper hyperfine state

$$\text{(IV-60)} \qquad F_{prob} = \frac{\sigma_{tr}}{\sigma_{tot}}$$

where σ_{tot} is the total scattering cross section (Table VIII) and σ_{tr} is either $\sigma_{22}(\sigma_{12})$ for μd atoms initially in the upper(lower) hyperfine state. The hfs after collision can then be determined by whether a selected random number is greater or less than F_{prob}.

IV.4 Experimental Data

Prior to presenting the experimental data it is convenient to define some nomenclature for the experimental conditions as shown in Table X. The first letter D indicates the gas filling used in the target. The number indicates the gas pressure in millibar, and the final letter indicates which foil stack was used, S for single gap and D for double gap.

Table X
Nomenclature for the Experimental Conditions

Condition	Foil Spacing (cm)	Pressure (bar)
D94S	0.23	0.094
D188S	0.23	0.188
D375S	0.23	0.375
D750S	0.23	0.750
D1520S	0.23	1.520
D188D	0.46	0.188
D375D	0.46	0.375
D750D	0.46	0.750

The final analyzed time distributions of μd atoms hitting the foil surface are shown in Table XI. The data for the D94S condition have significantly less statistical weight than those for the other conditions, due to less time spent collecting data at this condition. Therefore, it was omitted from most of the analysis (see §IV.6) and in the following discussion "all" experimental conditions really means "all but D94S." However, the

D94S data served an important function in that it demonstrated the feasibility of observing delayed diffusion related photons at this low pressure. Recording experimental data at such low pressures is essential for studying the diffusion process in hydrogen gas, since the theoretical scattering probability for μp atoms in hydrogen gas is expected to be larger than for μd atoms in deuterium gas [12]. As discussed in §IV.2.6, the 20 ns bin was omitted from the analysis for all of the conditions. In addition, the 60 ns bin in the D188D data was also omitted due to background subtraction problems.

In each data column of Table XI corresponding to one experimental condition (e.g. D94S,D188S,etc.), the entry $N(t_i)$ at time t_i is the number of transfer events observed between $t_i \pm 20$ ns (40 ns) depending on whether t_i is less (greater) than 400 ns. That is, the time bin width changes from 40 ns to 80 ns at 400 ns. The normalization of the data $N(t_i)$ under any one condition is arbitrary. It is important to note that no correction for muon decay has been made to the data in Table XI (cf. §IV.5).

Table XI
Experimental Time Distributions $N(t_i)$ vs. Time

Time (ns)	D94S	D188S	D375S
20	———	———	———
60	83.3 ± 41.7	279.0 ± 36.6	479.6 ± 29.6
100	348.4 ± 29.7	525.6 ± 26.4	696.7 ± 22.6
140	431.4 ± 23.3	623.9 ± 21.0	739.0 ± 18.3
180	427.5 ± 19.9	616.5 ± 17.9	694.0 ± 15.8
220	393.0 ± 17.8	546.0 ± 15.9	629.9 ± 14.4
260	353.3 ± 16.3	462.4 ± 13.7	541.2 ± 12.8
300	306.9 ± 14.8	412.5 ± 12.7	442.9 ± 11.4
340	235.1 ± 12.1	354.6 ± 11.6	385.6 ± 10.9
380	210.0 ± 11.8	288.2 ± 10.6	331.8 ± 10.1
440	366.7 ± 17.1	455.1 ± 14.1	501.2 ± 13.2
520	264.2 ± 14.2	321.0 ± 12.7	375.5 ± 11.1
600	199.7 ± 14.1	248.9 ± 11.5	303.7 ± 10.5
680	154.7 ± 14.2	201.7 ± 10.8	224.1 ± 9.1
760	125.1 ± 13.3	170.5 ± 10.0	186.5 ± 8.9
840	88.0 ± 12.0	136.4 ± 9.9	150.7 ± 8.0
920	64.9 ± 12.1	98.7 ± 9.7	126.6 ± 8.3
1000	———	98.8 ± 11.4	97.6 ± 8.1
1080	———	75.4 ± 10.2	95.5 ± 7.9
1160	———	66.9 ± 12.2	84.5 ± 7.6
1240	———	69.9 ± 11.3	59.2 ± 7.1
1320	———	51.0 ± 15.0	64.2 ± 6.9
1400	———	———	64.7 ± 8.1
1480	———	———	57.3 ± 10.4
1560	———	———	58.7 ± 10.0
1640	———	———	———
1720	———	———	———
1800	———	———	———
1880	———	———	———
1960	———	———	———

(see p. 97 for explanation)

Table XI
Experimental Time Distributions $N(t_i)$ vs. Time

Time (ns)	D750S	D1520S
20	———	———
60	683.3 ± 27.3	837.5 ± 23.7
100	903.8 ± 22.5	934.8 ± 20.7
140	893.9 ± 19.7	899.7 ± 18.9
180	786.6 ± 17.7	785.9 ± 16.7
220	686.3 ± 16.4	666.5 ± 14.9
260	623.2 ± 14.9	581.5 ± 13.4
300	509.8 ± 13.6	472.7 ± 12.5
340	437.7 ± 12.4	406.3 ± 11.7
380	400.8 ± 11.8	347.5 ± 10.6
440	568.7 ± 14.5	571.4 ± 14.0
520	464.5 ± 13.1	435.3 ± 12.8
600	367.4 ± 12.3	359.6 ± 11.7
680	295.5 ± 11.1	319.7 ± 10.9
760	232.5 ± 10.4	250.9 ± 10.0
840	184.5 ± 9.2	232.8 ± 9.4
920	170.6 ± 9.5	185.3 ± 8.9
1000	143.3 ± 9.4	200.8 ± 9.0
1080	137.2 ± 9.0	160.0 ± 9.0
1160	121.3 ± 9.0	160.6 ± 9.2
1240	119.5 ± 8.9	146.9 ± 8.5
1320	85.1 ± 8.4	123.1 ± 8.2
1400	75.4 ± 8.4	95.0 ± 8.2
1480	63.1 ± 8.4	108.3 ± 8.1
1560	67.8 ± 8.4	94.6 ± 7.4
1640	61.7 ± 7.8	94.6 ± 7.7
1720	59.7 ± 8.1	86.4 ± 7.4
1800	59.5 ± 7.5	98.0 ± 7.5
1880	51.3 ± 8.5	80.2 ± 6.9
1960	50.0 ± 12.0	75.7 ± 7.1

(see p. 97 for explanation)

Table XI
Experimental Time Distributions $N(t_i)$ vs. Time

Time (ns)	D188D	D375D	D750D
20	———	———	———
60	———	291.2 ± 33.0	356.4 ± 23.0
100	220.7 ± 27.8	532.6 ± 24.4	474.1 ± 17.3
140	357.3 ± 20.8	610.4 ± 20.4	480.0 ± 15.0
180	393.4 ± 16.8	631.1 ± 18.1	464.9 ± 13.8
220	388.4 ± 15.0	578.6 ± 16.2	433.5 ± 12.5
260	379.6 ± 14.7	557.5 ± 15.6	383.7 ± 11.9
300	323.2 ± 12.5	461.0 ± 14.1	342.3 ± 11.0
340	312.1 ± 12.2	431.5 ± 14.1	291.6 ± 10.7
380	279.0 ± 11.8	378.3 ± 13.0	286.1 ± 10.0
440	453.0 ± 15.6	669.7 ± 17.9	433.9 ± 12.9
520	354.2 ± 13.8	561.3 ± 16.1	356.7 ± 11.7
600	294.7 ± 13.1	423.1 ± 14.5	293.4 ± 11.0
680	265.1 ± 12.6	375.2 ± 13.4	233.1 ± 9.9
760	228.5 ± 11.9	328.2 ± 12.8	214.0 ± 9.6
840	188.0 ± 12.1	285.8 ± 12.2	177.0 ± 9.0
920	137.1 ± 10.9	252.9 ± 11.4	152.2 ± 8.7
1000	123.9 ± 11.1	183.9 ± 10.9	142.6 ± 8.4
1080	87.3 ± 10.1	163.8 ± 11.3	125.6 ± 9.1
1160	86.7 ± 9.7	161.0 ± 10.9	113.9 ± 8.6
1240	77.4 ± 9.2	127.6 ± 10.4	101.8 ± 9.1
1320	88.1 ± 10.4	121.5 ± 10.3	82.8 ± 8.0
1400	66.1 ± 10.1	113.2 ± 10.1	92.8 ± 8.0
1480	72.5 ± 12.6	112.0 ± 9.6	72.5 ± 6.8
1560	67.8 ± 11.4	103.0 ± 9.6	63.7 ± 7.0
1640	56.0 ± 13.0	78.3 ± 8.9	61.9 ± 6.7
1720	50.0 ± 13.0	76.6 ± 9.8	57.7 ± 6.7
1800	42.0 ± 13.0	68.6 ± 9.7	56.8 ± 6.4
1880	———	48.2 ± 10.7	54.0 ± 6.0
1960	———	56.0 ± 16.0	52.1 ± 6.2

(see p. 97 for explanation)

IV.5 Data Analysis

For an assumed initial velocity distribution function f(v) for the μd atoms it is possible to predict the observed time distribution of those atoms striking the foil in the absence of scattering. In this low pressure (no scattering) limit one can compute the moments of the observed time distribution and then compare them to the moments of a time distribution which is calculated with an assumed velocity distribution [90]. Another approach, which involves computing second derivatives with respect to t^{-2} of the observed time distribution has been suggested [91]. In practice, the limited statistical accuracy of the experimental data may limit the applicability of these methods. For example, it may not be possible to compute more than the first two or three moments with any confidence.

In any event, it is apparent from the data that there is still some scattering present even at the minimum scattering condition used in the analysis (D188S) and thus the aforementioned methods are inapplicable. The fact that scattering is still present at this condition is best seen by studying the shape of the time distribution as a function of pressure. Upon close inspection, some subtle differences can be seen between the D188S and the D375S time distributions which indicate that there is some scattering present in this pressure region. Computer simulations (§IV.3) also indicate that at the D188S condition $\approx$ 55 % of the μd atoms reach the foils without scattering, but $\approx$

25 % scatter once, and ≈ 10 % scatter twice before reaching the foils (these values assume a Maxwell initial speed distribution with a mean energy (3KT/2) of 2.0 eV and the nuclear cross-sections of Bubak and Faifman [12] multiplied by a constant factor of 2.5 - values which are near the fitted energy and molecular factor (see §IV.6)).

When scattering is present and the mean free path of the μd atoms is comparable to the foil spacing (as in this experiment) diffusion theory is inapplicable and one can resort to a Monte Carlo (MC) simulation of the diffusion process in order to analyze the data. In all MC simulations used for analysis, the form of the initial (isotropic) velocity distribution of the μd atoms was assigned and usually characterized by one or two free parameters. All MC simulations used in the analysis also assumed the energy dependence for the nuclear scattering cross sections (σ's) provided by Bubak and Faifman [12]. These were multiplied by an energy independent factor (the "molecular factor") to obtain the molecular cross sections. The molecular factor was treated as a free parameter in the fit. The μd atoms were assumed to be formed uniformly between the foils.

In order to constrain the fitting procedure and make optimal use of the available data, all experimental conditions were analyzed simultaneously. A scale parameter was assigned to each condition which served to scale the MC generated time distribution for that condition (which MC typically contained 40k events (foil hits)), to the corresponding experimental time

distribution which typically contained ≈ 10k events. The analysis then employed the program MINUIT to find the best parameter values which minimized χ^2.

The Monte Carlo iteration procedure and the production of grids of Monte Carlos in parameter space, which are discussed below, were run on the Cray X-MP/48 at the National Center for Supercomputing Applications in Champaign,Illinois. The fits to the experimental data using the interpolation method (see below) were run on a VAX-11/750 at William and Mary.

The initial attempt at fitting the experimental data involved running high statistics Monte Carlo simulations of the experimental conditions in an iterative manner. The procedure was straightforward. An initial speed distribution was assigned (e.g. a Maxwell distribution) which could be characterized by one or two free parameters (e.g. the mean energy 3KT/2). Initial guesses of the parameter values were provided for the program MINUIT , e.g., the mean energy, the molecular factor, and the seven scale factors (which, of course, have nothing to do with generating Monte Carlos) and then Monte Carlo time distributions were generated for all experimental conditions. These distributions were then reduced by the scale factors to produce the "theoretical" data for the initial parameter values. The value of χ^2 was computed and then a new set of Monte Carlo time distributions was generated using the new parameter values chosen by the minimization procedure in MINUIT. This iterative procedure continued until the parameter values which minimized χ^2

were found.

Each iteration of the Monte Carlo for each experimental condition used the same set of initial random number seeds. With the appropriate choice of the multiplier in equation (IV-7) a number of initial seeds can be determined separated by more than eight million "steps" in the random number sequence [92]. This has the effect of producing "streams" of random numbers which can be assigned to a particular process. For example, in the Monte Carlo used here, nine different streams of random numbers were assigned to determine : the initial speed, the initial position, the initial direction, the initial hyperfine state, and the hyperfine state after collision of the μd atoms, the speed of the D_2 molecules in the gas, the path length to collision, the time sampled from the detector response function, and the relevant scattering angles in the kinematics. The advantage of these fixed random number streams is that changes in the time distribution are due to either changes in the experimental conditions or changes in the parameter values, and not to random fluctuations caused by using a different random number sequence. For example, it is desirable to simulate 40k μd atoms which start from exactly the same positions between the foils regardless of the gas pressure or their initial energy.

The results of this iterative procedure were initially puzzling in that the parameter errors quoted by MINUIT were excessively small, e.g. 2-4 orders of magnitude smaller than what was expected (also see Table XII). Apparently there is an

inherent flaw in generating the theoretical distribution in a χ^2 minimization procedure by a Monte Carlo (stochastic) process. As χ^2 approaches its minimum value very small steps in parameter space are taken by MINUIT (e.g. 1 meV or less in energy). If the theoretical distribution is represented by an analytic function (or can be computed numerically) such small changes in parameter values will result in continuous changes in the theoretical distribution. However, in a Monte Carlo generated time distribution the number of events in a given time bin cannot change by arbitrarily small amounts in a continuous fashion, but can only change by discrete amounts (which can be non-integer due to the scale factor). This can cause problems in the computation of second derivatives in the parameter space and thus produce unreliable parameter errors, since the second derivative matrix is inverted to produce the error or covariance matrix.

The problem of extremely small parameter errors was solved by generating a grid of points in the parameter space (first pointed out to us by S. Park and K. Miller and also by R. Carlini). Each point in the grid represented seven time distributions generated with Monte Carlos which used the parameter values associated with that grid point. The theoretical time distributions could then be determined for any parameter values by interpolation between the grid points using a cubic spline interpolation method, which produced an interpolated function that was continuous through the second derivative [93]. In general, the fits to the data involved two or three free

parameters (excluding scale factors) and hence two or three-dimensional interpolation. Thus, in this interpolation method the grid of Monte Carlo time distributions was generated first and then the χ^2 minimization program was run, with the time distributions for new parameter values supplied by MINUIT interpolated from the existing grid. If one or more of the new parameter values supplied by MINUIT was outside of the tabulated grid in parameter space then it was necessary to run a new set of Monte Carlos with those parameter values. For a suitably chosen range of parameter values in the grid, this would only be necessary during the early stage of the fitting procedure (when the steps in parameter space are relatively large) and thus has no effect on the final parameter error analysis.

The effect of the method used to generate the theoretical distribution for use in MINUIT on the parameter errors is shown by the results of a test (Table XII). The theoretical distributions used in this table are simply Maxwell or Gaussian speed distributions which were generated (for each iteration in MINUIT) via analytic expressions (equns. (IV-23) and (IV-25)), a Monte Carlo (MC) iteration procedure as described above, or by the cubic spline interpolation method from an existing grid in parameter space. The experimental distributions to which each of these was fitted were produced by a Monte Carlo method (§IV.3) , where the mean energy of the Maxwell distribution was 1.00 eV and the Gaussian parameters were a mean of 100.0 eV and standard deviation of 10.0 eV. In all cases the reduced χ^2 of the fits

Table XII
Effect of Method used for Theory Generation on Parameter Errors

Distribution	Method	Mean Energy (eV)	Sigma (eV)
Maxwellian	MC iteration	1.002 ± 0.0003	———
	analytic	1.002 ± 0.008	———
	interpolation	1.001 ± 0.008	———
Gaussian	MC iteration	100.0 ± 0.001	10.00 ± 0.0008
	analytic	100.0 ± 0.1	10.02 ± 0.07
	interpolation	100.0 ± 0.1	10.00 ± 0.06

were less than one. Note that the Monte Carlo iteration method produces the correct parameter values with errors that are much too small. Therefore, all fits to the experimental data described below employed the interpolation method from a set of grid points in parameter space.

By running a preliminary set of Monte Carlos with an assumed Maxwell distribution of varying mean energies it was apparent that the mean energy of the μd atoms was in the neighborhood of 1.5-2.0 eV and that the molecular factor was about 2-2.5. These rough estimates were simply made by visually comparing the Monte Carlo generated time distributions to the experimental time distributions for all experimental conditions. Such an estimate is useful to confine the extent of the interpolation grid to a reasonable region in parameter space. If the grid size is too

small then there will be too many Monte Carlo iterations outside the grid and the parameter errors will become excessively small, while a grid larger than necessary would be costly in terms of computation time.

The effect that the number of points in the grid had on the fit was examined by producing a grid of Monte Carlos for a Maxwellian speed distribution. Then, in the two-parameter space (mean energy x molecular factor) a grid with 11x8 points was produced, from which smaller grids of 6x4 and 4x4 were taken. Increasing the number of points in these grids did not increase the accuracy of the interpolation [93]. This was confirmed when fits using various grid sizes yielded identical values (within the quoted error) for the mean energy of the μd atoms and the molecular factor. Thus, for two-dimensional interpolations a grid size of 4x4 was used and for the three-dimensional case a 4x4x4 grid was employed. Minimizing the number of points in the grid is essential since even for a two-dimensional grid it was necessary to run 4x4x7 = 112 Monte Carlos with 40k events (see below) in each Monte Carlo in the grid. Adding additional parameters to the fit was done with care since each additional parameter increased the computation time to generate a grid by a factor of four.

In this analysis the function that was minimized by MINUIT was χ^2

$$\chi^2 = \sum_i \frac{(y_i - z_i)^2}{\sigma_i^2} \qquad \text{(IV-61)}$$

where y_i is the number of experimental events in bin i, z_i is the

number of theoretical events in bin i, and σ_i is the error in the experimental value. In equation (IV-61) the theoretical value is assumed to be known precisely. In our case the theoretical values z_i, even after interpolation, are dependent upon Monte Carlo generated distributions and thus involve statistical fluctuations in the number of events in each time bin. Therefore, a sufficiently large number of events had to be generated in order to make the errors in the theoretical distribution small enough so that equation (IV-61) could be applied with validity. The necessary number of events was determined by fitting the experimental data using interpolation from a grid of Monte Carlos (which assumed a Maxwellian initial speed distribution for the μd atoms) containing N events and comparing the values of reduced χ^2 as a function of N. The grid spanned 1.30-2.50 eV in 0.40 eV steps along the mean energy axis and 1.60-2.50 by 0.30 steps along the molecular factor axis. The results of producing grids of Monte Carlos containing 10k,40k, and 100k events for the interpolation procedure is shown in Table XIII. Clearly there is considerable benefit in increasing the number of events from 10k to 40k. This is not surprising since at 10k the number of events in the Monte Carlos and in the experimental distributions are comparable. Increasing N to 100k had little effect on the value of reduced χ^2 and hence 40k events was chosen as a reasonable number of events to simulate in each Monte Carlo, while keeping computation time as small as practicable.

Table XIII
Effect of the Number of Events N in Each Monte Carlo on χ^2

N	mean energy (eV)	molecular factor	reduced χ^2
10 000	1.83 ± 0.02	2.36 ± 0.01	3.06
40 000	1.82 ± 0.02	2.10 ± 0.02	2.26
100 000	1.90 ± 0.03	2.06 ± 0.03	2.21

It should be stressed that the fit is not forced to remain within the grid boundaries and is perfectly free to choose any parameter values for χ^2 minimization.

It should also be noted that the experimental data of Table XI were not used directly in the fits, but were first adjusted to take into account the effects of muon decay on the number of observed events in each time bin. The "raw" experimental time distributions of Table XI can be adjusted in one of two ways. The first method is simply to multiply the number of events in each time bin of Table XI by a factor $e^{\lambda t}$, where λ is the free muon decay rate and t is the time at the center of each time bin. One might expect that since the half-widths of the time bins are small (20-40 ns) compared to the mean life of the muon (2.2 μs) this method would be accurate to within 1-2 %, and this expectation was borne out by the following test. The test method was the calculation of the expected value of the number of events in each time bin in the absence of decay

$$(IV\text{-}62) \qquad f(t) = \langle e^{\lambda t} f^{u}(t) \rangle = \frac{\int_{t_1}^{t_2} e^{\lambda t} f^{u}(t)\,dt}{\int_{t_1}^{t_2} dt}$$

where $f^{u}(t)$ is the "raw" experimental data and $t_1(t_2)$ defines the lower(upper) time in each time bin. The function $f^{u}(t)$, which is known at a discrete set of times (taken as the center of each time bin), can be determined for any value of t (within the observed range of times) via cubic spline interpolation from the values in Table XI. The integration in equation (IV-62) can then be performed numerically to produce the decay adjusted data f(t). The adjusted data obtained with the center of bin method are within 1-2 % of the adjusted values computed with equation (IV-62). In addition, for a given assumed speed distribution, identical parameter values (within errors) were obtained by MINUIT regardless of which method was used to adjust the experimental data. Since decay adjusted data were used in the fitting procedure the Monte Carlos could be generated without considering muon decay, resulting in a savings in computation time. For example, in a simulation at the D1520S condition ≈ 45 % of the μd atoms formed in the gas gap would decay before reaching a foil surface. Thus, to run a Monte Carlo with 40k events hitting the foil would require ≈ 80k events to be simulated, but using decay adjusted data enables the same simulation to require only a few percent over 40k events to be simulated (a few percent of the μd atoms would hit the sides of the foil stack).

IV.6 Discussion of Results

The interpolation method described in §IV.5 was used in all of the fits which are presented below. We reiterate the assumptions which were made in the generation of the Monte Carlo (MC) grids: the μd atoms were formed uniformly between the foils (but see below); the functional form of the initial speed distribution of the μd atoms was fixed; the μd atoms were initially moving isotropically; the nuclear cross sections were taken from reference [12] and scaled by an energy independent constant to simulate molecular cross sections (but see below).

It is rather easy to obtain a good fit (in a statistical sense) to the data if data for each condition are analyzed separately. For example, Table XIV presents the results of fitting only the D188S condition using a Maxwell speed distribution, one molecular factor, and uniform μd formation between the foils. As can be seen, a χ^2_ν of near 1.0 can be obtained by omitting the 60 ns bin from the fit. However, the mean energy is significantly different from the case when all seven or eight conditions are fitted simultaneously (see below). We do not attribute any physical significance to this difference, preferring to focus on the results of simultaneously including all conditions in a single "master" analysis with high statistics and $\approx$ 180 degrees of freedom.

Clearly a master fit to all of the available data constrains the interpretation of the experiment to a much greater

degree. Therefore, all of the experimental conditions were used in the fits except for the D94S data, which contained larger fractional errors than the other experimental conditions. In other words, the weight of the D94S data was too small to affect the fit results. The effect of data points with small weight was also seen when attempts were made to fit the late time tails of the foil hit distributions at the D188S condition (see below). The weight of these data points was too small to affect the MINUIT determination of the best parameter values. Omitting the D94S data from most of the analysis (once the "best" parameter values were determined a final fit <u>including D94S</u> was generated to all eight conditions) saved computing time during the generation of MC grids.

The results of fits using one energy independent molecular factor and a variety of initial speed distributions are shown in Table XV. (In Tables XIV-XX, comments which appear in block letters apply to all of the fits presented in the table.) A Maxwell speed distribution, characterized by the mean energy 3KT/2 (which corresponds to the rms speed), contained speeds in the range $0<v<v_m$. The maximum speed v_m was defined to be 2.5 times the mean speed so that this upper limit included almost 99.9 % of the area under the Maxwell distribution. Although the reduced chi-square (χ^2_ν) of this fit was 2.26 for 178 degrees of freedom (ν), a visual comparison of the MC curves generated from interpolation and the experimental data showed a remarkably good fit. However, at late times it did appear that the MC

distribution fell below the experimental data at the lower pressure conditions (most noticeably at D188S), with this discrepancy decreasing with increasing pressure. Therefore, it seemed logical to increase the number of lower energy μd atoms in an attempt to lift the late time part of the time distributions. To check this deduction several speed distributions were assumed which contained a relatively larger low speed component than a Maxwell speed distribution. The first attempt to improve the fit employed a truncated Maxwellian, which treated the mean energy, the upper limit of the Maxwellian (no longer defined to be 2.5 times the mean speed), and the molecular factor as free parameters. As can be seen in Table XV, a maximum speed of $\approx$ 2.5 times the mean speed was preferred by MINUIT. A Gaussian speed distribution, with the mean energy, the ratio of the standard deviation (in speed) to the mean speed, and the molecular factor treated as free parameters, provided a negligible improvement over the Maxwellian. A rectangular speed distribution, i.e. equal probability for speeds between zero and some maximum speed (where the maximum energy is treated as a free parameter), produced a larger χ^2_ν than the others. It should be noted that the error in the maximum energy is anomalously small since MINUIT yielded a maximum energy which was just outside the range of the MC grid energies (see §IV.5). A final guess at an initial speed distribution was a combination of a Maxwellian with a fixed mean energy and a rectangular distribution. The maximum energy in the rectangular distribution

and the relative area of the rectangle to the total area (≡ 1.0) were treated as free parameters. The mean energy of the Maxwellian was fixed at 1.90 eV and the molecular factor was fixed at 2.06, these values taken from the 100k events per grid point entry of Table XIII. This combination of speed distributions also had a small effect on χ^2_ν . Incidentally, a delta function initial speed distribution produced reduced chi-squares that were 5-15 times worse than a Maxwellian when preliminary attempts were made to fit only one condition at a time. Thus, there were no delta function MC grids created since it was clearly not a realistic initial speed distribution. Therefore, it appeared that a Maxwell initial speed distribution with an upper limit of 2.5 times the mean speed was at least as good as any other trial speed distribution, with the added benefit that it was only a one parameter distribution. It should be noted that there apparently is no physical significance behind the Maxwellian in the sense that no equilibrium has been established. It just appears to simulate the data rather well.

Further insight into the interpretation of the data would often come when certain portions of the data were fitted separately. In particular, it was often of interest to treat the D188S, D375S, and D188D and the D750S, D1520S, and D750D conditions as two separate sets of data. For comparison with results to be discussed later, the fits using a Maxwell initial speed distribution with one molecular factor to these subsets of data are presented in Table XVI.

Recall that the assumption of an energy independent molecular factor was not expected to be valid. In fact, the available theoretical calculations suggested that the molecular factor increases at lower CM collision energies ϵ, with a value of $\approx$ 2.3 in the range .0485 < ϵ < 0.25 eV [51,53]. (The molecular factor is energy dependent in this range but a rough approximation yields a value of about 2.3.) Therefore, the next simulations involved a Maxwellian speed distribution with two molecular factors, each constant over the applicable energy region. Thus, one of these applied to collision energies less than some crossover energy E' in the CM, the other to collisions with ϵ > E'. One might expect that at higher energies the molecular factor would approach 2.0 since the de Broglie wavelength of a 1 eV μd atom is $\approx$ 0.19 Å, which is smaller than the 0.74 Å equilibrium separation of the atoms in a D_2 molecule, hence at high enough energies the μd atom may interact with only one atom in the molecule. However, the molecular factor extracted from fits to all of the experimental conditions indicated that a molecular factor of 2.10 for the "high" energy region might be more appropriate. The low energy molecular factor was taken to be 2.30 (the approximate prediction of references [51,53]), 2.50, and 2.70. The results are presented in Table XVII. Apparently, there is not much sensitivity to the value of the low energy molecular factor and thus 2.30 was considered to be a reasonable value. The crossover energy E' of $\approx$ 0.30 eV in the CM is in good agreement with theory [51,53]. It can be seen that there is an

improvement (reduction) in χ^2_ν from 2.26 to 1.88 when a second molecular factor is added, with most of the improvement originating in the higher pressure (and scattering) conditions D750S, D1520S, and D750D.

It was evident from tabulating the contributions to chi-square from each time bin that the earliest time bin (the 60 ns bin for all conditions except D188D, in which case it was the 100 ns bin) made an extremely large contribution to χ^2 at the low pressure conditions. This discrepancy between the MC time distribution and the earliest time bin decreased in a consistent manner as the pressure increased. In fact, the fit to the first time bin in the D750S, D1520S, and D750D conditions was excellent. It was hypothesized that the cause of this discrepancy arose either from background subtraction or a non-uniform stopping distribution of muons in the foil gap.

The background from the prompt stops in the Au layer on the foils is clearly strongest at early times and thus the background subtraction is most sensitive in the earliest time bin. This sensitivity decreases as the pressure increases due to the increased number of muons stopping in the gas, which results in a larger delayed signal being produced. This sensitivity may lead to a background subtraction which is less accurate at the 60 ns time bin. (Recall that the subtraction in the 20 ns time bin left results which were statistically consistent with zero.) The results of fitting the data with the first time bin removed are shown in Table XVIII. The Gaussian initial speed distribution is

included to demonstrate that this effect is independent of the assumed initial speed distribution. The parameter values appear to be stable (within error) when the first time bin is omitted. Clearly, there is benefit from excluding the first time bin, e.g. χ^2_ν for the Maxwellian fit with one molecular factor is cut from 2.26 to 1.70, and for the two molecular Maxwellian fit from 1.88 to 1.38. Also, note the large improvement in χ^2_ν (from 2.11 to 1.41) when the D188S, D375S, and D188D conditions are fit when the first bin is omitted. At the same time, the higher pressure conditions (D750S, D1520S, D750D) showed a much smaller improvement in χ^2_ν from 1.39 to 1.25 (compare Tables XVII and XVIII). This is consistent with the idea that the background subtraction is most sensitive at 60 ns for the lower pressure conditions.

Alternatively, the presence of a "void" in the stopping distribution of muons between the foils would certainly diminish the number of events in the first time bin. Such a non-uniform stopping distribution is conceivable since the total stopping power of the gas in each foil gap at the D188S condition is only 7 $\mu g/cm^2$. Thus, there may exist a region in the foil gap (near the upstream foil) in which fewer muons stop than in the rest of the gap. To test for this possibility, a fit was run to a grid of MC's which were generated with a void of various sizes in the stopping distribution of the muons between the foils. It was assumed that no μd atoms were formed within this void and that the μd atoms were formed uniformly in the remainder of the foil

gap, with the size of the void scaling inversely with pressure. The results of using such a void in conjunction with a Maxwellian speed distribution and two molecular factors are shown in Table XIX. The molecular factors were defined to be 2.10 for ϵ > 0.30 eV and 2.30 for ϵ < 0.30 eV. It can be seen that there is some improvement in χ^2_ν (from 1.88 to 1.61), although perhaps not enough to justify the assumption of a pressure dependent void in the stopping distribution. However, it is difficult to prove that a 1 $\mu g/cm^2$ void does not exist. Omitting the first time bin from the void fit has no benefit over the fit to a grid of MC's which assumed a uniform stopping distribution in the entire foil gap since the presence of such a small void predominately affects only the earliest time bin.

The results of the "best" fit values to all of the experimental conditions, including D94S, are shown in Table XX. These fits used a Maxwellian speed distribution (with a maximum speed cutoff at 2.5 times the mean speed), two molecular factors (2.10 for ϵ > E' and 2.30 for ϵ < E'), and assumed the μd atoms were formed uniformly between the foils. The mean energy of the Maxwellian and the crossover energy E' were treated as free parameters. The parameter values were unchanged when the D94S data was included in the fit, and the increase in χ^2_ν was not considered significant.

The fits to the eight experimental conditions using the parameter values of Table XX (with the first bin omitted) are shown in Figures 14-21. The number of events in the 80 ns wide

bins have been divided in half for plotting purposes only, and the data have been adjusted to remove the effect of muon decay (this procedure is denoted by DC ≡ Decay Corrected). The poorer fit at the 60 ns bin for the D94S and D188S conditions, and at the 100 ns bin for the D188D condition can readily be seen, as can the discrepancy at late times in the lowest pressure conditions. This disagreement at late times is of course magnified by plotting the time distributions on a logarithmic scale. However, it is remarkable that such a simple two parameter fit can simulate the data so well.

Table XIV
Fit to D188S Condition Only

MAXWELLIAN SPEED DISTRIBUTION

Time Bins	$\bar{E}$ (eV)	Molecular Factor	χ^2_ν	ν
All	1.50 ± 0.05	2.31 ± 0.17	1.87	18
Omit First Time Bin	1.52 ± 0.06	2.32 ± 0.18	1.08	17

Table XV
Fits Using Different Initial Speed Distributions f(v)

ALL 7 CONDITIONS

ALL TIME BINS

f(v)	$\bar{E}$ (eV)	Cutoff*$\bar{v}$	Mol. Fac.	χ^2_ν	ν
Maxwellian	1.82 ± 0.02	≡ 2.50	2.10 ± 0.02	2.26	178
Truncated Maxwellian	1.92 ± 0.02	2.47 ± 0.04	2.03 ± 0.02	2.29	177

f(v)	$\bar{E}$ (eV)	$\sigma_v/\bar{v}$	Mol. Fac.	χ^2_ν	ν
Gaussian	1.56 ± 0.02	0.36 ± 0.04	2.22 ± 0.03	2.20	177

f(v)	Max. E (eV)	Rel. Area	Mol. Fac.	χ^2_ν	ν
Rectangular	4.10 ± 0.0007	≡ 1.0	2.19 ± 0.02	6.43	178
Rectangular with fixed Maxwellian ($\bar{E}$=1.90 eV)	2.90 ± 0.39	0.06 ± 0.02	≡ 2.06	2.35	178

Mol. Fac. = Molecular Factor
Rel. Area = Relative Area of Rectangular Distribution
Max. E = Maximum Energy in Rectangular Distribution

Table XVI
Fits to Subsets of Data

MAXWELLIAN SPEED DISTRIBUTION
ALL TIME BINS

Conditions	$\bar{E}$ (eV)	Mol. Fac.	χ^2_ν	ν
All 7	1.82 ± 0.02	2.10 ± 0.02	2.26	178
D188S,D375S,D188D	1.74 ± 0.05	2.32 ± 0.10	2.20	66
D750S,D1520S,D750D	1.92 ± 0.04	2.06 ± 0.03	1.72	82

Mol. Fac. = Molecular Factor

Table XVII
Two Molecular Factor Fits

MAXWELLIAN SPEED DISTRIBUTION

ALL TIME BINS

Conditions	Molecular Factor $\epsilon<E'$	Molecular Factor $\epsilon>E'$	$\bar{E}$ (eV)	E' (eV)	χ^2_ν	ν
All 7	2.30	2.10	1.82 ± 0.02	0.32 ± 0.02	1.88	178
All 7	2.50	2.10	1.86 ± 0.02	0.14 ± 0.02	1.94	178
All 7	2.70	2.10	1.65 ± 0.04	0.36 ± 0.01	1.83	178
D188S D375S D188D	2.30	2.10	1.73 ± 0.04	0.26 ± 0.04	2.11	66
D750S D1520S D750D	2.30	2.10	1.88 ± 0.04	0.33 ± 0.02	1.39	82
All 7	2.10 ± 0.02		1.82 ± 0.02	———	2.26	178

E' = Crossover Energy in CM
ϵ = Collision Energy in CM

Table XVIII
The Effect of Removing the First Time Bin from the Fit

ALL 7 CONDITIONS

f(v)	$\bar{E}$ (eV)	$\sigma_v/\bar{v}$	Mol. Fac.	χ^2_ν	ν
Maxwellian	1.83 ± 0.03	——	2.12 ± 0.02	1.70	171
Gaussian	1.58 ± 0.02	0.42 ± 0.03	2.23 ± 0.03	1.58	170

MAXWELLIAN SPEED DISTRIBUTION

Conditions	Molecular Factor ϵ<E'	Molecular Factor ϵ>E'	$\bar{E}$ (eV)	E' (eV)	χ^2_ν	ν
All 7	2.30	2.10	1.86 ± 0.02	0.33 ± 0.02	1.38	171
All 7	2.50	2.10	1.90 ± 0.02	0.13 ± 0.02	1.46	171
All 7	2.70	2.10	1.88 ± 0.02	0.14 ± 0.02	1.59	171
D188S D375S D188D	2.30	2.10	1.79 ± 0.04	0.27 ± 0.04	1.41	63
D750S D1520S D750D	2.30	2.10	1.91 ± 0.04	0.35 ± 0.02	1.25	79

Mol. Fac. = molecular factor
E' = Crossover Energy in CM
ϵ = Collision Energy in CM

Table XIX
The Effect of a Non-Uniform Muon Stopping Distribution

MAXWELLIAN SPEED DISTRIBUTION

TWO MOLECULAR FACTORS: 2.30 if $\epsilon < E'$; 2.10 if $\epsilon > E'$

ALL 7 CONDITIONS

Time Bins	Void ($\mu g/cm^2$)	$\bar{E}$ (eV)	E' (eV)	χ^2_ν	ν
All	NONE	1.82 ± 0.02	0.32 ± 0.02	1.88	178
All	1.05 ± 0.14	1.91 ± 0.03	≡ 0.30	1.61	178
Omit First Time Bin	NONE	1.86 ± 0.02	0.33 ± 0.02	1.38	171
Omit First Time Bin	0.58 ± 0.14	1.90 ± 0.03	≡ 0.30	1.43	171

E' = Crossover Energy in CM
ϵ = Collision Energy in CM

Table XX
Fit to All Eight Experimental Conditions

MAXWELLIAN SPEED DISTRIBUTION

TWO MOLECULAR FACTORS: 2.30 if $\epsilon < E'$; 2.10 if $\epsilon > E'$

Time Bins	Conditions	$\bar{E}$ (eV)	E' (eV)	χ^2_ν	ν
All	All 7	1.82 ± 0.02	0.32 ± 0.02	1.88	178
All	All 8	1.78 ± 0.02	0.32 ± 0.02	2.20	193
Omit First Time Bin	All 7	1.86 ± 0.02	0.33 ± 0.02	1.38	171
Omit First Time Bin	All 8	1.82 ± 0.02	0.32 ± 0.02	1.58	185

E' = Crossover Energy in CM
ϵ = Collision Energy in CM

Chapter V

CONCLUSIONS

The initial speed distribution (assumed to be isotropic) of the μd atoms is described rather well (see Table XX) by a Maxwell speed distribution of mean energy (3KT/2) 1.8 ± 0.1 eV. The error of 0.1 eV is estimated from the range in the values of the mean energy resulting from different fits to the data which used similar assumptions. For example, the truncated Maxwellian fit of Table XV produces a mean energy of 1.92 ± 0.02 eV even with a very similar cutoff in the Maxwell speed distribution and molecular factor. In fact, in all of the fits which assumed a Maxwell initial speed distribution, the value of the mean energy was determined to be between 1.7 and 1.9 eV.

By simple momentum and energy conservation arguments, the mean μd initial energy of 1.8 eV would imply that the energy of the muon at the time of capture would be about 80 eV if the entire D_2 molecule was involved in the capture process. Such a high muon energy is closer to the predictions of references [28] and [29] than to the other capture theories discussed in §II.2, most of which predict muon energies before capture of less than the ionization potential of hydrogen. The analysis also indicates

that the theoretical nuclear scattering cross sections of Bubak and Faifman [12] appear to agree well with experiment when a molecular factor is included. There is clear benefit to using two molecular factors to scale the nuclear cross sections to molecular cross sections in the Monte Carlo simulation (see Table XVII). The best values of the molecular factors were determined to be 2.10 for $\epsilon > 0.30$ eV and 2.30 for $\epsilon < 0.30$ eV, where ϵ is the collision energy in the center of mass. These values are also in fair agreement with theoretical predictions [51,53]. Of course, theoretical molecular scattering cross sections which can be used directly in a Monte Carlo simulation would be helpful in any future analysis.

The D_2 data described and analyzed here have demonstrated the feasibility and importance of performing this type of experiment at pressures as low as 100 mbar, two orders of magnitude below previously attempted pressures. In particular, the analysis has demonstrated the importance of performing this experiment at pressures low enough to insure that transfer of muons to the surface layer of carbon is not realized (see §IV.2.4). Additionally, the use of many different pressures and spacings has proved a valuable constraint on interpretation of the data, helping to show clearly the separate influences of the initial velocity distribution and of subsequent scattering processes on the μd diffusion phenomenon.

The results are of direct significance to studies of muon catalyzed fusion, and (together with a similar experiment

performed in hydrogen), to studies of weak interactions of muons.

APPENDIX A

The Effective Hamiltonian for Muon Absorption by a Proton

We start by recalling equations (I-11),(I-13), and (I-14)

$$(A\text{-}1) \qquad M = \frac{G_F \cos\theta}{\sqrt{2}} \int d^3x \, \bar{\Psi}_n \hat{O} \Psi_p$$

$$(A\text{-}2) \qquad \hat{O} = f_V \gamma^\lambda j_\lambda + i f_W \sigma^{\lambda\nu} q_\nu j_\lambda - f_A \gamma^\lambda \gamma_5 j_\lambda - f_P q^\lambda \gamma_5 j_\lambda$$

$$(A\text{-}3) \qquad j_\lambda = \bar{\Psi}_\nu \gamma_\lambda (1 - \gamma_5) \Psi_\mu$$

where second class terms have been omitted (§I.2). The nucleon motions are non-relativistic (the proton is assumed to be at rest and the energy of the final state neutron is $\approx$ 5 MeV) so the nucleon wave functions (one particle per unit volume normalization) have the form

$$(A\text{-}4) \qquad \Psi = \left[\frac{E + m}{2m}\right]^{\frac{1}{2}} \begin{bmatrix} \chi \\ \frac{\sigma_A \cdot p}{E+m} \chi \end{bmatrix} \rightarrow \begin{bmatrix} \chi \\ \frac{\sigma_A \cdot p}{2m} \chi \end{bmatrix}$$

where m represents the nucleon mass, i.e the neutron-proton mass difference has been neglected, χ is a two-component Pauli wave function, and σ_A is the nucleon Pauli spin operator. Then

$$(A\text{-}5) \qquad \Psi_p = \begin{bmatrix} \chi_p \\ \frac{\sigma_A \cdot p}{2m} \chi_p \end{bmatrix} \approx \begin{bmatrix} \chi_p \\ 0 \end{bmatrix}$$

$$(A\text{-}6) \qquad \bar{\Psi}_n = \Psi_n^\dagger \gamma^0 = (\chi_n^\dagger, \chi_n^\dagger \frac{\sigma_A \cdot p_n}{2m}) \begin{bmatrix} 1 & 0 \\ 0 & -1 \end{bmatrix} = (\chi_n^\dagger, -\chi_n^\dagger \frac{\sigma_A \cdot p_n}{2m})$$

The muon is absorbed from the 1S state [5] and therefore for muon absorption by a proton

$$(A\text{-}7) \qquad \Psi_\mu(r) = \frac{1}{(\pi a_0^3)^{\frac{1}{2}}} e^{-r/a_0} u_\mu = \phi_\mu u_\mu = \phi \begin{bmatrix} \chi_\mu \\ 0 \end{bmatrix}$$

where the muon Bohr radius $a_0 = h^2/m'e^2$ and m' is the reduced mass of the muon-nucleus system. The neutrino wave function can be expressed as a plane wave :

$$\text{(A-8)} \qquad \Psi_\nu(r) = \frac{1}{\sqrt{2}} e^{ip_\nu \cdot r} \begin{bmatrix} \chi_\nu \\ \sigma \cdot \hat{p}_\nu \chi_\nu \end{bmatrix}$$

Since $j_\lambda = (j_0, -j)$, equation (A-3) can be decomposed into

$$j_0 = \bar{\Psi}_\nu \gamma_0 (1 - \gamma_5) \Psi_\mu = (\chi_\nu^\dagger, -\chi_\nu^\dagger \sigma \cdot \hat{p}_\nu) \begin{bmatrix} 1 & -1 \\ 1 & -1 \end{bmatrix} \begin{bmatrix} \chi_\mu \\ 0 \end{bmatrix} \phi_\mu \frac{1}{\sqrt{2}} e^{-ip_\nu \cdot x}$$

$$\text{(A-9)} \qquad j_0 = \frac{1}{\sqrt{2}} [\chi_\nu^\dagger (1 - \sigma \cdot \hat{p}_\nu) \chi_\mu] \phi_\mu e^{-ip_\nu \cdot x}$$

$$j = \bar{\Psi}_\nu \gamma (1 - \gamma_5) \Psi_\mu = (\chi_\nu^\dagger, -\chi_\nu^\dagger \sigma \cdot \hat{p}_\nu) \begin{bmatrix} -\sigma & \sigma \\ -\sigma & \sigma \end{bmatrix} \begin{bmatrix} \chi_\mu \\ 0 \end{bmatrix} \phi_\mu \frac{1}{\sqrt{2}} e^{-ip_\nu \cdot x}$$

$$\text{(A-10)} \qquad j = -\frac{1}{\sqrt{2}} [\chi_\nu^\dagger (1 - \sigma \cdot \hat{p}_\nu) \sigma \chi_\mu] \phi_\mu e^{-ip_\nu \cdot x}$$

Now, looking at the various terms in equation (A-1) :

<u>Vector</u> $\qquad f_V \bar{\Psi}_n \gamma^\lambda j_\lambda \Psi_p$

$$\gamma^\lambda j_\lambda = \gamma^0 j_0 - \gamma \cdot j$$

$$\text{(A-11)} \qquad f_V \bar{\Psi}_n \gamma^\lambda j_\lambda \Psi_p = f_V \bar{\Psi}_n \gamma^0 j_0 \Psi_p - f_V \bar{\Psi}_n \gamma \cdot j \Psi_p$$

$$f_V \bar{\Psi}_n \gamma^0 j_0 \Psi_p = (\chi_{n'}^\dagger, -\chi_n^\dagger \frac{\sigma_A \cdot p_n}{2m}) [\chi_\nu^\dagger (1 - \sigma \cdot \hat{p}_\nu) \chi_\mu] \frac{\phi_\mu}{\sqrt{2}} e^{-ip_\nu \cdot x} \begin{bmatrix} \chi_p \\ 0 \end{bmatrix}$$

$$\text{(A-12)} \qquad f_V \bar{\Psi}_n \gamma^0 j_0 \Psi_p = \frac{f_V}{\sqrt{2}} e^{-ip_\nu \cdot x} \phi_\mu [\chi_n^\dagger \chi_\nu^\dagger (1 - \sigma \cdot \hat{p}_\nu) \chi_\mu \chi_p]$$

$$f_V \bar{\Psi}_n \gamma \cdot j \Psi_p = -\frac{f_V}{\sqrt{2}} e^{-ip_\nu \cdot x} \phi_\mu (\chi_{n'}^\dagger, -\chi_n^\dagger \frac{\sigma_A \cdot p_n}{2m}) \begin{bmatrix} 0 & \sigma_A \\ -\sigma_A & 0 \end{bmatrix}$$

$$\cdot [\chi_\nu^\dagger (1 - \sigma \cdot \hat{p}_\nu) \sigma \chi_\mu] \begin{bmatrix} \chi_p \\ 0 \end{bmatrix}$$

$$f_V\bar{\Psi}_n\gamma\cdot j\Psi_p = -\frac{f_V}{\sqrt{2}}\, e^{-ip_\nu\cdot x}\,\phi_\mu[x_n^\dagger x_\nu^\dagger(1-\sigma\cdot\hat{p}_\nu)\,\frac{\sigma_A\cdot p_n}{2m}\,\sigma_A\cdot\sigma x_\mu x_p]$$

Using $\sigma\cdot A\sigma\cdot B = A\cdot B + i\sigma\cdot AxB$ and since momentum conservation requires $p_n = -p_\nu$ (for muon absorption at rest) and $q = -p_n$ yields

$$f_V\bar{\Psi}_n\gamma\cdot j\Psi_p = -\frac{f_V}{\sqrt{2}}\, e^{-ip_\nu\cdot x}\,\phi_\mu(x_n^\dagger x_\nu^\dagger(1-\sigma\cdot\hat{p}_\nu)[\frac{-\sigma\cdot p_\nu}{2m} - \frac{i\sigma_A\cdot q}{2m}\, x\ \sigma]x_\mu x_p\}$$

Then from the Dirac equation for the neutrino

$$-\sigma\cdot p_\nu\, x_\nu = E_\nu\, x_\nu \quad \text{or} \quad -x_\nu^\dagger\sigma\cdot p_\nu = E_\nu\, x_\nu^\dagger$$

$$\text{(A-13)}\quad f_V\bar{\Psi}_n\gamma\cdot j\Psi_p = -\frac{f_V}{\sqrt{2}}\, e^{-ip_\nu\cdot x}\,\phi_\mu(x_n^\dagger x_\nu^\dagger(1-\sigma\cdot\hat{p}_\nu)[\frac{E_\nu}{2m} - \frac{i\sigma_A\cdot q}{2m}\, x\ \sigma]x_\mu x_p\}$$

Therefore, using (A-12) and (A-13) the vector term becomes

$$\text{(A-14)}\quad f_V\bar{\Psi}_n\gamma^\lambda j_\lambda\Psi_p = \frac{f_V}{\sqrt{2}}\, e^{-ip_\nu\cdot x}\,\phi_\mu([x_n^\dagger x_\nu^\dagger(1-\sigma\cdot\hat{p}_\nu)x_\mu x_p]\cdot(1+\frac{E_\nu}{2m}) - \frac{i}{2m}\,[x_n^\dagger x_\nu^\dagger(1-\sigma\cdot\hat{p}_\nu)\sigma_A\cdot q x\sigma x_\mu x_p])$$

<u>Weak Magnetism</u> $if_W\bar{\Psi}_n\sigma^{\alpha\beta}q_\beta j_\alpha\Psi_p = if_W\bar{\Psi}_n\sigma^{0k}q_k j_0\Psi_p + if_W\bar{\Psi}_n\sigma^{kl}q_l j_k\Psi_p$

Using $\sigma^{\alpha\beta} = \frac{i}{2}[\gamma^\alpha\gamma^\beta - \gamma^\alpha\gamma^\beta]$ and expressing the momentum transfer q in contravariant form ($q^\beta=(q^0,q)$ and $q_\beta=(q^0,-q)$) gives

$$if_W\bar{\Psi}_n\sigma^{\alpha\beta}q_\beta j_\alpha\Psi_p = -if_W\bar{\Psi}_n\sigma^{0k}q^k j_0\Psi_p - if_W\bar{\Psi}_n\sigma^{kl}q^l j_k\Psi_p$$

$$-i\sigma^{0k}q^k = \tfrac{1}{2}[\gamma^0\gamma^k - \gamma^k\gamma^0]q^k = \begin{bmatrix} 0 & \sigma^k \\ \sigma^k & 0 \end{bmatrix} q^k = \begin{bmatrix} 0 & \sigma\cdot\mathbf{q} \\ \sigma\cdot\mathbf{q} & 0 \end{bmatrix}$$

This will give rise to a term that is $\alpha\ \sigma_A\cdot p_n \sigma\cdot q\ \alpha\ q^2$ since $q = p_n$.

$$-i\sigma^{kl}q^l = \tfrac{1}{2}[\gamma^k\gamma^l - \gamma^l\gamma^k]q^l = \gamma^k\gamma^l q^l$$

$$-i\sigma^{kl}q^l = \begin{bmatrix} 0 & \sigma^k \\ -\sigma^k & 0 \end{bmatrix}\begin{bmatrix} 0 & \sigma^l \\ -\sigma^l & 0 \end{bmatrix} q^l = \begin{bmatrix} -i\epsilon_{klm}\sigma^m & 0 \\ 0 & -i\epsilon_{klm}\sigma^m \end{bmatrix} q^l$$

since $\sigma^k\sigma^l = \delta^{kl} + i\epsilon_{klm}\sigma^m \Rightarrow i\epsilon_{klm}\sigma^m$ here since if k=l then $\sigma^{kl} = 0$. Then using $(q\times\sigma_A)^k = \epsilon_{klm}q^l\sigma^m$

$$-i\sigma^{kl}q^l = -i\begin{bmatrix} q\times\sigma_A & 0 \\ 0 & q\times\sigma_A \end{bmatrix}$$

To lowest order in q :

$$if_W\bar{\psi}_n\sigma^{kl}q_l j_k\psi_p = \frac{if_W}{\sqrt{2}}\, e^{-ip_\nu\cdot x}\,\phi_\mu\Big((\chi_n^\dagger, -\chi_n^\dagger\frac{\sigma_A\cdot p_n}{2m})[\chi_\nu^\dagger(1-\sigma\cdot\hat{p}_\nu)]$$

$$\cdot\begin{bmatrix} q\times\sigma_A & 0 \\ 0 & q\times\sigma_A \end{bmatrix}\sigma\chi_\mu\begin{bmatrix}\chi_p \\ 0\end{bmatrix}\Big)$$

$$= \frac{if_W}{\sqrt{2}}\, e^{-ip_\nu\cdot x}\,\phi_\mu[\chi_n^\dagger\chi_\nu^\dagger(1-\sigma\cdot\hat{p}_\nu)\,q\times\sigma_A\cdot\sigma\chi_\mu\chi_p]$$

$$(q\times\sigma_A)\cdot\sigma = \sigma_A\cdot(\sigma\times q) = -\sigma_A\cdot(q\times\sigma)$$

$$\text{(A-15)}\quad if_W\bar{\psi}_n\sigma^{\alpha\beta}q_\beta j_\alpha\psi_p = \frac{-if_W}{\sqrt{2}}\, e^{-ip_\nu\cdot x}\,\phi_\mu[\chi_n^\dagger\chi_\nu^\dagger(1-\sigma\cdot\hat{p}_\nu)\sigma_A\cdot q\times\sigma\chi_\mu\chi_p]$$

Axial Vector

$$f_A\bar{\psi}_n\gamma^\alpha\gamma^5 j_\alpha\psi_p = -f_A\bar{\psi}_n\gamma^5\gamma^\alpha j_\alpha\psi_p = -f_A\bar{\psi}_n\gamma^5\gamma^0 j_0\psi_p + f_A\bar{\psi}_n\gamma^5\gamma\cdot j\psi_p$$

$$-f_A\bar{\psi}_n\gamma^5\gamma^0 j_0\psi_p = \frac{-f_A}{\sqrt{2}}\, e^{-ip_\nu\cdot x}\phi_\mu\{(x_n^\dagger, -x_n^\dagger\frac{\sigma_A\cdot p_n}{2m})\begin{bmatrix}0 & -1\\ 1 & 0\end{bmatrix}$$

$$\cdot[x_\nu^\dagger(1-\sigma\cdot\hat{p}_\nu)x_\mu]\begin{bmatrix}x_p\\ 0\end{bmatrix}\}$$

$$-f_A\bar{\psi}_n\gamma^5\gamma^0 j_0\psi_p = \frac{f_A}{\sqrt{2}}\, e^{-ip_\nu\cdot x}\phi_\mu\{x_n^\dagger x_\nu^\dagger(1-\sigma\cdot\hat{p}_\nu)\frac{\sigma_A\cdot p_n}{2m}\, x_\mu x_p\}$$

since $\sigma_A\cdot p_n = -\sigma_A\cdot p_\nu = -E_\nu\sigma_A\cdot\hat{p}_\nu$

$$\text{(A-16)}\quad -f_A\bar{\psi}_n\gamma^5\gamma^0 j_0\psi_p = \frac{-f_A}{\sqrt{2}}\, e^{-ip_\nu\cdot x}\phi_\mu\,\frac{E_\nu}{2m}\,\{x_n^\dagger x_\nu^\dagger(1-\sigma\cdot\hat{p}_\nu)\sigma_A\cdot\hat{p}_\nu x_\mu x_p\}$$

$$f_A\bar{\psi}_n\gamma^5\gamma\cdot j\psi_p = \frac{-f_A}{\sqrt{2}}\, e^{-ip_\nu\cdot x}\phi_\mu\{(x_n^\dagger, -x_n^\dagger\frac{\sigma_A\cdot p_n}{2m})\begin{bmatrix}-\sigma_A & 0\\ 0 & \sigma_A\end{bmatrix}$$

$$\cdot[x_\nu^\dagger(1-\sigma\cdot\hat{p}_\nu)\sigma x_\mu]\begin{bmatrix}x_p\\ 0\end{bmatrix}\}$$

$$\text{(A-17)}\quad f_A\bar{\psi}_n\gamma^5\gamma\cdot j\psi_p = \frac{f_A}{\sqrt{2}}\, e^{-ip_\nu\cdot x}\phi_\mu\{x_n^\dagger x_\nu^\dagger(1-\sigma\cdot\hat{p}_\nu)\sigma\cdot\sigma_A x_\mu x_p\}$$

Combining (A-16) and (A-17) yields

$$\text{(A-18)}\quad f_A\bar{\psi}_n\gamma^\alpha\gamma^\beta j_\alpha\psi_p = \frac{f_A}{\sqrt{2}}\, e^{-ip_\nu\cdot x}\phi_\mu\{\frac{-E_\nu}{2m}\,[x_n^\dagger x_\nu^\dagger(1-\sigma\cdot\hat{p}_\nu)\sigma_A\cdot\hat{p}_\nu x_\mu x_p]$$

$$+\,[x_n^\dagger x_\nu^\dagger(1-\sigma\cdot\hat{p}_\nu)\sigma\cdot\sigma_A x_\mu x_p]\}$$

Induced Pseudoscalar

$$f_p\bar{\psi}_n\gamma^5 q^\alpha j_\alpha \psi_p = f_p\bar{\psi}_n\gamma^5 q^0 j_0\psi_p - f_p\bar{\psi}_n\gamma^5 \mathbf{q}\cdot\mathbf{j}\psi_p$$

$$f_p\bar{\psi}_n\gamma^5 q^0 j_0\psi_p = \frac{f_p}{\sqrt{2}}\, e^{-ip_\nu\cdot x}\phi_\mu\{(x_n^\dagger, -x_n^\dagger\frac{\sigma_A\cdot p_n}{2m})\begin{bmatrix}0 & q^0\\ q^0 & 0\end{bmatrix}$$
$$\cdot[x_\nu^\dagger(1-\sigma\cdot\hat{p}_\nu)x_\mu]\begin{bmatrix}x_p\\ 0\end{bmatrix}\}$$

$$f_p\bar{\psi}_n\gamma^5 q^0 j_0\psi_p = \frac{-f_p}{\sqrt{2}}\, e^{-ip_\nu\cdot x}\phi_\mu(x_n^\dagger x_\nu^\dagger(1-\sigma\cdot\hat{p}_\nu)\frac{\sigma_A\cdot p_n}{2m}\, q_0 x_\mu x_p\}$$

Since $q_0 = \frac{|p_n|^2}{2m} \alpha\ q^2$, the above expression is $\alpha\ q^3$.

$$-f_p\bar{\psi}_n\gamma^5 \mathbf{q}\cdot\mathbf{j}\psi_p = \frac{f_p}{\sqrt{2}}\, e^{-ip_\nu\cdot x}\phi_\mu\{(x_n^\dagger, -x_n^\dagger\frac{\sigma_A\cdot p_n}{2m})\begin{bmatrix}0 & \mathbf{q}\\ \mathbf{q} & 0\end{bmatrix}$$
$$\cdot[x_\nu^\dagger(1-\sigma\cdot\hat{p}_\nu)\sigma x_\mu]\begin{bmatrix}x_p\\ 0\end{bmatrix}\}$$

$$-f_p\bar{\psi}_n\gamma^5 \mathbf{q}\cdot\mathbf{j}\psi_p = \frac{-f_p}{\sqrt{2}}\, e^{-ip_\nu\cdot x}\phi_\mu(x_n^\dagger x_\nu^\dagger(1-\sigma\cdot\hat{p}_\nu)\frac{\sigma_A\cdot p_n}{2m}\, \sigma\cdot\mathbf{q} x_\mu x_p\}$$

$$\sigma\cdot\mathbf{q} = \sigma\cdot(p_n - p_p) = \sigma\cdot p_n = -\sigma\cdot p_\nu = -E_\nu\sigma\cdot\hat{p}_\nu$$

$$\sigma_A\cdot p_n = -\sigma_A\cdot p_\nu = -E_\nu\sigma_A\cdot\hat{p}_\nu$$

$$-f_p\bar{\psi}_n\gamma^5 \mathbf{q}\cdot\mathbf{j}\psi_p = \frac{-f_p}{\sqrt{2}}\, e^{-ip_\nu\cdot x}\phi_\mu\ \frac{E_\nu^2}{2m}(x_n^\dagger x_\nu^\dagger(1-\sigma\cdot\hat{p}_\nu)\ \sigma_A\cdot\hat{p}_\nu\sigma\cdot\hat{p}_\nu x_\mu x_p\}$$

Therefore, to lowest order in q

$$\text{(A-19)}\quad f_p\bar{\psi}_n\gamma^5 q^\alpha j_\alpha\psi_p = \frac{-f_p}{\sqrt{2}}\, e^{-ip_\nu\cdot x}\phi_\mu\ \frac{E_\nu^2}{2m}(x_n^\dagger x_\nu^\dagger(1-\sigma\cdot\hat{p}_\nu)\ \sigma_A\cdot\hat{p}_\nu\sigma\cdot\hat{p}_\nu x_\mu x_p\}$$

Defining $g_p \equiv -m_\mu f_p$ and also using $E_\nu(\text{GeV}) \approx m_\mu(1-(m_\mu/2)) \approx m_\mu$ (from momentum and energy conservation) in (A-19) produces

$$(A\text{-}20)\quad f_p\bar{\psi}_n\gamma^5 q^\alpha j_\alpha\psi_p = \frac{g_p}{\sqrt{2}}\, e^{-ip_\nu\cdot x}\,\phi_\mu\,\frac{E_\nu}{2m}\{x_n^\dagger x_\nu^\dagger(1-\sigma\cdot\hat{p}_\nu)\;\sigma_A\cdot\hat{p}_\nu\sigma\cdot\hat{p}_\nu x_\mu x_p\}$$

Substituting (A-14),(A-15),(A-18), and (A-20) into (A-1) yields

$$(A\text{-}21)\quad M = \frac{G_F\cos\theta}{2}\int d^3x\; e^{-ip_\nu\cdot x}\,\phi_\mu x_n^\dagger x_\nu^\dagger(1-\sigma\cdot\hat{p}_\nu)\{f_V(1+\frac{E_\nu}{2m})$$
$$- \frac{if_V}{2m}\,\sigma_A\cdot qx\sigma - if_W\sigma_A\cdot qx\sigma + f_A\,\frac{E_\nu}{2m}\,\sigma_A\cdot\hat{p}_\nu$$
$$- f_A\sigma\cdot\sigma_A - g_p\,\frac{E_\nu}{2m}\,\sigma_A\cdot\hat{p}_\nu\sigma\cdot\hat{p}_\nu\}x_\mu x_p$$

$$M = \frac{G_F\cos\theta}{2}\int d^3x\; e^{-ip_\nu\cdot x}\,\phi_\mu x_n^\dagger x_\nu^\dagger(1-\sigma\cdot\hat{p}_\nu)\{f_V(1+\frac{E_\nu}{2m})$$
$$+ \frac{if_V}{2m}\,\sigma\cdot\hat{p}_\nu\sigma_A\cdot qx\sigma + if_W\sigma\cdot\hat{p}_\nu\sigma_A\cdot qx\sigma + f_A\,\frac{E_\nu}{2m}\,\sigma_A\cdot\hat{p}_\nu$$
$$- f_A\sigma\cdot\sigma_A + g_p\,\frac{E_\nu}{2m}\,\sigma_A\cdot\hat{p}_\nu\}x_\mu x_p$$

$$\sigma\cdot\hat{p}_\nu[\sigma_A\cdot(qx\sigma)] = \sigma\cdot\hat{p}_\nu[\sigma\cdot(\sigma_A x q)] = E_\nu\sigma\cdot\hat{p}_\nu[\sigma\cdot(\sigma_A x\hat{p}_\nu)]$$
$$= E_\nu\{\hat{p}_\nu\cancel{\cdot}^{\,0}(\sigma_A x\hat{p}_\nu) + i\sigma\cdot(\hat{p}_\nu x(\sigma_A x\hat{p}_\nu))\}$$

$(AxBxC) = (A\cdot C)B - (A\cdot B)C$

$$= iE_\nu\{\sigma\cdot(\hat{p}_\nu\cdot\hat{p}_\nu)\sigma_A - \sigma\cdot(\hat{p}_\nu\cdot\sigma_A)\hat{p}_\nu\}$$
$$= iE_\nu\{\sigma\cdot\sigma_A - \sigma\cdot\hat{p}_\nu\sigma_A\cdot\hat{p}_\nu\}$$

$$M = \frac{G_F\cos\theta}{2}\int d^3x\; e^{-ip_\nu\cdot x}\,\phi_\mu x_n^\dagger x_\nu^\dagger(1-\sigma\cdot\hat{p}_\nu)\{f_V(1+\frac{E_\nu}{2m})$$
$$- f_V\,\frac{E_\nu}{2m}\,[\sigma\cdot\sigma_A - \sigma\cdot\hat{p}_\nu\sigma_A\cdot\hat{p}_\nu] - f_W E_\nu[\sigma\cdot\sigma_A - \sigma\cdot\hat{p}_\nu\sigma_A\cdot\hat{p}_\nu]$$
$$+ f_A\,\frac{E_\nu}{2m}\,\sigma_A\cdot\hat{p}_\nu - f_A\sigma\cdot\sigma_A + g_p\,\frac{E_\nu}{2m}\,\sigma_A\cdot\hat{p}_\nu\}x_\mu x_p$$

$$(A\text{-}22)\quad M = \frac{G_F\cos\theta}{2}\int d^3x\, e^{-ip_\nu\cdot x}\phi_\mu \chi_n^\dagger \chi_\nu^\dagger (1-\sigma\cdot\hat{p}_\nu)\{f_V(1+\frac{E_\nu}{2m})$$
$$- [\frac{E_\nu}{2m}(f_V + 2mf_W) + f_A]\sigma\cdot\sigma_A$$
$$- \frac{E_\nu}{2m}[(f_V+ 2mf_W) - f_A - g_p]\sigma_A\cdot\hat{p}_\nu\}\chi_\mu\chi_p$$

Then

$$(A\text{-}23)\quad M = \tfrac{1}{2}\int \chi_n^\dagger \chi_\nu^\dagger H \chi_\mu \chi_p e^{-ip_\nu\cdot x}\phi_\mu d^3x$$

where the effective Hamiltonian H is

$$(A\text{-}24)\quad H = (1-\sigma\cdot\hat{p}_\nu)[F_V + F_A\sigma_A\cdot\sigma + F_P\sigma_A\cdot\hat{p}_\nu]$$

with

$$(A\text{-}25)\quad F_V \equiv G_F\cos\theta\ f_V[1 + \frac{E_\nu}{2m}]$$

$$(A\text{-}26)\quad F_A \equiv G_F\cos\theta\ [-f_A - \frac{E_\nu}{2m}(f_V+ 2mf_W)]$$

$$(A\text{-}27)\quad F_P \equiv G_F\cos\theta\ \frac{E_\nu}{2m}[f_A - m_\mu f_P - (f_V+ 2mf_W)]$$

APPENDIX B

The purpose of this appendix is to derive an expression for the probability distribution of μd atoms arriving at a foil surface in the absence of scattering [66]. The μd atoms are assumed to form uniformly in the gas gap between two foils separated by a distance L, with the geometry as defined in Figure B-1. Consider the case of a μd atom

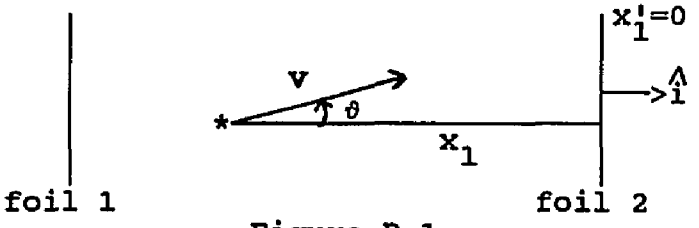

Figure B-1

formed at a distance x_1 from a foil surface. One can define G(x',v';x,v,t) as the probability distribution for a particle with initial position x and velocity v to be in a phase space element dx',dv' about x',v' after a time t such that

$$(B\text{-}1) \qquad \int G(x',v';x,v,t) = 1$$

for all time t. If it is assumed that the μd atoms do not scatter en route to the foils then the Green's function for the problem can be written as

$$(B\text{-}2) \qquad G(x',v';x,v,t) = \delta(v'-v)\delta(x'-x-vt)$$

and the probability distribution for a μd atom to strike an element of area dS on the foil surface is

$$(B\text{-}3) \qquad P(t) = \int dv'\{(dS\cdot v')G\}\{r(x,v)dxdv\}$$

where the term in the first bracket is the flux through the surface element dS and the term in the second bracket gives the

initial spatial and velocity distributions of the μd atoms such that

$$(B\text{-}4) \qquad \int r(x,v)\,dxdv = 1$$

For a semi-infinite geometry in the x_2 and x_3 directions it is convenient to assume that the μd atom forms at a position $(x_1, x_2=x_3=0)$. The function $r(x,v)$ can then be written

$$(B\text{-}5) \qquad r(x,v) = \frac{1}{L}\theta(0<x_1<L)\,\delta(x_2)\,\delta(x_3)\,f(v)$$

where $\theta(0<x_1<L)$ represents a rectangular pulse of unit amplitude between 0 and L and $f(v)$ is the initial velocity distribution. The probability for hitting a foil surface (equn. B-3) is then

$$P(t) = \int dv'dx_2'dx_3'v_1'\,\delta(x'-x-v't)\,\delta(v'-v)\,\frac{f(v)}{L}\,\theta(0<x_1<L)\,\delta(x_2)\,\delta(x_3)\,dxdv$$

since $dS = dx_2'dx_3'\hat{i}$. An integration over v' followed by an integration over $dx_2'dx_3'$ (since $\delta(A-B) = \delta(A_1-B_1)\delta(A_2-B_2)\delta(A_3-B_3)$ this only leaves the x_1 component) in conjunction with the fact that $dx_1 = \delta(x_2)\delta(x_3)dx$ yields

$$(B\text{-}7) \qquad P(t) = \frac{1}{L}\int v_1\,\delta(x_1'-x_1-v_1t)\,f(v)\,\theta(0<x_1<L)\,dx_1dv$$

From Figure B-1 it can be seen that $v_1 = v\cos\vartheta \equiv v\mu$, $x_1' = 0$ (the delta function becomes $\delta(x_1+v_1t)$), $x_1 = -v\mu t$ and also using $dv = v^2dvd(\cos\vartheta)d\varphi = v^2dvd\mu d\varphi$ allows (B-7) to be written as

$$(B\text{-}8) \qquad P(t) = \frac{2\pi}{L}\int_1^1 \mu d\mu \int_0^\infty v^3 f(v)\,\theta(0<-v\mu t<L)\,dv$$

where the 2π comes from the integral over φ due to azimuthal symmetry. Since $\theta(a<x<b) = \theta(x-a)\theta(b-x)$ one has

$$(B\text{-}9) \qquad \int_1^1 d\mu\,\theta(0<-v\mu t<L) = \int_1^1 d\mu\,\theta(-v\mu t)\,\theta(L+v\mu t) = \int_1^0 d\mu\,\theta(L+v\mu t)$$

$$= \int_0^1 d\mu\,\theta(L-v\mu t) = \int_0^1 d\mu\,\theta\left(\frac{L}{vt} - \mu\right)$$

The effect of the θ-function is to introduce two regions of integration in (B-8) since

for $t > \frac{L}{v}$ $\quad \theta(\frac{L}{vt} - \mu) \quad ==>$

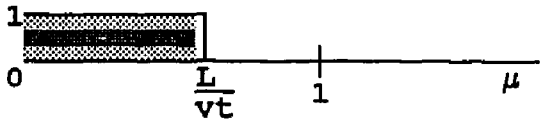

for $t < \frac{L}{v}$ $\quad \theta(\frac{L}{vt} - \mu) \quad ==>$

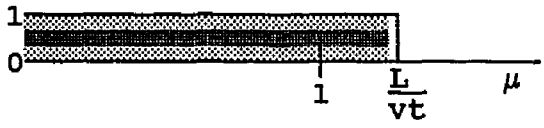

Thus, equation (B-8) can be broken up into two integrals

$$P_1(t) = \frac{2\pi}{L}\int_0^1 \mu d\mu \int_0^{L/t} v^3 f(v)dv \qquad t < \frac{L}{v}$$

(B-10)

$$P_2(t) = \frac{2\pi}{L}\int_0^{L/vt} \mu d\mu \int_{L/t}^{\infty} v^3 f(v)dv \qquad t > \frac{L}{v}$$

Then, in principle it is possible to determine the time distribution of the μd atoms as they hit the foil for a chosen f(v). Two simple examples :

1) a delta function $\qquad f(v) = \frac{\delta(v-v_0)}{4\pi v_0^2} \qquad$ (recall (B-4))

Here (B-10) becomes

$$P_1(t) = \frac{1}{2Lv_0^2}\int_0^1 \mu d\mu \int_0^{L/t} \delta(v-v_0)v^3 dv = \frac{v_0}{4L} \qquad t < \frac{L}{v_0}$$

(B-11)

$$P_2(t) = \frac{1}{2Lv_0^2}\int_0^{L/vt} \mu d\mu \int_0^{L/t} \delta(v-v_0)v^3 dv = \frac{L}{4v_0 t^2} \qquad t > \frac{L}{v_0}$$

This is the time distribution of μd atoms hitting one plane, so due to symmetry considerations equation (B-10) is multiplied by two to produce the time distribution for a set of two foils (equn. (II-23)).

2) a Maxwell distribution $$f(v) = \left[\frac{m}{2\pi kT}\right]^{3/2} \exp\left(\frac{-mv^2}{2kT}\right)$$

Substitution of this velocity distribution into (B-10) will yield a probability distribution for hitting either of two foils given by

$$(B\text{-}12) \qquad P(t) = \frac{1}{L}\left[\frac{2kT}{\pi m}\right]^{1/2} \left[1 - \exp\left(\frac{-mL^2}{2kTt^2}\right)\right]$$

Note that since there is a distribution of velocities (and not a unique velocity as in the delta function case) there are not two distinct regions in the predicted time distribution (B-12), i.e. one simply adds $P_1(t)$ and $P_2(t)$ to find $P(t)$. Of course, it will usually not be possible to determine $P(t)$ analytically as in these two cases, so that in general $P(t)$ must be determined numerically.

REFERENCES

1. T.D. Lee and C.N.Yang, Phys. Rev. 104, 254 (1956).

2. C.S. Wu, E. Ambler, R.W. Hayward, D.D. Hoppes, and R.P. Hudson, Phys. Rev. 105, 1413 (1957).

3. R.P. Feynman and M. Gell-Mann, Phys. Rev. 109, 193 (1958).

4. E.C.G. Sudarshan and R. Marshak, Phys. Rev. 109, 1860 (1958).

5. E.D. Commins and P.H. Bucksbaum, Weak Interactions of Leptons and Quarks (Cambridge University Press, Cambridge, 1983).

6. R.J. Blin-Stoyle, Fundamental Interactions and the Nucleus (North-Holland Publishing Company, Amsterdam, 1973).

7. A. Bertin, M. Capponi, I. Massa, M. Piccinini, G. Vannini, M. Poli, and A. Vitale, Nuov. Cim. 86A, 123 (1985).

8. H. Primakoff, Weak Interactions and High Energy Neutrino Physics, ed. T.D. Lee (Academic Press, New York, 1966).

9. J.E. Rothberg, E.W. Anderson, E.J. Bleser, L.M. Lederman, S.L. Meyer, J.L. Rosen, and I.T. Wang, Phys. Rev. 132, 2664 (1963).

10. G. Bardin, J. Duclos, A. Magnon, J. Martino, A. Richter, E. Zavattini, A. Bertin, M. Piccinini, A. Vitale, and D. Measday, Nucl. Phys. A352, 365 (1981).

11. A.A. Quaranta, A. Bertin, G. Matone, F. Palmonari, G. Torelli, P. Dalpiaz, A. Placci, and E. Zavattini, Phys. Rev. 177, 2118 (1969).

12. M. Bubak and M.P. Faifman, JINR preprint E4-87-464, Dubna (1987).

13. W.H. Breunlich, M. Cargnelli, J. Marton, N. Naegele, P. Pawlek, A. Scrinzi, J. Werner, J. Zmeskal, J. Bistirlich, K.M. Crowe, M. Justice, P. Kammel, J. Kurck, C. Petitjean, R.H. Sherman, H. Bossy, H. Daniel, T.von Egidy, J.Hartmann, W. Neumann, and H. Schmid, LBL-21174, Berkeley (1986).

14. N. Cabibbo, Weak Interactions and High Energy Neutrino Physics, ed. T.D. Lee (Academic Press, New York, 1966).

15. M.L. Goldberger and S.B. Treiman, Phys. Rev. 111, 354(1958).

16. U. Fano, Ann. Rev. Nuc. Sci. 13, 1 (1963).

17. J.F. Janni, At. Dat. and Nucl. Dat. Tables 27, 147 (1982).

18. H. Schmidt Böcking, Experimental Methods in Heavy Ion Physics, ed. K. Bethge (Springer-Verlag, Berlin, 1978).

19. A.S. Wightman, Phys. Rev. 77, 521 (1950).

20. D.K. Brice, Phys. Rev. A 6, 1791 (1972).

21. H. Anderhub, J. Böcklin, M. Devereux, F. Dittus, R. Ferreira Marques, H. Hofer, H.K. Hofer, F. Kottmann, O. Pitzurra, P.G. Seiler, D. Taqqu, J. Unternährer, and M. Wälchli, Phys. Lett. 101B, 151 (1981).

22. E.F. Fermi and E. Teller, Phys. Rev. 72, 399 (1947).

23. G.A. Baker, Phys. Rev. 117, 1130 (1960).

24. R.A. Mann and M.E. Rose, Phys. Rev. 121, 293 (1961).

25. P. Vogel, P.K. Haff, V. Akylas, and A. Winter, Nucl. Phys. A254, 445 (1975).

26. M. Leon and R. Seki, Nucl. Phys. A282, 445 (1977).

27. M. Leon and J.H. Miller, Nucl. Phys. A282, 461 (1977).

28. G. Ya Korenman and S.I. Rogovaya, J. Phys. B13, 641 (1980).

29. P.K. Haff and T.A. Tombrello, Ann. of Phys. 86, 178 (1974).

30. M.Y. Au-Yang and M.L. Cohen, Phys. Rev. 174, 468 (1968).

31. J.S. Cohen, R.L. Martin, and W.L. Wadt, Phys. Rev. A 24, 33 (1981).

32. R.L. Rosenberg, Phil. Mag. 40, 759 (1949).

33. J.S. Cohen, Phys. Rev. A 27, 167 (1983).

34. V.V. Balashov, V.K. Dolinov, G. Ya Korenman, S.V. Leonora, I.V. Moskalenko, and V.P. Popov, Muon Catalyzed Fusion 2, 105 (1988).

35. A. Bertin, A. Vitale, and A. Placci, Riv. Nuov. Cim. 5, 423 (1975).

36. M. Leon and H. A. Bethe, Phys. Rev. 127, 636 (1962).

37. L. Bracci and G. Fiorentini, Nuov. Cim. 43A, 9 (1978).

38. L.I. Menshikov, Muon Catalyzed Fusion 2, 173 (1988).

39. M. Leon, Phys. Lett. 35B, 413 (1971).

40. E.H.S. Burhop, High Energy Physics Vol. III, ed. E.H.S. Burhop (Academic Press, New York, 1969).

41. B. Budic, J.R. Toraskar, and I. Yaghoobia, Phys. Lett. 34B, 539 (1971).

42. A. Placci, E. Polacco, E. Zavattini, K. Ziock, C. Carboni, U. Gastaldi, G. Gorini, and G. Torelli, Phys. Lett. 32B, 413 (1970).

43. F. Kottmann, Workshop on Exotic Atoms, PSI, June 1988.

44. G.R. Burbidge and A.H. De Borde, Phys. Rev. 89, 189 (1953).

45. E. Borie and M. Leon, Phys. Rev. A 21, 1460 (1980).

46. L.I. Ponomarev, L.N. Somov and M.I. Faifman, Sov. J. Nucl. Phys. 29, 67 (1979).

47. T.Y. Wu and T. Ohmura, Quantum Theory of Scattering (Prentice-Hall, Inc., Englewood Cliffs,N.J., 1962).

48. A. Matveenko, Sov. Phys. JETP 38, 1082 (1974).

49. M.P. Faifman, Sov. J. Nucl. Phys. 26, 227 (1977).

50. V.Z. Melezhik and J. Wozniak, Phys. Lett. 116A, 370 (1986).

51. A. Adamczak and V.S. Melezhik, Phys. Lett. 118A, 181 (1986).

52. V.I. Fomichev and A.I. Mikhailov, Muon Catalyzed Fusion 2, 137 (1988).

53. A. Adamczak and V.S. Melezhik, Muon Catalyzed Fusion 2, 138 (1988).

54. A. Adamczak, V.S. Melezhik, and L.I. Menshikov, JINR preprint E4-86-29, Dubna (1986).

55. A. Bertin, M. Capponi, I. Massa, M. Piccinini, G. Vannini, M. Poli, and A. Vitale, Nuov. Cim. 72A, 225 (1982).

56. P.K. Haff, E. Rodrigo, and T.A. Tombrello, Ann. Phys. 104, 363 (1977).

57. F.J. Hartmann, R. Bergmann, H. Daniel, H.J. Pfeiffer, T. von Egidy, and W. Wilhelm, Atoms and Nuclei 305, 189 (1982).

58. L. Bracci and G. Fiorentini, Nuov. Cim. 50A, 373 (1979).

59. G. Fiorentini and G. Torelli, Nuov. Cim. 36A, 317 (1976).

60. A. Bertin, M. Bruno, A. Vitale, A. Placci, and E. Zavattini, Phys. Rev. A 7, 462 (1973).

61. Y. Eisenberg and D. Kessler, Nuov. Cim. 19, 1195 (1961).

62. A. Bertin, M. Capponi, I. Massa, M. Piccinini, G. Vannini, and A. Vitale, Lett. Nuov. Cim. 31, 73 (1981).

63. A. Bertin, I. Massa, M. Piccinini, G. Vannini, and A. Vitale, Phys. Lett. 74A, 39 (1979).

64. A. Bertin, F. Ferrari, I. Massa, M. Piccinini, G. Vannini, and A. Vitale, Phys. Lett. 72A, 319 (1979).

65. H.J. Evans, Nucl. Phys. A207, 379 (1973).

66. E.A. Remler and R.T. Siegel, WmMary 86-5, 1986 (unpublished).

67. The foils were constructed and tested by : Pennwalt Corporation, King of Prussia, PA 19406-0018.

68. A. Placci, E. Zavattini, A. Bertin and A. Vitale, Nuov. Cim. 64A, 1053 (1969).

69. Calculated using mass attenuation coefficients from : J. H. Hubbell, Int. J. Appl. Rad. Isot. 33, 1269 (1982).

70. SIN User's Handbook, (1981).

71. R. Engfer, H. Schneuwly, J.L. Villeumier, H.K. Walter, and A. Zehnder, At. Dat. and Nucl. Dat. Tab. 14, 509 (1974).

72. F.J. Hartmann, private communication.

73. C.M. Lederer and V.S. Shirley, ed., Table of Isotopes, 7th ed. (John Wiley and Sons, Inc., New York, 1978).

74. D.K. Anderson and D.A. Jenkins, in Nuclear Spectroscopy and Reactions Part B, (Academic Press,Inc., New York, 1974).

75. C.K. Hargrove, E.P. Hincks, G. R. Mason, R.J. McKee, D. Kessler, and S. Ricci, Phys. Rev. Lett. 23, 215 (1969).

76. FITA, Technical University of Munich.

77. R. Siegel, WmMary 87-4, 1987 (unpublished).

78. L. Schlapbach, private communication.

79. G. Barth, SSL Reflections, Winter 1985.

80. N. Sasamoto, K. Koyama, and S. Tanaka, NIM 125, 597 (1975).

81. I.V. Anicin and C.T. Yap, NIM in Physics Research A259, 525 (1987).

82. R. Siegel, WmMary 88-4, 1988 (unpublished).

83. A.G. Frodesen, O. Skjeggestad, and H. Tofte, Probability and Statistics in Particle Physics (Universitetsforlaget, Bergen, Norway, 1979).

84. E.D. Cashwell and C.J. Everett, Practical Manual on the Monte Carlo Method for Random Walk Problems (Pergamon Press, New York, 1959).

85. S. Park and K. Miller, Comm. of the ACM (1988).

86. E. Fermi, Nuclear Physics (University of Chicago Press, Chicago, 1950).

87. MINUIT, F. James and M. Roos, CERN Program Library D506.

88. T. Suzuki, D.F. Measday, and J.P. Roalsvig, Phys. Rev. C 35, 2212 (1987).

89. G. Chen, private communication.

90. R. Siegel, WmMary 86-2, 1986 (unpublished).

91. L. Bracci and G. Fiorentini, 1987 (unpublished).

92. S. Park, private communication.

93. W.H. Press, B.P. Flannery, S.A. Teukolsky, and W.T. Vetterling, Numerical Recipes - The Art of Scientific Computing (Cambridge University Press, Cambridge, 1986).

FIGURE CAPTIONS

Fig. 1 Probability per unit time P(t) for a μd atom to strike a foil surface in the limit of no scattering in the foil gap. The solid curve represents P(t) for a delta function initial velocity distribution of mean energy 1.0 eV. The dashed curve is P(t) for a Maxwell velocity distribution of mean energy 3KT/2 = 1.0 eV. Both curves assume that the μd atoms are formed uniformly between semi-infinite foils separated by a spacing of 0.2 cm and are initially moving isotropically.

Fig. 2 Schematic of the gas system used in the experiment.
(a) High Vacuum System
(b) Gas Circulation System

Fig. 3 Layout of the μE4 experimental area at the Paul Scherrer Institute.

Fig. 4 Experimental setup of the diffusion experiment. Shown are the beam telescope counters 2,3, and 3A; charged particle veto counters V1 and V2; germanium detectors A,B,C, and GMX; and the target stack inside the aluminum pressure vessel.

Fig. 5 Simplified logic diagram of the electronics.
TFA = Timing Filter Amplifier, GG = Gate Generator
CFD = Constant Fraction Discriminator
DISC = Discriminator, DT = Delayed Trigger

Fig. 6 Typical prompt energy spectrum in the region 20-500 keV. Taken from D1520S data of Detector A. Time region is ± 30 ns.

Fig. 7 Typical delayed energy spectrum in the region 20-500 keV. Taken from D1520S data of Detector A. Time region is 200-2000 ns.

Fig. 8 Energy spectrum of Detector A when the solid Au target was placed in the muon beam. Time region is -30-500 ns.

Fig. 9 Comparison of carbon (solid circles) and nitrogen (open circles) time distributions at 7.85 bar. The carbon data are the sum of the C(3-1) and C(4-1) time distributions of Detector C from the May 1987 data. The nitrogen data are also from the May 1987 data and Detector B. All data are decay adjusted.

Fig. 10 Comparison of carbon time distributions as a function of pressure. Data are the sum of the C(3-1) and C(4-1) data from the May 1987 run and Detector C. Pressures shown are 7.85 bar (solid circles), 2.56 bar (open circles), and 1.28 bar (solid squares). All data are decay adjusted.

Fig. 11 The direction cosines u,v,w.

Fig. 12 The unit sphere in u,v,w space.

Fig. 13 Velocity diagram for a collision in the yz plane of the LAB frame between a projectile and a moving target. Here v_p is the projectile velocity, v_t is the target velocity, v_c is the velocity of the CM in the LAB frame, and v_r is the relative velocity between the projectile and the target. The CM axes Y,Z are shown for reference.

Fig. 14 Time distribution of delayed Pt nuclear γ-ray events observed under condition D94S. Experimental points are decay adjusted from data in Table XI. Solid curve is Monte Carlo fit to the data.

Fig. 15 Time distribution of delayed Pt nuclear γ-ray events observed under condition D188S. Experimental points are decay adjusted from data in Table XI. Solid curve is Monte Carlo fit to the data.

Fig. 16 Time distribution of delayed Pt nuclear γ-ray events observed under condition D375S. Experimental points are decay adjusted from data in Table XI. Solid curve is Monte Carlo fit to the data.

Fig. 17 Time distribution of delayed Pt nuclear γ-ray events observed under condition D750S. Experimental points are decay adjusted from data in Table XI. Solid curve is Monte Carlo fit to the data.

Fig. 18 Time distribution of delayed Pt nuclear γ-ray events observed under condition D1520S. Experimental points are decay adjusted from data in Table XI. Solid curve is Monte Carlo fit to the data.

Fig. 19 Time distribution of delayed Pt nuclear γ-ray events observed under condition D188D. Experimental points are decay adjusted from data in Table XI. Solid curve is Monte Carlo fit to the data.

Fig. 20 Time distribution of delayed Pt nuclear γ-ray events observed under condition D375D. Experimental points are decay adjusted from data in Table XI. Solid curve is Monte Carlo fit to the data.

Fig. 21 Time distribution of delayed Pt nuclear γ-ray events observed under condition D750D. Experimental points are decay adjusted from data in Table XI. Solid curve is Monte Carlo fit to the data.

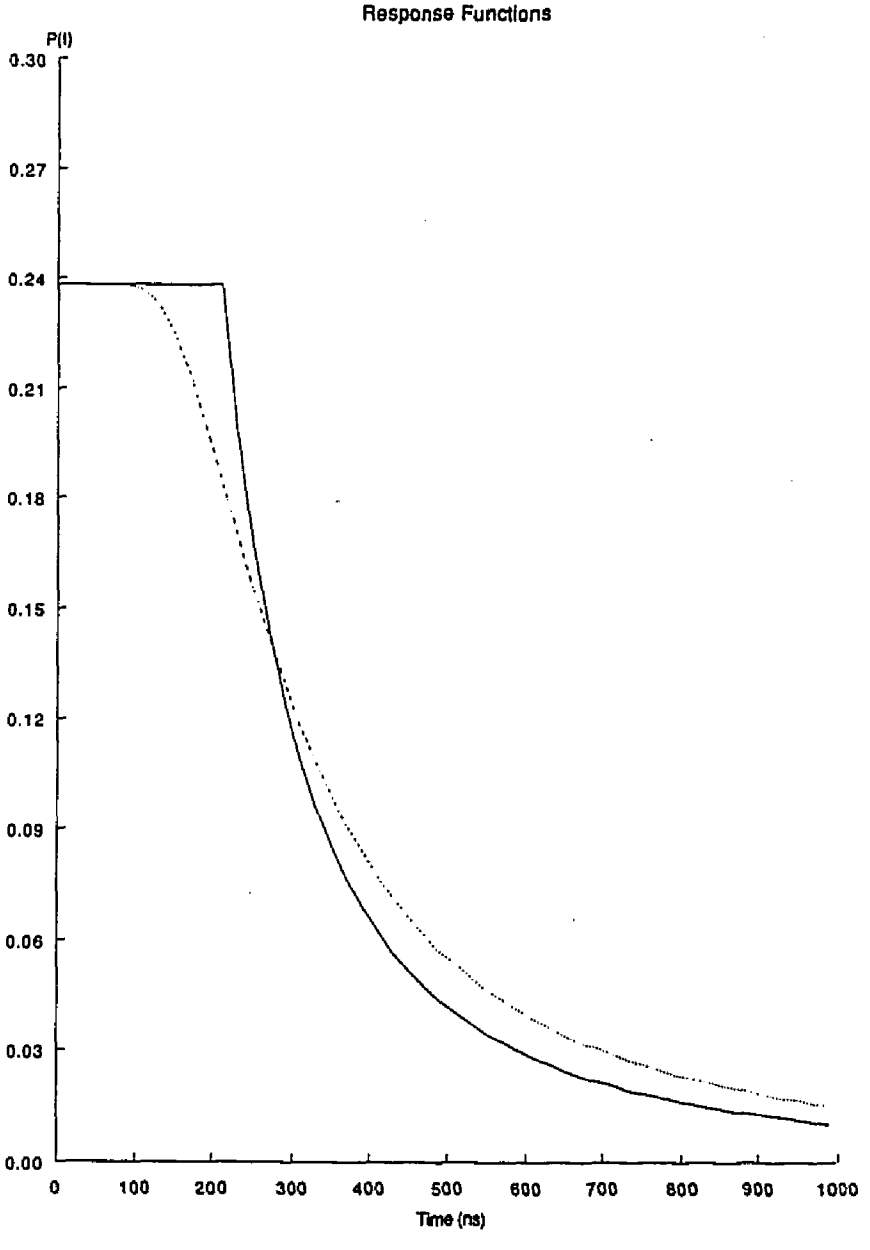
Response Functions
P(t)
0.30
0.27
0.24
0.21
0.18
0.15
0.12
0.09
0.06
0.03
0.00
0
100
200
300
400
500
600
700
800
900
1000
Time (ns)

Figure 1

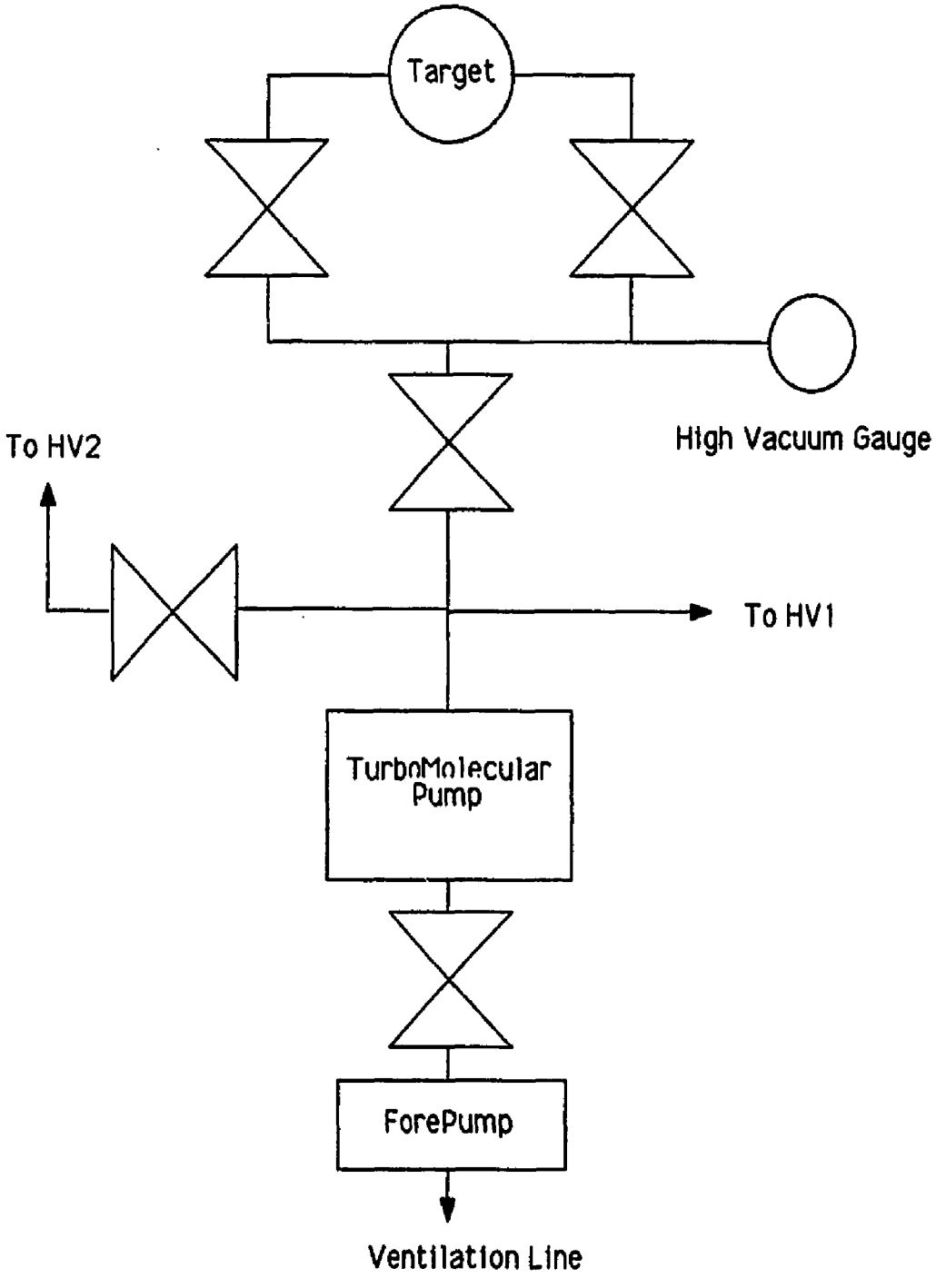
Target
High Vacuum Gauge
To HV2
To HV1
TurboMolecular Pump
ForePump
Ventilation Line

Figure 2a

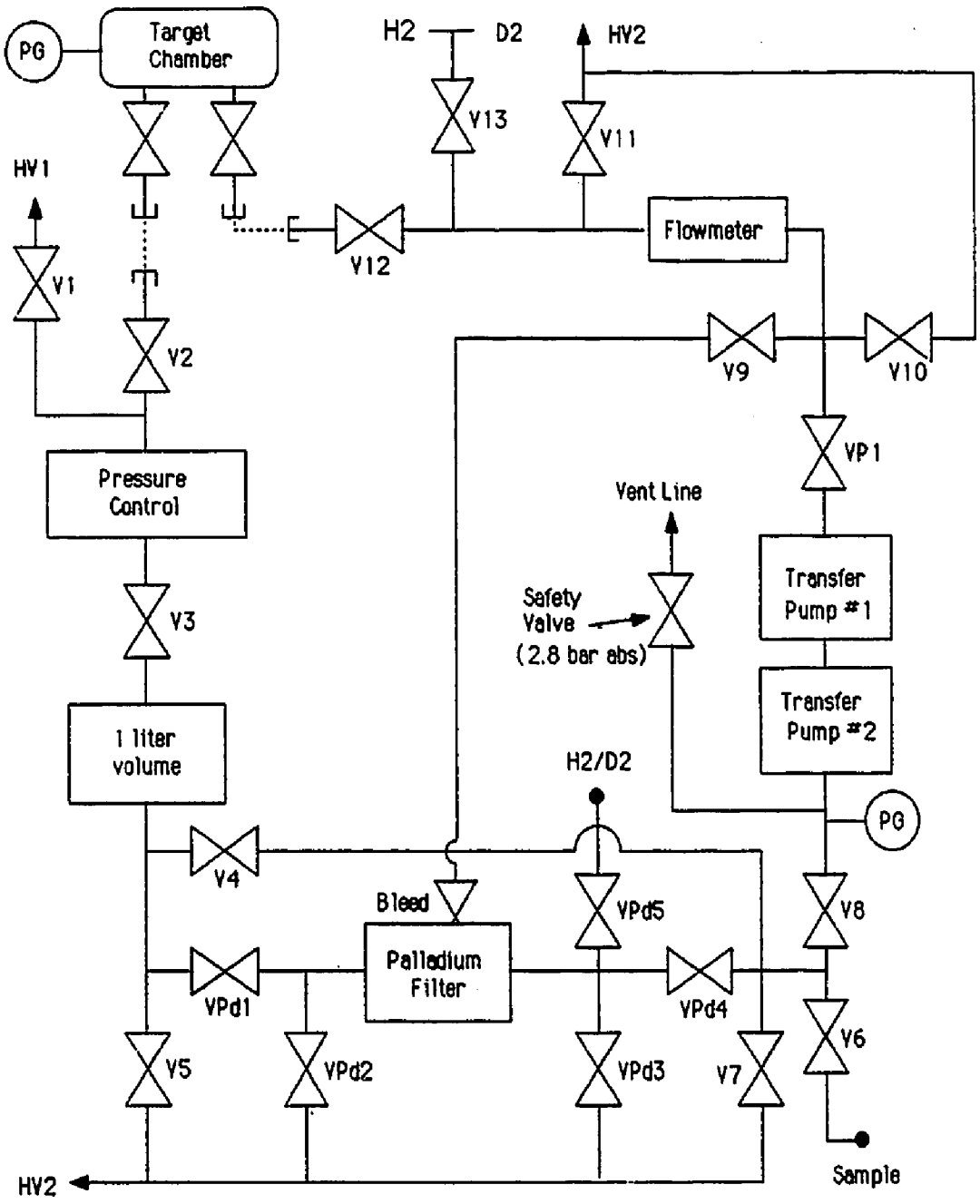
PG
Target Chamber
H2
D2
HV2
V13
V11
HV1
V1
V12
Flowmeter
V2
V9
V10
VP1
Pressure Control
Vent Line
Safety Valve (2.8 bar abs)
Transfer Pump #1
V3
Transfer Pump #2
1 liter volume
H2/D2
PG
V4
Bleed
VPd5
V8
Palladium Filter
VPd1
VPd4
V6
V5
VPd2
VPd3
V7
HV2
Sample

Figure 2b

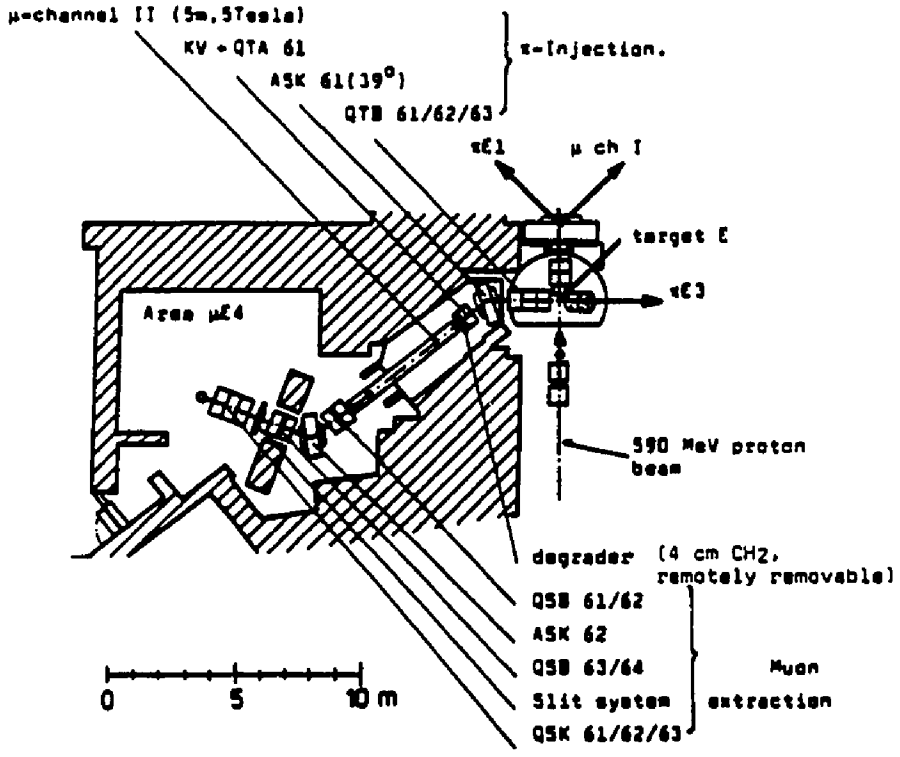
μ-channel II (5m,5Tesla)
KV + QTA 61
ASK 61(39°)
QTB 61/62/63
π-injection.
πE1
μ ch I
target E
πE3
Area μE4
590 MeV proton beam
degrader (4 cm CH2, remotely removable)
QSB 61/62
ASK 62
QSB 63/64
Slit system
QSK 61/62/63
Muon extraction
0
5
10 m

Figure 3

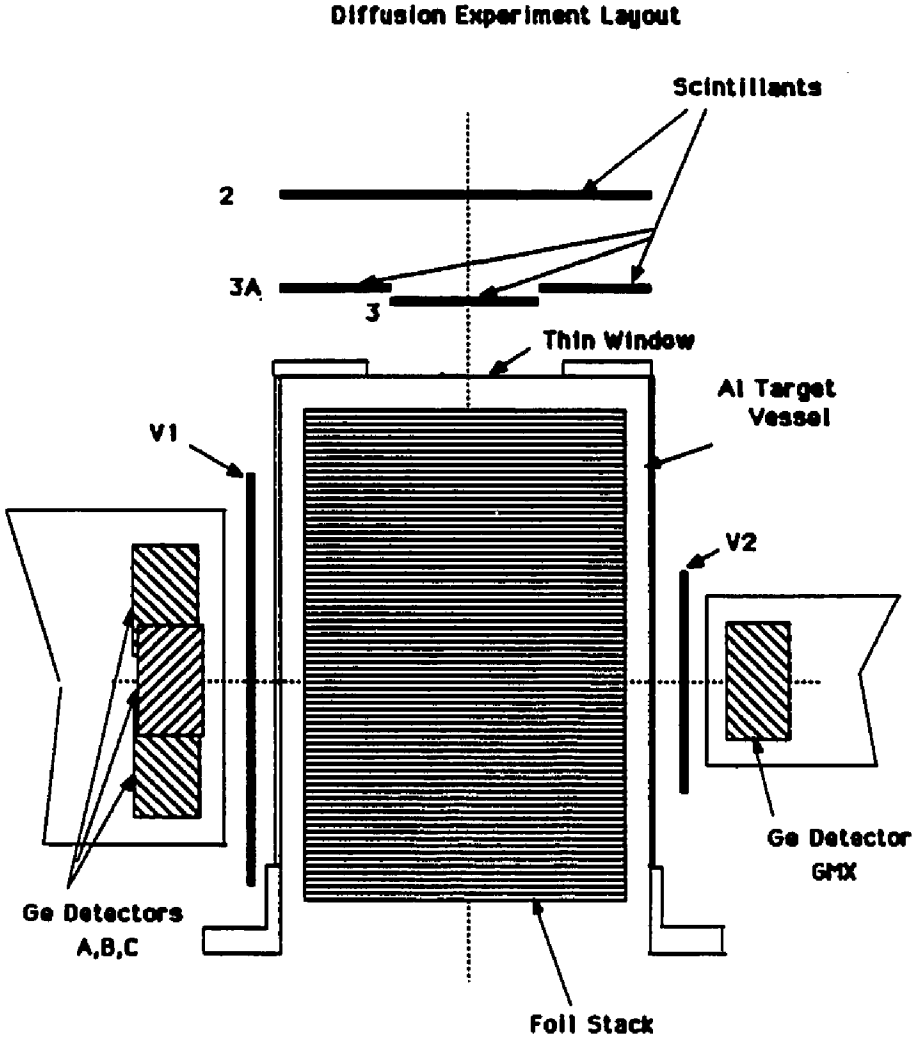
Diffusion Experiment Layout
Scintillants
2
3A
3
Thin Window
Al Target
Vessel
V1
V2
Ge Detectors
A,B,C
Ge Detector
GMX
Foil Stack

Figure 4

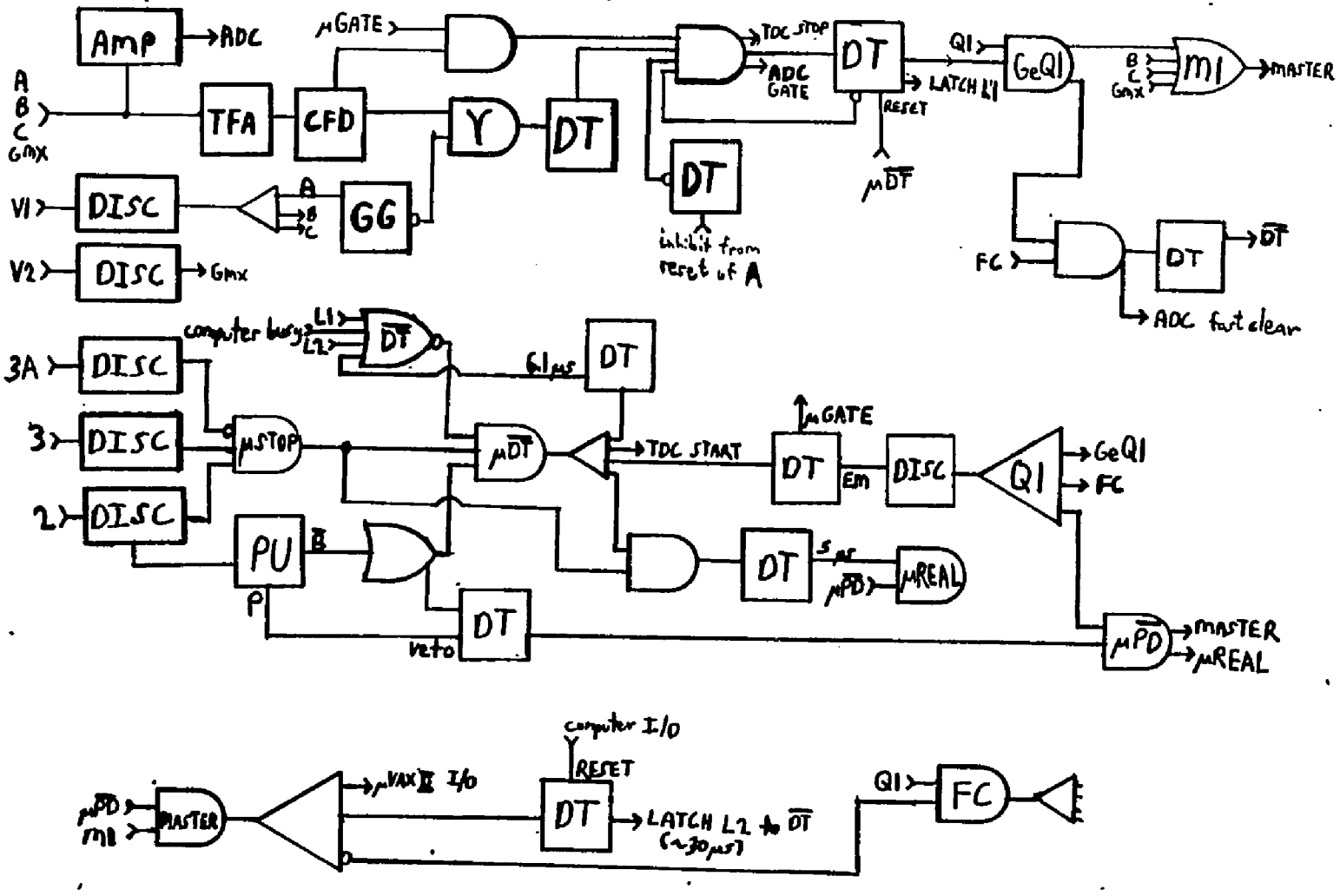
Amp
ADC
μGATE
A
B
C
Gmx
TFA
CFD
Y
DT
TDC STOP
ADC GATE
DT
Q1
GeQ1
LATCH L1
RESET
μDT
B
C
Gmx
m1
master
VI
DISC
A
B
C
GG
V2
DISC
Gmx
inhibit from reset of A
DT
FC
DT
DT
ADC fast clear
computer busy
L1
L2
DT
61μs
DT
3A
DISC
3
DISC
2
DISC
μSTOP
μDT
TDC START
μGATE
DT
Em
DISC
Q1
GeQ1
FC
PU
B
P
DT
veto
5μs
μPD
μREAL
μPD
master
μREAL
computer I/O
RESET
μPD
m1
master
μVAX II I/O
DT
LATCH L2 & DT
(~30μs)
Q1
FC

Figure 5

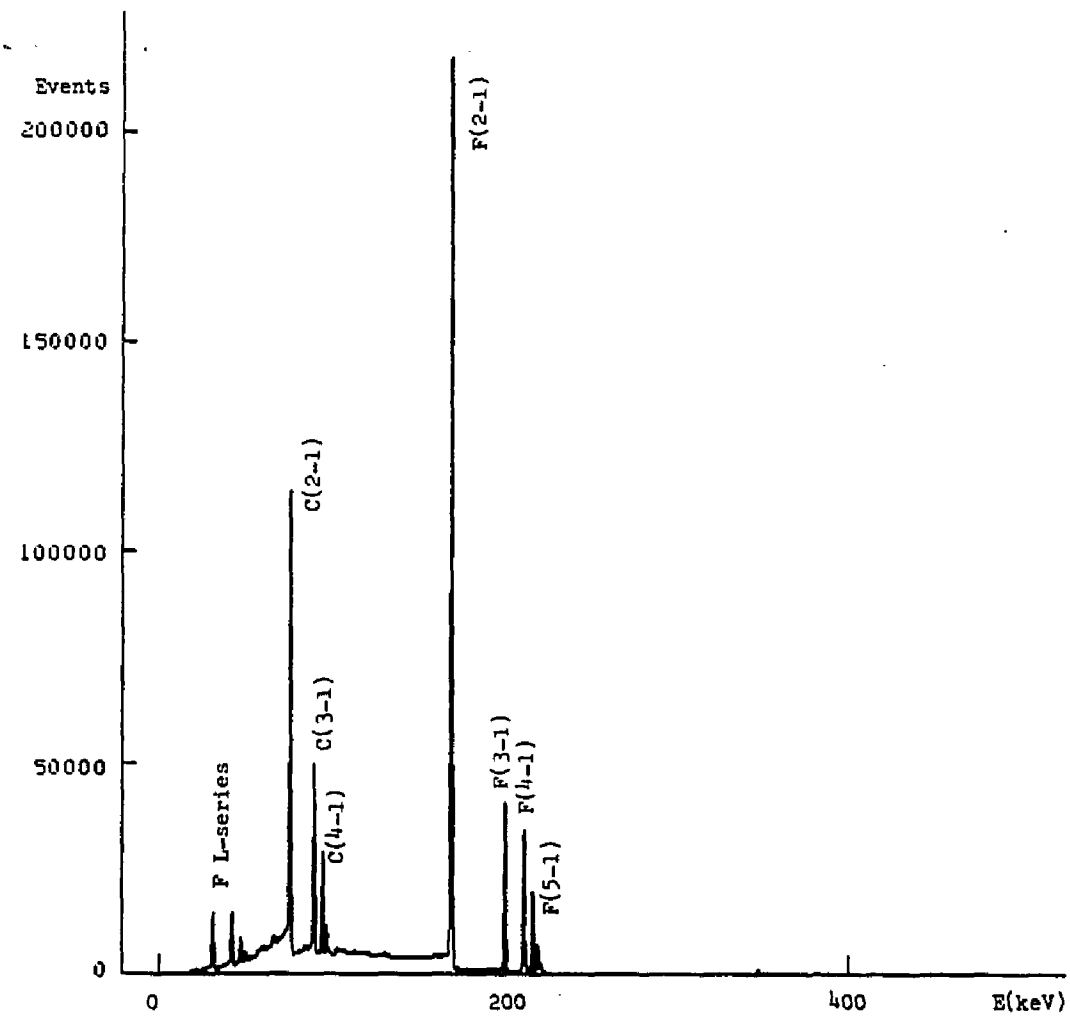
Events
200000
150000
100000
50000
0
F L-series
C(2-1)
C(3-1)
C(4-1)
F(2-1)
F(3-1)
F(4-1)
F(5-1)
0
200
400
E(keV)

Figure 6

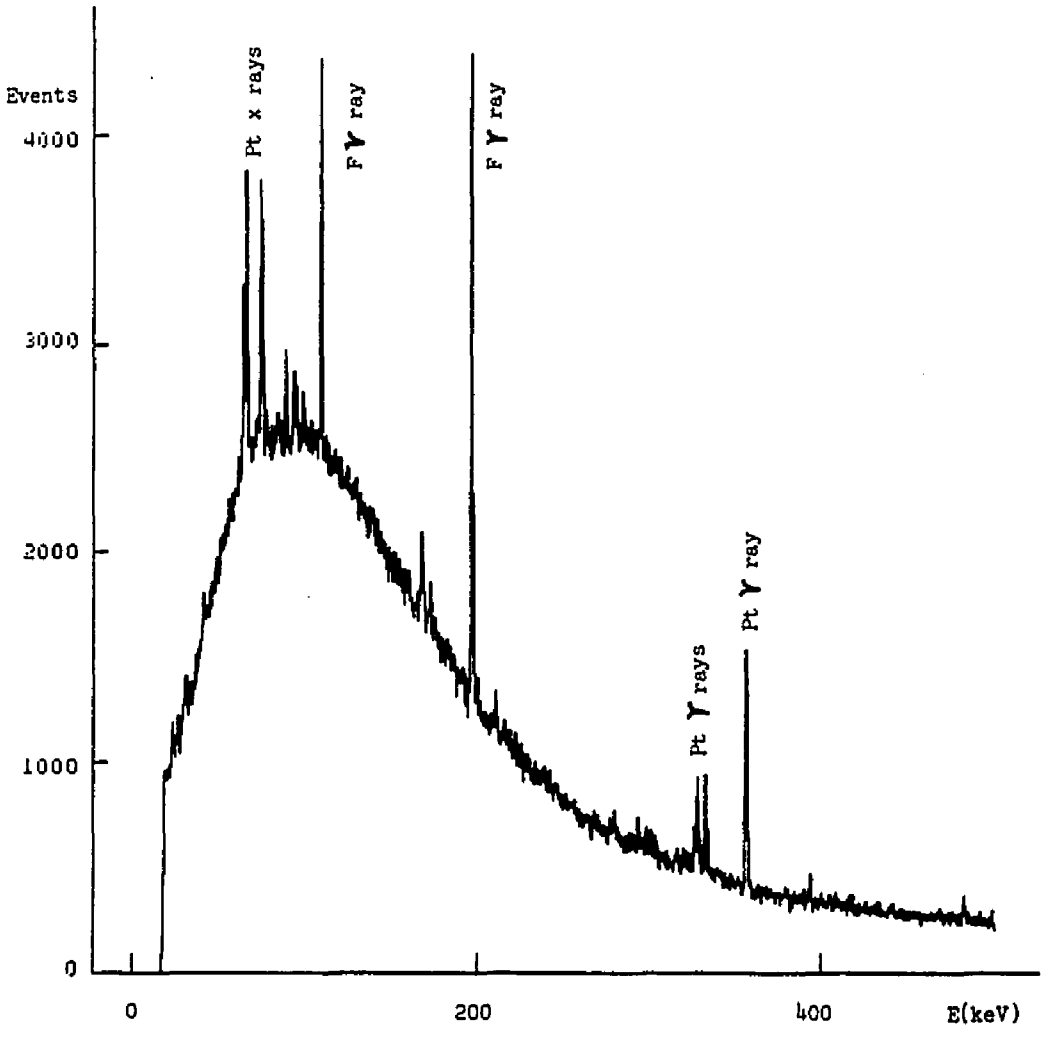
Events
4000
3000
2000
1000
0
Pt x rays
F γ ray
F γ ray
Pt γ rays
Pt γ ray
0
200
400
E(keV)

Figure 7

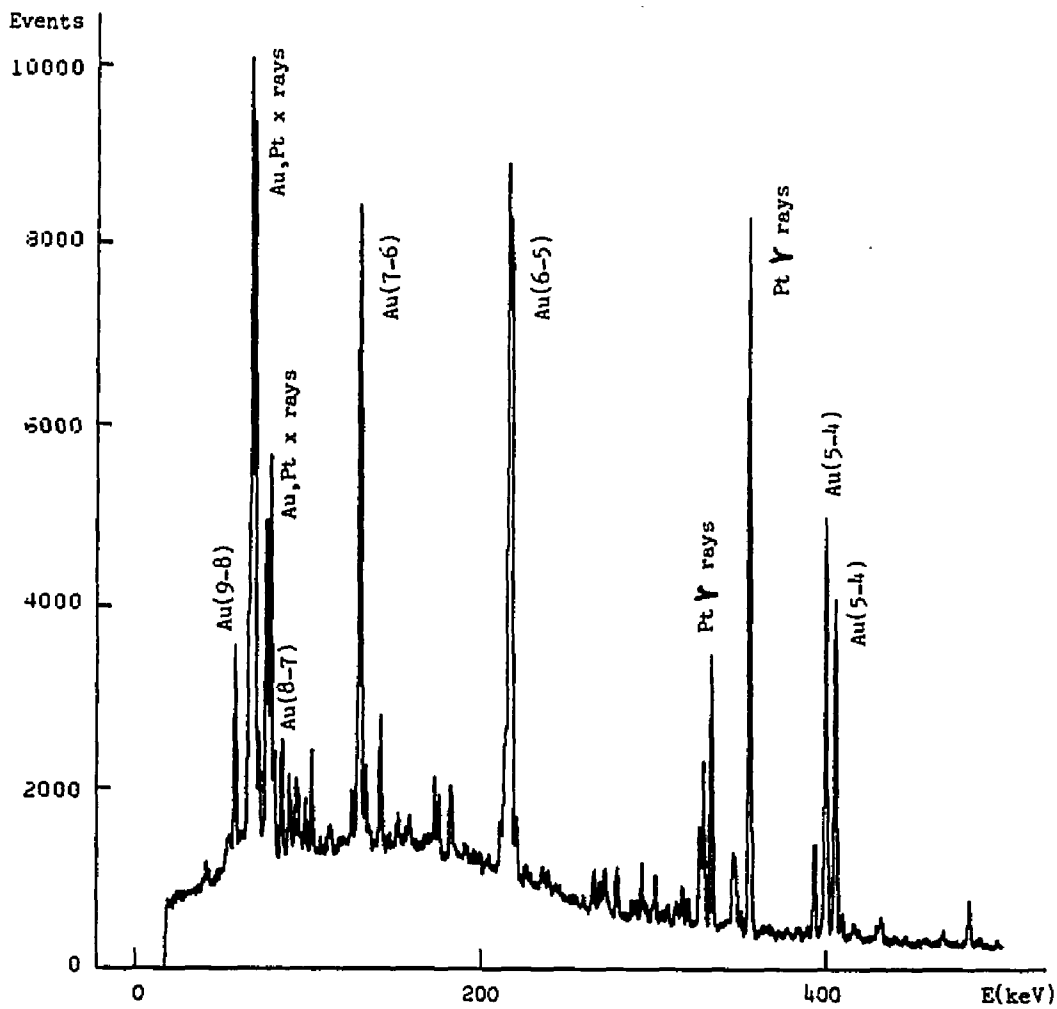
Events
10000
8000
6000
4000
2000
0
0
200
400
E(keV)
Au(9-8)
Au,Pt x rays
Au(8-7)
Au,Pt x rays
Au(7-6)
Au(6-5)
Pt γ rays
Pt γ rays
Au(5-4)
Au(5-4)

Figure 8

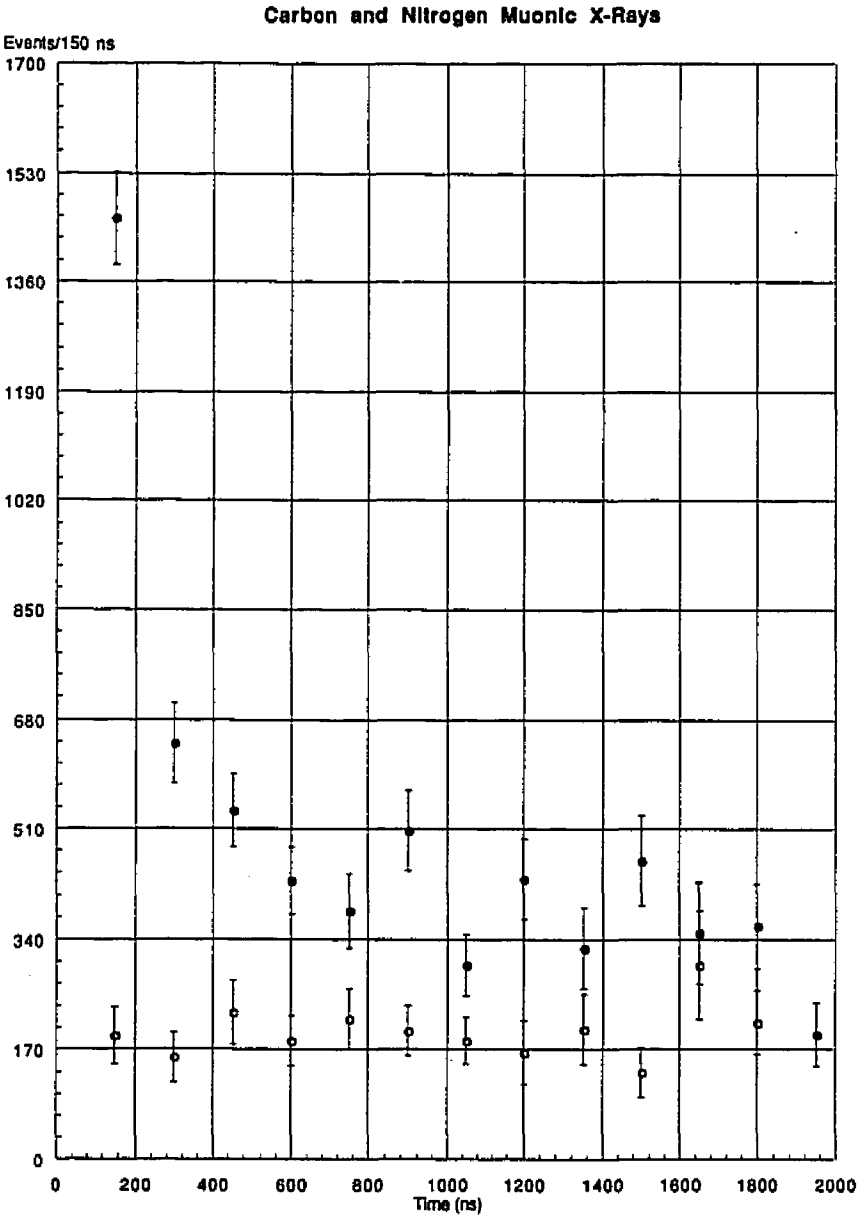
Carbon and Nitrogen Muonic X-Rays
Events/150 ns
1700
1530
1360
1190
1020
850
680
510
340
170
0
0
200
400
600
800
1000
1200
1400
1600
1800
2000
Time (ns)

Figure 9

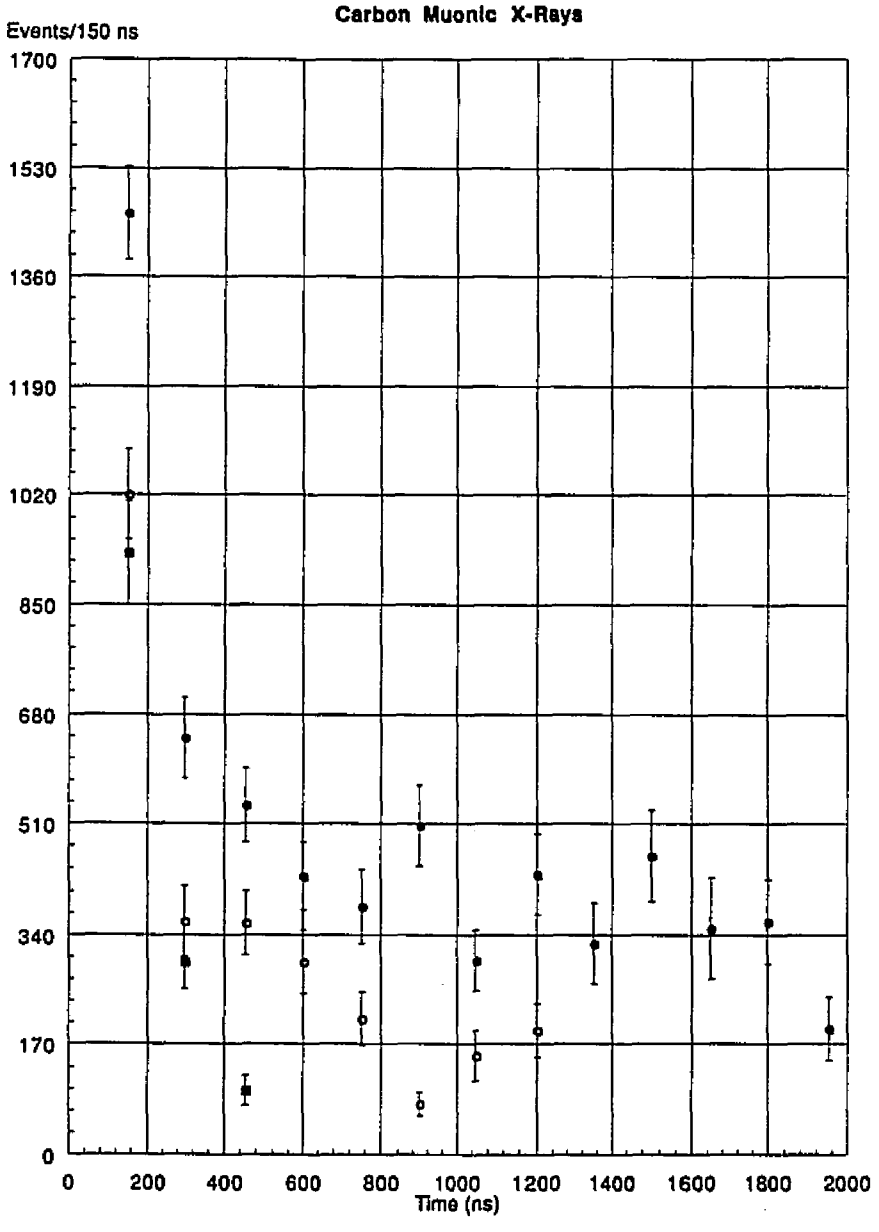
Carbon Muonic X-Rays
Events/150 ns
1700
1530
1360
1190
1020
850
680
510
340
170
0
0
200
400
600
800
1000
1200
1400
1600
1800
2000
Time (ns)

Figure 10

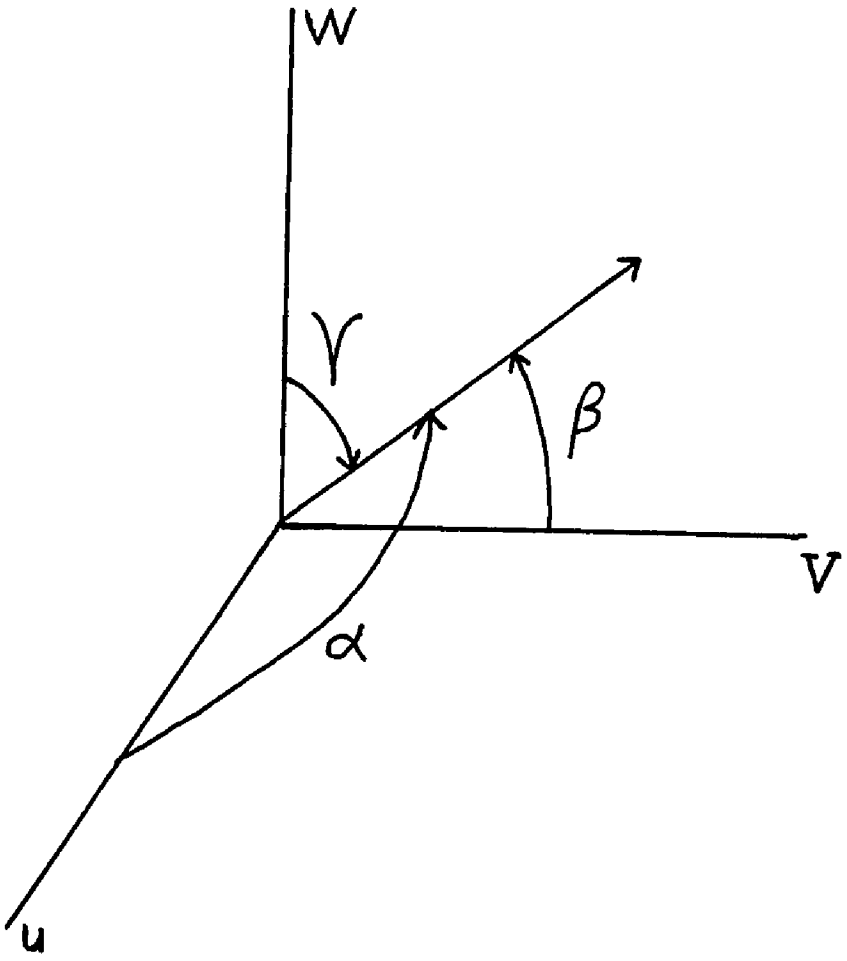

Figure 11

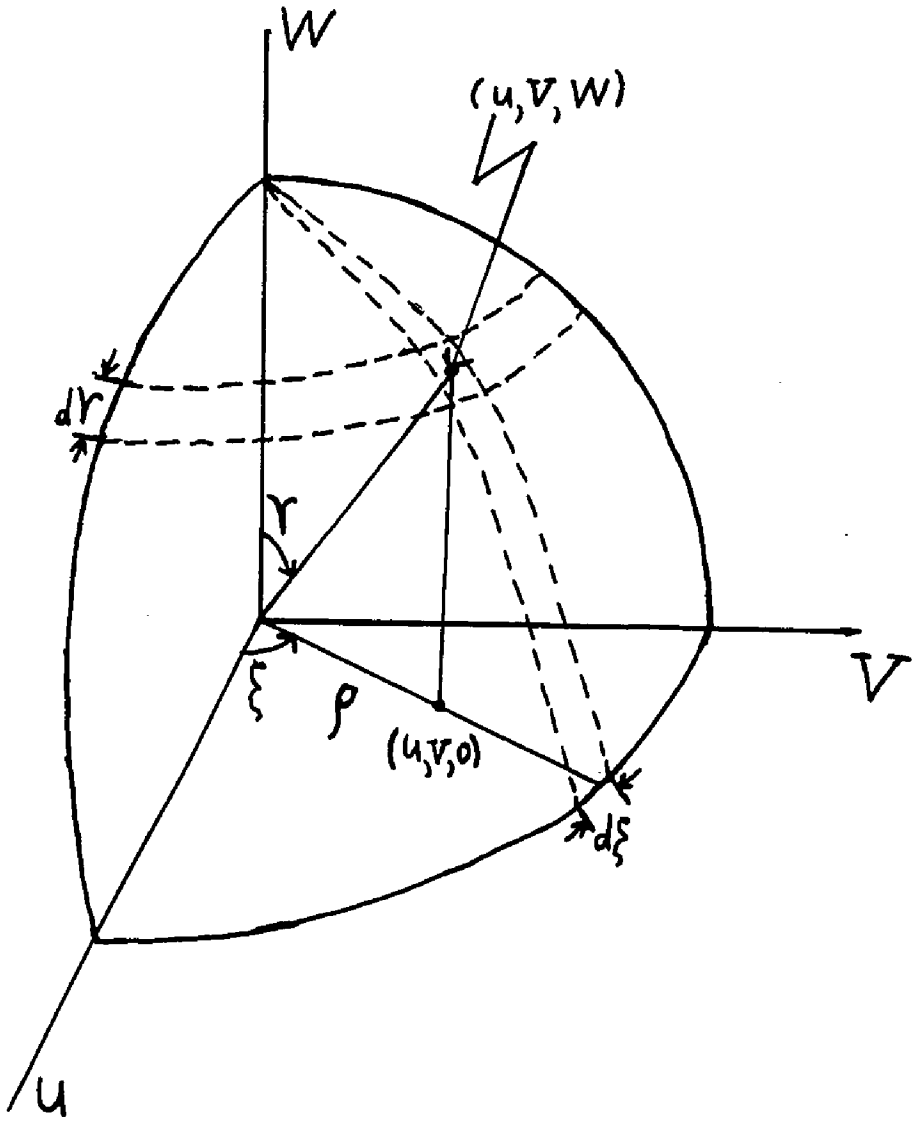

Figure 12

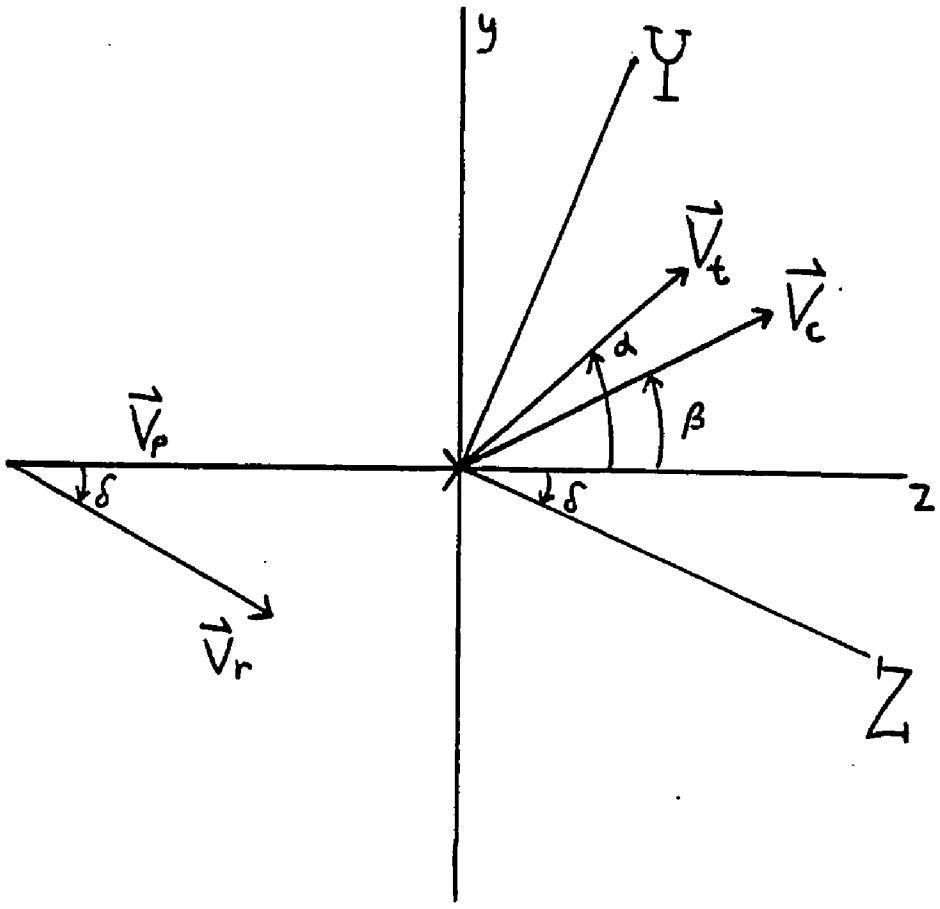

Figure 13

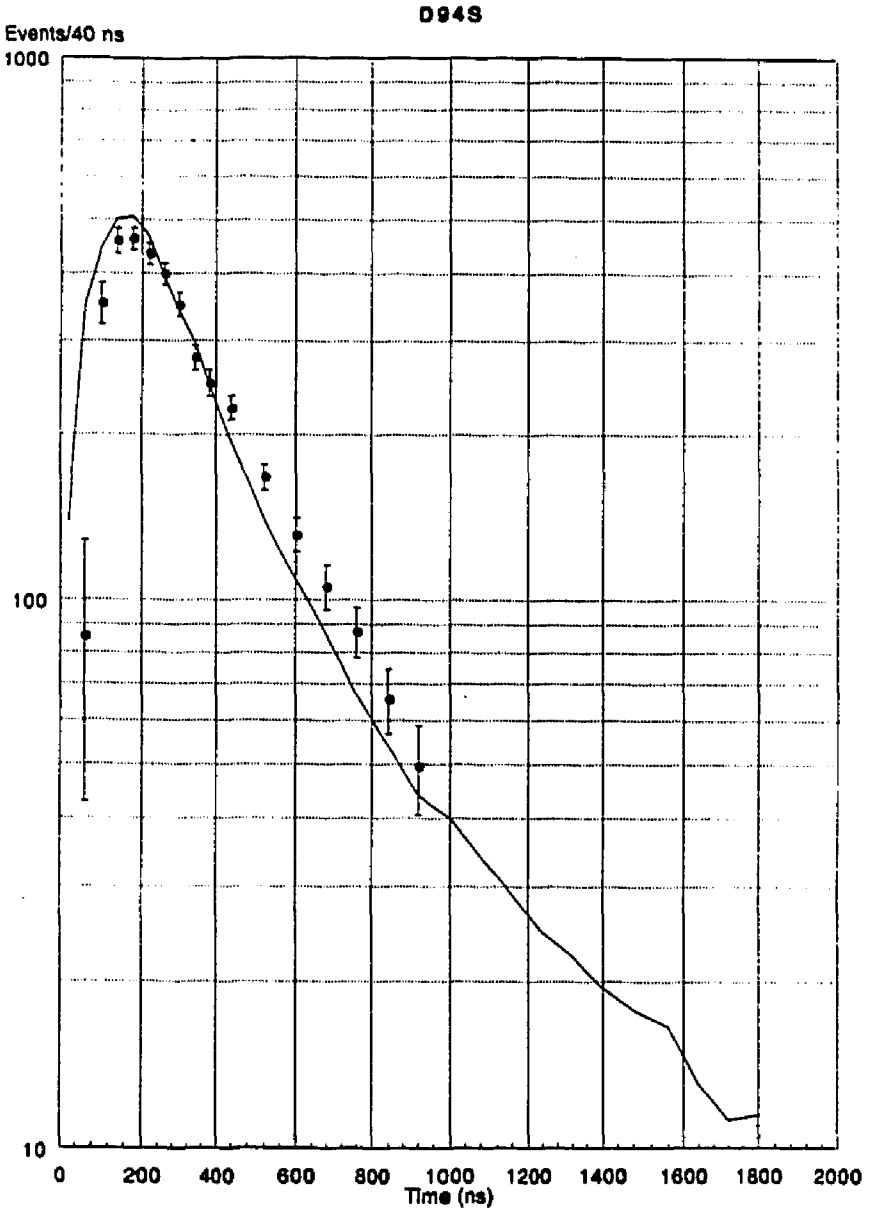
D94S
Events/40 ns
1000
100
10
0
200
400
600
800
1000
1200
1400
1600
1800
2000
Time (ns)

Figure 14

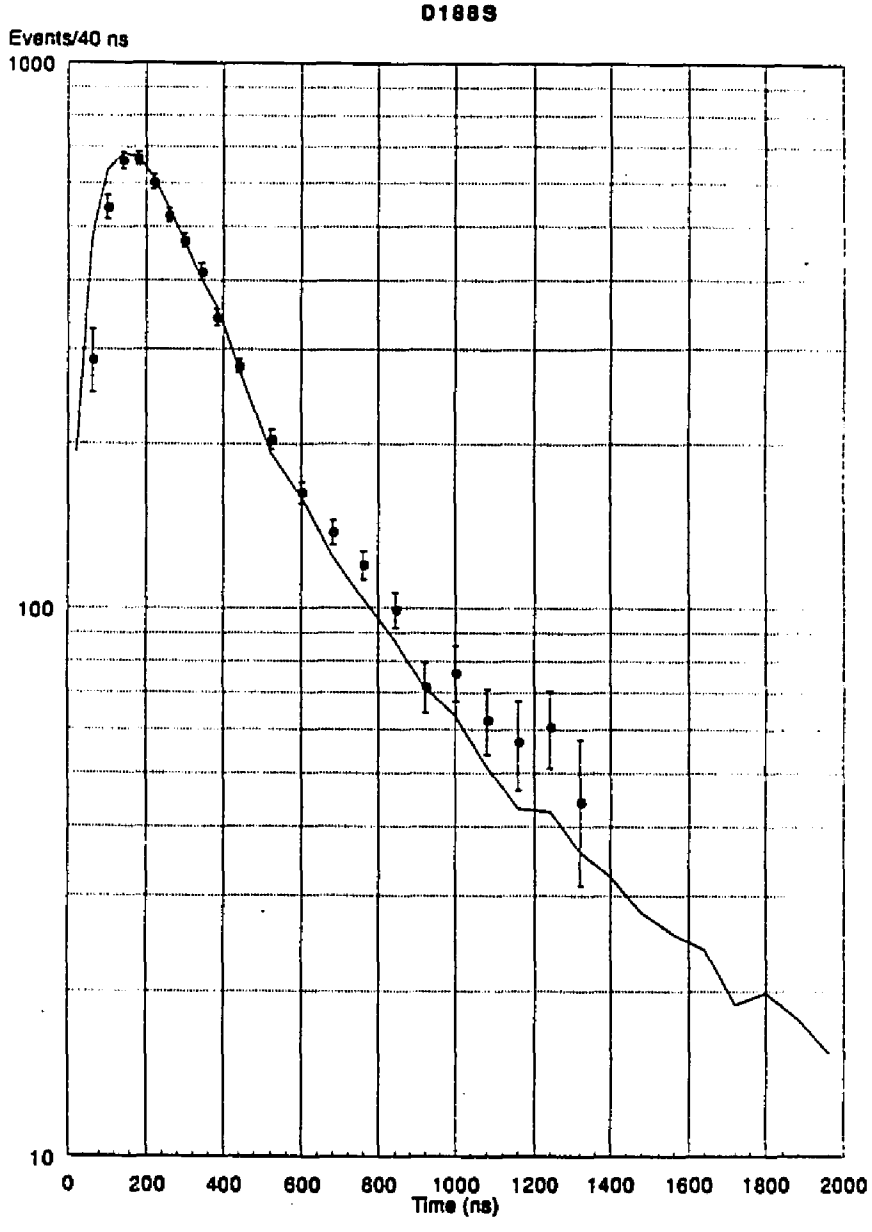
D188S
Events/40 ns
1000
100
10
0
200
400
600
800
1000
1200
1400
1600
1800
2000
Time (ns)

Figure 15

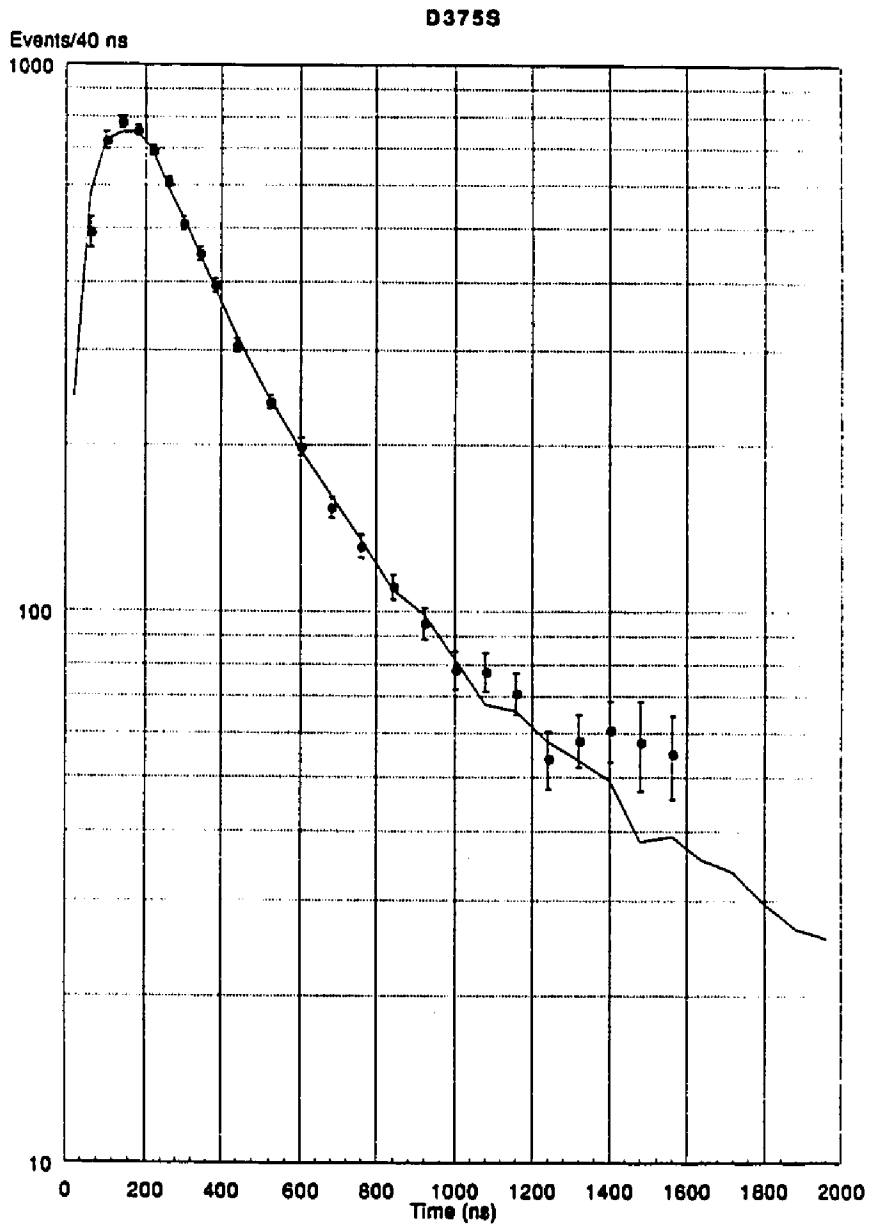
D375S
Events/40 ns
1000
100
10
0
200
400
600
800
1000
1200
1400
1600
1800
2000
Time (ns)

Figure 16

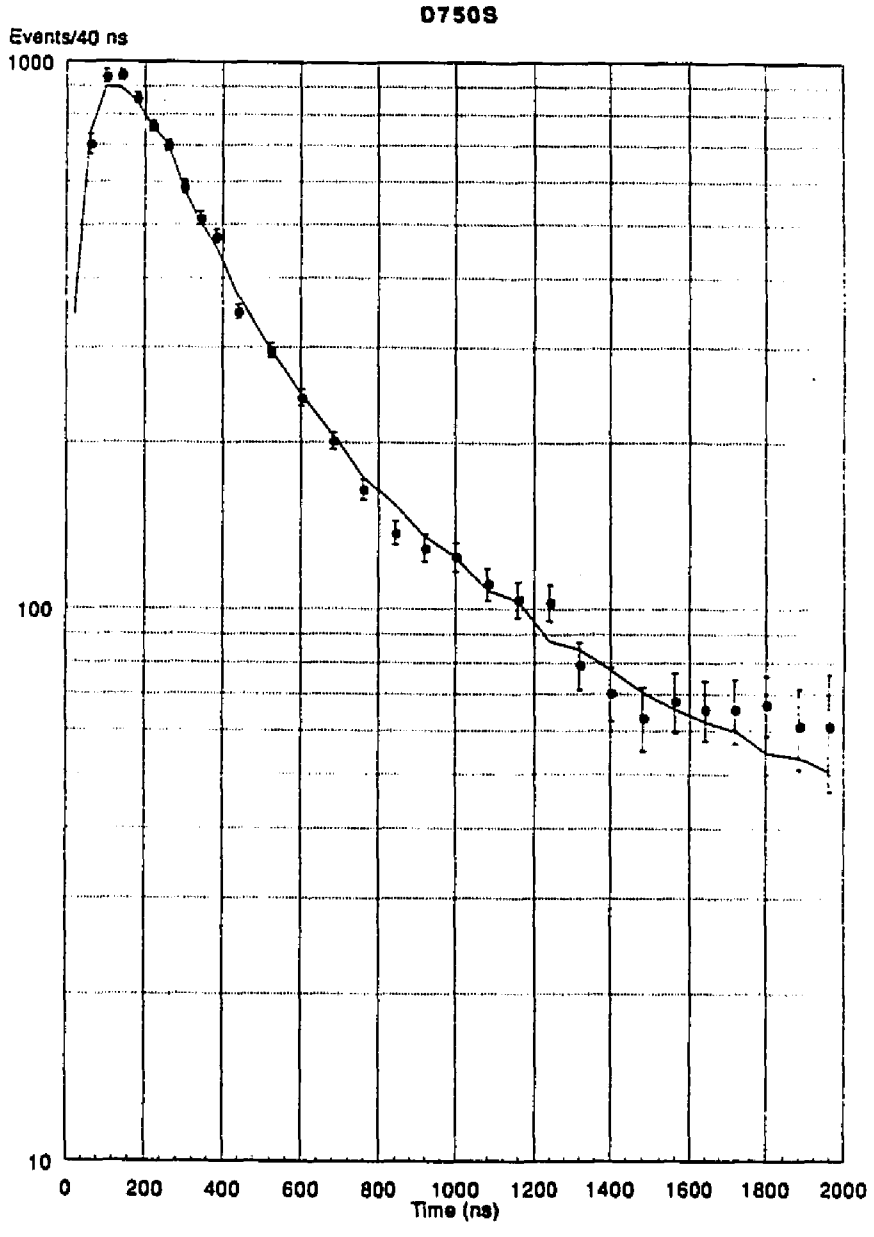
D750S
Events/40 ns
1000
100
10
0
200
400
600
800
1000
1200
1400
1600
1800
2000
Time (ns)

Figure 17

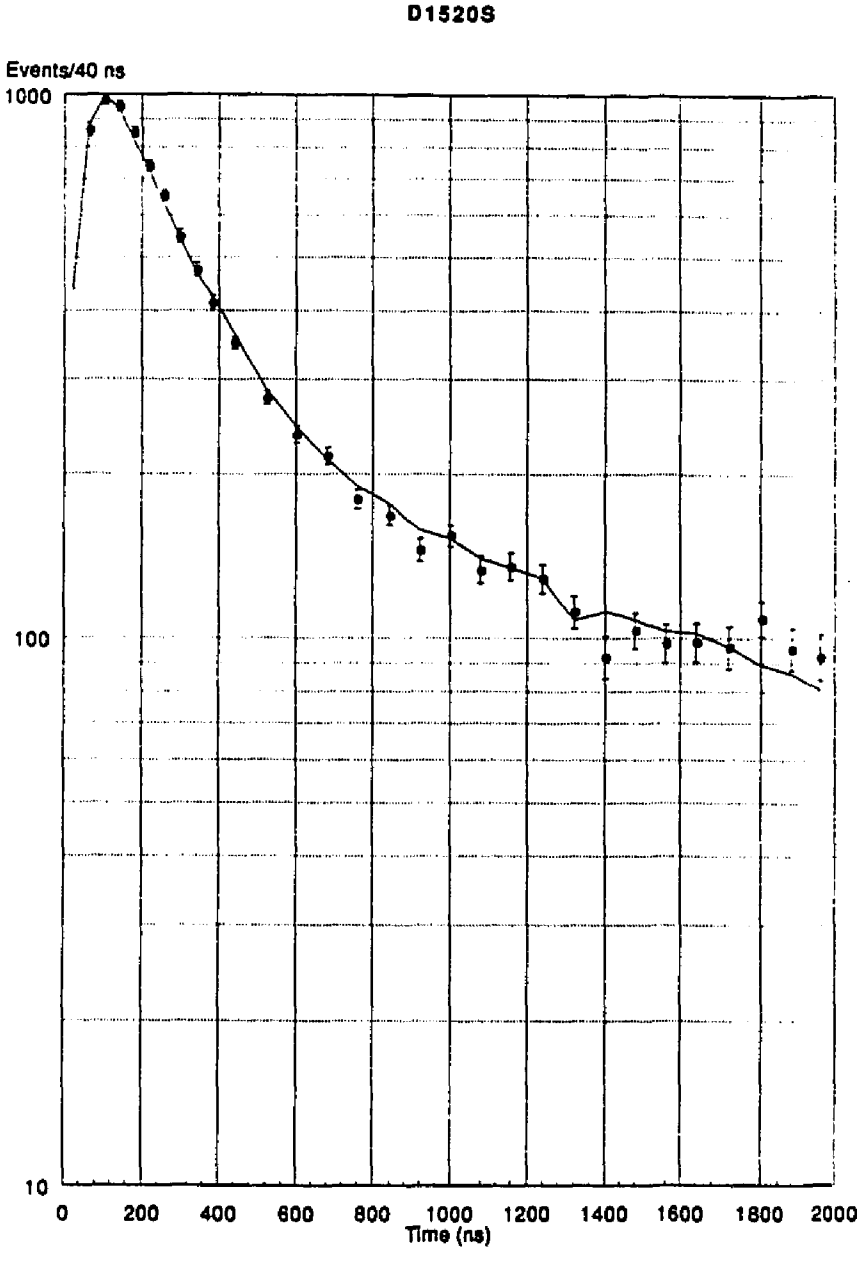
D1520S
Events/40 ns
1000
100
10
0
200
400
600
800
1000
1200
1400
1600
1800
2000
Time (ns)

Figure 18

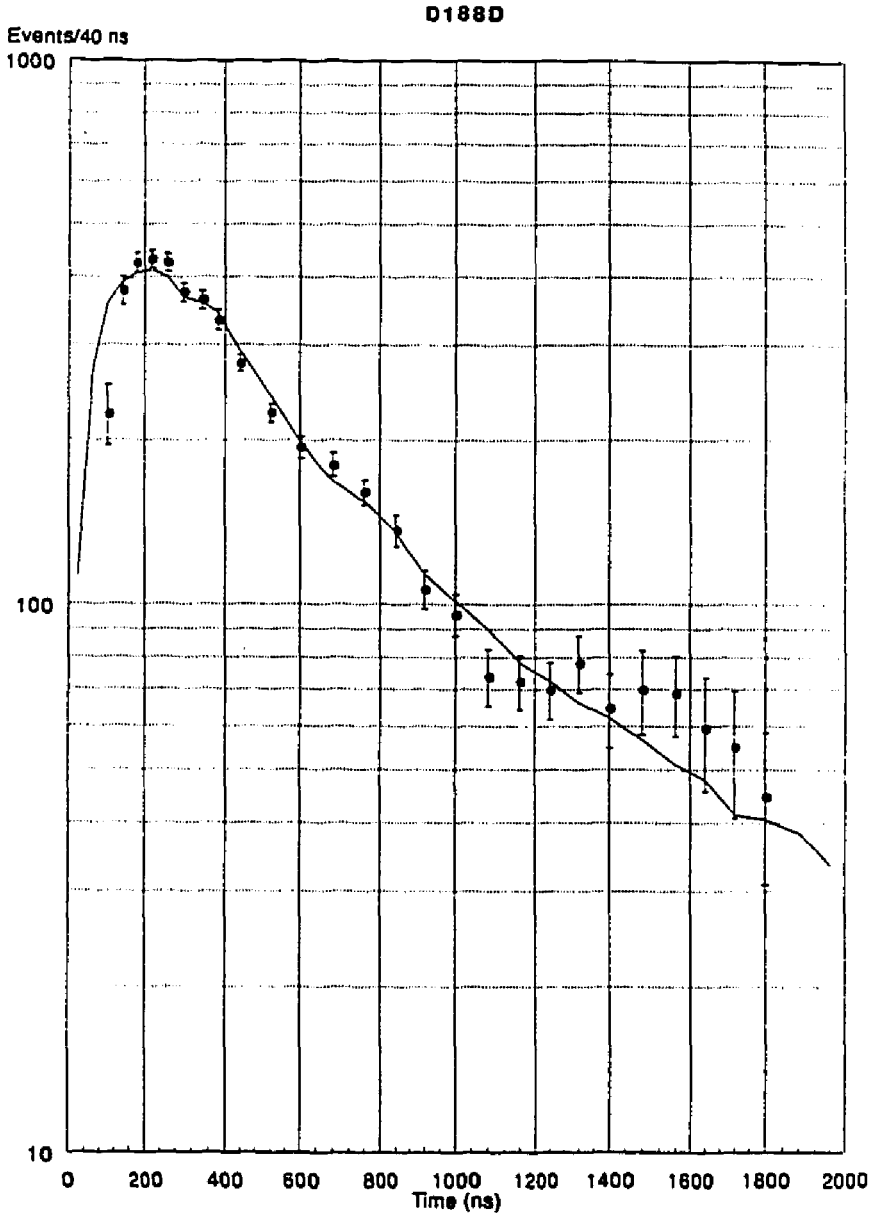
D188D
Events/40 ns
1000
100
10
0
200
400
600
800
1000
1200
1400
1600
1800
2000
Time (ns)

Figure 19

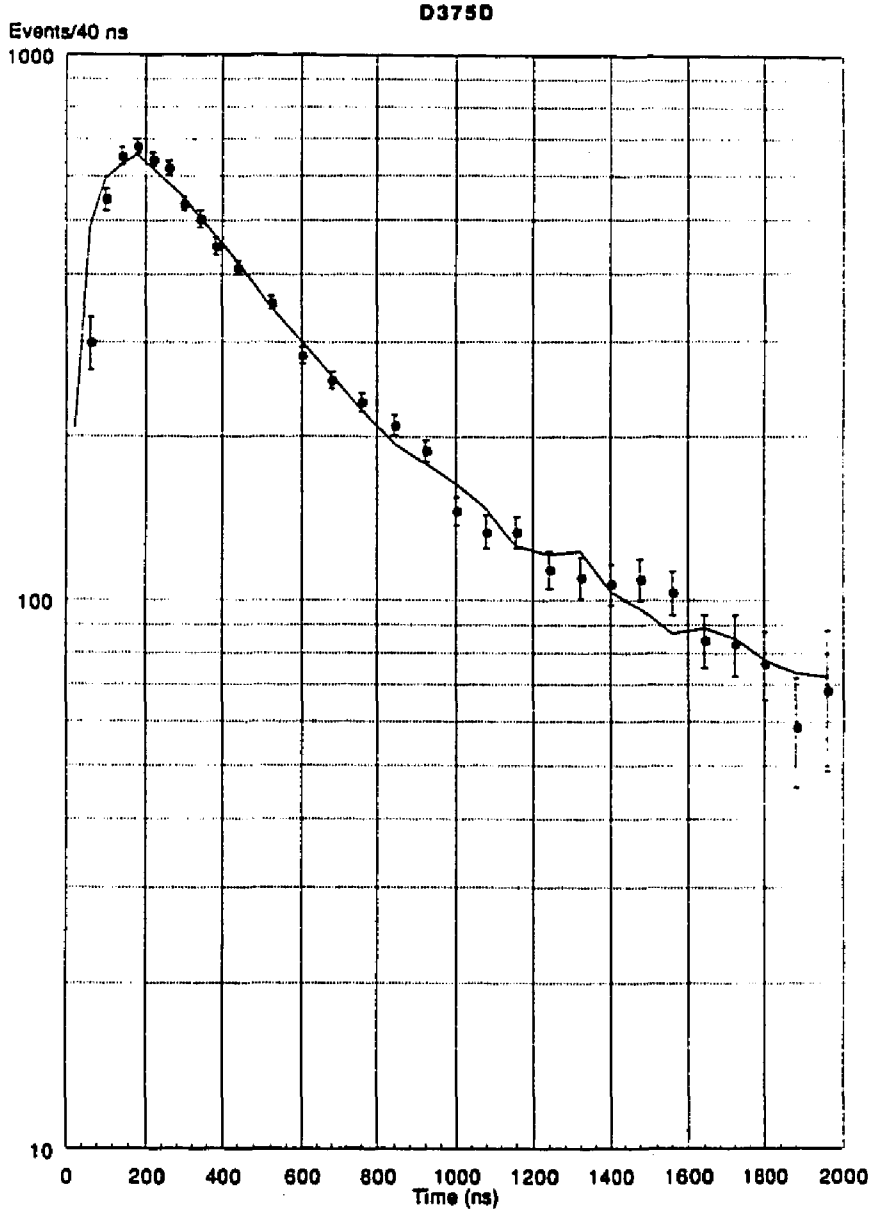
D375D
Events/40 ns
1000
100
10
0
200
400
600
800
1000
1200
1400
1600
1800
2000
Time (ns)

Figure 20

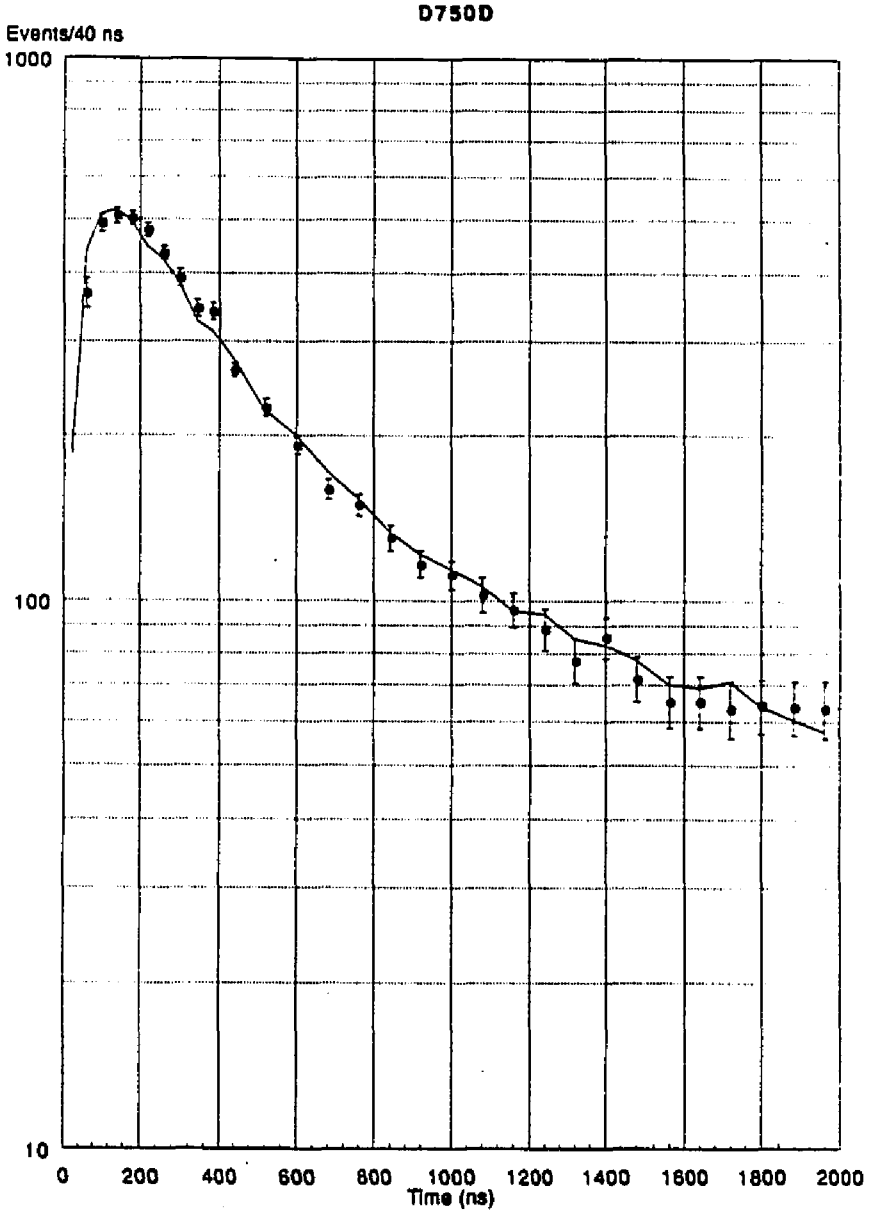
D750D
Events/40 ns
1000
100
10
0
200
400
600
800
1000
1200
1400
1600
1800
2000
Time (ns)

Figure 21

VITA

James Brian Kraiman was born in Philadelphia, PA on 3-August-59. Graduated from Plymouth-Whitemarsh Senior High School, Plymouth Meeting, PA in June, 1977. Graduated with a B.A. in physics from Gettysburg College in June, 1981. Completed requirements for Ph.D degree in Physics from the College of William and Mary in Virginia in January, 1989.